ALMA MATER STUDIORUM - UNIVERSITÀ DI BOLOGNA
SEDE DI CESENA
SECONDA FACOLTÀ DI INGEGNERIA CON SEDE A CESENA
CORSO DI LAUREA MAGISTRALE IN INGEGNERIA
ELETTRONICA E TELECOMUNICAZIONI PER LO SVILUPPO
SOSTENIBILE

TITOLO DELL'ELABORATO

Numerical simulation of interdigitated back contact hetero-junction solar cells

ELABORATO IN
Nanoelettronica L-M

Relatore:
Prof. *Claudio Fiegna*

Presentato da:
Alessandro Callozzo

Correlatore:
Dott. *Mauro Zanuccoli*

III Sessione - Anno Accademico 2011/12

Contents

Table of contents 5

Abstract 9

Introduction 11

1 Photovoltaic effect and light absorption in semiconductor materials 15

1.1 The sun . . . 15
1.2 Black body and solar spectrum . . . 15
1.2.1 Absorption in the atmosphere . . . 18
1.2.2 Rayleight scattering . . . 18
1.2.3 Air mass . . . 18
1.3 Properties of light . . . 19
1.4 Semiconductor materials . . . 20
1.4.1 Conduction in semiconductors . . . 21
1.4.2 Band structure . . . 22
1.4.3 Intrinsic concentration . . . 23
1.4.4 Doping . . . 24
1.5 Photovoltaic effect . . . 26
1.5.1 Refractive index . . . 26
1.5.2 Absorption of light in semiconductor . . . 28
1.5.3 Indirect bandgap of silicon . . . 30
1.6 Recombination mechanisms . . . 31
1.6.1 Radiative recombination . . . 32
1.6.2 Auger recombination . . . 32
1.6.3 Schokley Read Hall recombination . . . 32
1.6.4 Carrier lifetime . . . 33
1.7 Basic equations of semiconductor-device physics . . . 34
1.7.1 Poisson's equation . . . 35
1.7.2 Drift-Diffusion model . . . 35
1.7.3 Continuity equations . . . 36
1.8 Pn junction . . . 37
1.8.1 Dark characteristic . . . 39
1.8.2 Illuminated characteristic . . . 41

2 Solar cells 43

2.1 I-V characteristic . . . 43
2.1.1 Saturation current . . . 44

2.2 Other figures of merit 46
2.2.1 Trasmittance, reflectance and absorbance 46
2.2.2 Quantum efficiency 46
2.3 Efficiency limits 47
2.4 Effect of temperature 49
2.5 Efficiency losses 50
2.5.1 Short-circuit current losses 50
2.5.2 Open-circuit voltage losses 51
2.5.3 Fill Factor losses 51
2.6 Design of solar cells 52
2.6.1 Anti-reflection coating 53
2.6.2 Light trapping 53
2.6.3 Recombinations and parasitic resistances reduction 54
2.7 Advanced silicon solar cells 55
2.7.1 Interdigitated back contact 56
2.7.2 Heterojunction with intrinsic thin layer 56

3 Interdigitated back contact hetero-junction solar cells 59
3.1 Amorphous silicon 60
3.1.1 Density of states 61
3.2 JV characteristic and contact width design 62
3.3 Benefits and disadvantages of a-Si intrinsic back layer 63
3.4 Band structure analysis 64
3.5 Improving fill factor 66
3.5.1 Buffer layer conductivity 66
3.5.2 Buffer layer thickness 66
3.5.3 Back surface i-layer bandgap 67
3.6 Doped layers defects 69
3.7 Impact of c-Si resistivity 70

4 Numerical simulator 71
4.1 Sentaurus structure editor 71
4.1.1 Simulated symmetry element 72
4.2 Sentaurus device 73
4.2.1 Models implemented 74
4.3 Optical simulation 79
4.3.1 Complex refraction indexes 80
4.3.2 Transfer matrix method setting 81
4.3.3 Raytracing setting 81

5 Optical simulation **83**
5.1 Transfer Matrix Method results 84
5.2 Raytracing results 85

6 Electrical simulation **89**
6.1 Electrical simulator validation 89
6.2 Efficiency limits analysis 91
6.2.1 Homogeneous emitter HE solar cell 91
6.2.2 Heterojunction with intrinsic thin layer HIT solar cell 92
6.2.3 Interdigitated back contact hetero-junction IBC-HJ solar cell . . . 93
6.3 Impact of the back buffer layer on cell performance 94
6.4 Sensitivity on substrate resistivity 102
6.5 Sensitivity to geometrical gap value 104

Conclusion **107**

List of Figures **109**

References **112**

Sommario

In questa tesi si descrive il lavoro svolto finalizzato alla messa a punto di un flusso di simulazione numerico opto-elettronico di celle fotovoltaiche in silicio con architettura a contatto posteriore di tipo eterogiunzione (*Interdigitated Back Contact Hetero-Junction* IBC-HJ). La struttura analizzata presenta entrambi i contatti metallici, emettitore e base, nel retro della cella annullando così gli effetti di perdita ottica associati al contatto frontale. Inoltre le diffusioni caratterizzate da alte concentrazioni di drogante vengono sostituite da deposizioni di sottili strati di silicio amorfo che hanno il vantaggio di presentare un processo di fabbricazione a più bassa temperatura e quindi relativamente meno costoso rispetto alle diffusioni nel silicio cristallino.

Dopo una accurata ricerca bibliografica volta ad evidenziare le principali caratteristiche fisiche di queste strutture e le specifiche criticità, è stato messo a punto un flusso di simulazione numerico. Lo strumento utilizzato per modellare il funzionamento delle strutture considerate è il simulatore di dispositivo commerciale Sentaurus, prodotto dalla Synopsys. Il primo passo considerato nella costruzione del flusso di simulazione è stato quello di definire la geometria bidimensionale e le proprietà elettriche ed ottiche dei materiali. Per simulare il funzionamento di una cella illuminata si è dovuto anzitutto considerare l'assorbimento di fotoni da parte della struttura stessa e, di conseguenza, ricavarne la mappa di generazione ottica di coppie elettroni e lacune.

La simulazione ottica è stata eseguita con due differenti metodi: il metodo delle matrici di trasferimento (*Transfer Matrix Method* TMM) e quello del tracciamento dei raggi (*Raytracing* RT). Il primo metodo è in grado di trattare domini spaziali di simulazione monodimensionali ed è stato utilizzato per la simulazione di dispositivi con interfacce parallele e planari. Il metodo di tracciamento dei raggi è stato invece utilizzato con successo per la simulazione ottica tridimensionale di superfici texturizzate che hanno la caratteristica di ridurre sensibilmente la riflessione della radiazione solare incidente alla superficie frontale. Il profilo di generazione ottica è stato poi importato nel simulatore elettrico per effettuare la soluzione numerica autoconsistente delle equazioni del trasporto dei portatori in accoppiamento alle equazioni di Poisson e di continuità. Il risultato della simulazione elettro-ottica è stato quindi utilizzato per calcolare le principali figure di merito del dispositivo fotovoltaico.

Dopo aver validato il modello, confrontando i risultati ottenuti con quelli presenti in letteratura, l'obiettivo è stato quello di mettere in evidenza potenzialità e criticità di questo tipo di dispositivo. Per questo tipo di analisi è emerso che le celle IBC-HJ presentano un

limite massimo di efficienza superiore sia a quello delle celle convenzionali omogiunzione in silicio cristallino (*Homogeneous Emitter* HE) sia a quello di celle eterogiunzione con contatti frontali (*Heterojunction with Intrinsic Thin layer* HIT). D'altra parte è anche evidente che le criticità di questa struttura sono dovute alla difettosità e alla limitata mobilità di trasporto dei portatori negli strati di silicio amorfo. Infine sono stati considerati i principali parametri geometrici e fisici ed al variare di quest'ultimi, all'interno di intervalli realistici di possibili valori, sono state calcolate le principali figure di merito della cella.

Abstract

The goal of this thesis is the application of an opto-electronic numerical simulation to heterojunction silicon solar cells featuring an all back contact architecture (*Interdigitated Back Contact Hetero-Junction* IBC-HJ). The studied structure exhibits both metal contacts, emitter and base, at the back surface of the cell with the objective to reduce the optical losses due to the shadowing by front contact of conventional photovoltaic devices. Overall, IBC-HJ are promising low-cost alternatives to monocrystalline wafer-based solar cells featuring front and back contact schemes, in fact, for IBC-HJ the high concentration doping diffusions are replaced by low-temperature deposition processes of thin amorphous silicon layers. Furthermore, another advantage of IBC solar cells with reference to conventional architectures is the possibility to enable a low-cost assembling of photovoltaic modules, being all contacts on the same side.

A preliminary extensive literature survey has been helpful to highlight the specific critical aspects of IBC-HJ solar cells as well as the state-of-the-art of their modeling, processing and performance of practical devices. In order to perform the analysis of IBC-HJ devices, a two-dimensional (2-D) numerical simulation flow has been set up. A commercial device simulator based on finite-difference method to solve numerically the whole set of equations governing the electrical transport in semiconductor materials (Sentuarus Device by Synopsys) has been adopted. The first activity carried out during this work has been the definition of a 2-D geometry corresponding to the simulation domain and the specification of the electrical and optical properties of materials. In order to calculate the main figures of merit of the investigated solar cells, the spatially resolved photon absorption rate map has been calculated by means of an optical simulator.

Optical simulations have been performed by using two different methods depending upon the geometrical features of the front interface of the solar cell: the transfer matrix method (TMM) and the raytracing (RT). The first method allows to model light propagation by plane waves within one-dimensional spatial domains under the assumption of devices exhibiting stacks of parallel layers with planar interfaces. In addition, TMM is suitable for the simulation of thin multi-layer anti reflection coating layers for the reduction of the amount of reflected light at the front interface. Raytracing is required for three-dimensional optical simulations of upright pyramidal textured surfaces which are widely adopted to significantly reduce the reflection at the front surface. The optical generation profiles are interpolated onto the electrical grid adopted by the device simulator which solves the carriers transport equations coupled with Poisson and continuity equations in a self-consistent way. The main figures of merit are calculated by means of

a postprocessing of the output data from device simulation.

After the validation of the simulation methodology by means of comparison of the simulation result with literature data, the ultimate efficiency of the IBC-HJ architecture has been calculated. By accounting for all optical losses, IBC-HJ solar cells result in a theoretical maximum efficiency above 23.5% (without texturing at front interface) higher than that of both standard homojunction crystalline silicon (*Homogeneous Emitter* HE) and front contact heterojuction (*Heterojunction with Intrinsic Thin layer* HIT) solar cells. However it is clear that the criticalities of this structure are mainly due to the defects density and to the poor carriers transport mobility in the amorphous silicon layers. Lastly, the influence of the most critical geometrical and physical parameters on the main figures of merit have been investigated by applying the numerical simulation tool set-up during the first part of the present thesis. Simulations have highlighted that carrier mobility and defects level in amorphous silicon may lead to a potentially significant reduction of the conversion efficiency.

Introduction

Electrical power nowadays is essential in most of the human being activities. Its consumption has been grown exponentially in the last decades, in fact the world power demand raised from about 5 TW in the 1960s to over 18 TW in the 2010s. Electric energy can be obtained only by means of transformation of others energy. Many natural sources are suitable to this purpose including but not limited to fossil fuel, coal, nuclear energy, natural gas, geothermal, hydroelectricity, wind and sun. Conventional power plants, which use fossil fuels such as coal, oil or nuclear materials are able to produce high amount of power. On the other hand, they also produce elevated polluting emissions and use, as raw materials, limited natural resources, whose cost constantly raises. Fossil fuel power plants involve a combustion which leads to a harmful CO_2 emission. Earth temperature is linked to a balance between incoming and outcoming solar energy, which depends on the atmosphere composition. Human activities increase the anthropogenic gases (such as carbon dioxide, methane, ozone, nitrous oxides and chlorofluorocarbons) released into the atmosphere, which potentially lead to an increase in terrestrial temperature; such phenomenon is called Greenhouse effect, it causes the global warming and results in several other effects, such as rainfalls and wind patterns modifications.

Renewable energy sources include those derived from natural sources such as sun, wind, waves, tides or geothermal heat. Advantages of renewable energy sources are that i) they are not limited sources, ii) they do not produce any polluting waste and iii) no gases emission occurs; thanks to such reasons, over the time, governments of most countries around the world have enhanced their energy legislation and green incentives toward an increase of the amount of energy produced from natural sources.

The most direct way to convert solar energy into electrical energy is that involving the photovoltaic technologies which lead to several advantages: theoretical unlimited amount of available energy, absence of gas emission, easy integration in building as well as low operative and maintenance expense. Furthermore, they produce the maximum possible power during the central hours of the day, which correspond to the maximum consumption time. However, there are some disadvantages: i) the light radiation has random intensity over the time, therefore it is not very reliable and ii) its cost is still very high. The goal of future photovoltaic devices is to be cheaper, thanks to the reduction of both production and installation costs, but with a higher conversion efficiency.

The Shockley-Queisser limit evaluates the maximum theoretical efficiency of a solar cell, which is 33.7% achieved by a single pn junction with a bandgap width of 1.34 eV. A silicon solar cell has an efficiency limit of about 29%, however, under practical conditions, such value degrades by means of different loss mechanisms. The main loss phenomena, optical and electrical both, are: i) reflection at the front surface, ii) front contact shadowing, iii) bulk and interface recombinations and iv) parasitic resistances.

Standard crystalline silicon solar cells have been studied for over 50 years, hence their practical performance is close to the upper bound limit. However, toward the objective of reducing the cost-per-watt of photovoltaic technology, new materials and architectures have to be investigated since the conversion efficiency of current commercial silicon solar cells is 22.5% at module level. The topic of this thesis is the analysis and simulation of the interdigitated back contact hetero-junction IBC-HJ solar cells which is one of the most promising architecture to achieve relatively high efficiency by using low-cost processing techniques. However, exactly as for their homojunction counterparts or as for HIT solar cells, also IBC-HJ solar cells design have to be optimized by properly sizing all geometrical parameters as well as the quality of the materials and processes involved in their fabrication. Numerical simulations are helpful to model and optimize solar cells for which several competing physical mechanisms have to be accounted for in order to predict realistic values of the figures of merit.

In the **first section** a brief description of physical properties, which are necessary to understand the working principle of solar cells, are presented: sun and sunlight features, photovoltaic effect, semiconductor properties and pn junction behaviour. The main equations for their mathematical description are presented as well. Electrical loss mechanisms are introduced as well as their physical explanations.
In the **second section** the working principle of a solar cell is outlined. In the first part a typical current-voltage (I-V) characteristic is described as well as all the main figures of merit. In addition, the influence of temperature and of other critical physical parameters on the figures of merit is discussed. A theoretical upper bound limit of efficiency is calculated according to the well-known methodologies proposed in literature. In the last part of section two some promising advanced architectures of silicon based solar cells are outlined.
In the **third section** IBC-HJ solar cells are extensively described. The results of a literature survey are summarized to discuss the state-of-the-art of IBC-HJ solar cells manufacturing, performance and modeling.

In the **fourth section** the main features of Sentaurus, the numerical simulator by Synopsys which has been adopted for the modeling activity in this thesis, are described. Furthermore, the simulation methodology and the flow adopted for both optical and electrical TCAD simulations are described. Particular emphasis is given to the description of the physical and electrical models adopted in this theoretical study.
The results of performed optical simulations of solar cells exhibiting textured and planar front surfaces are discussed in the **fifth section**.
In the **sixth section** the results of the electrical simulations are extensively discussed. In particular, the numerical simulation flow has been applied in order to investigate the sensitiveness of some crucial physical and geometrical parameters on the main figures of merit; such parameters play a role of paramount importance in determining the overall cost-performance trade-off in the design of the device.

1 Photovoltaic effect and light absorption in semiconductor materials

1.1 The sun

Solar energy is produced into the sun, where thermonuclear reactions are possible thanks to temperature above 13 millions degree and pressure of 500 billion of atmosphere. In those conditions hydrogen protons can fuse into helium releasing large amount of energy; this radiation from the core is not visible because it is heavily absorbed by a layer of hydrogen. The heat produced in this layer is trasfered through the convective zone of the sun by thermal convection. The external temperature of the sun drops to 5700K and the estimated emitted power is approximately 383YW (Yotta = 10^{24}). The energy that reach our atmosphere can be easily calculated by means of the knowledge of the Earth radius and the distance between the star and our planet.

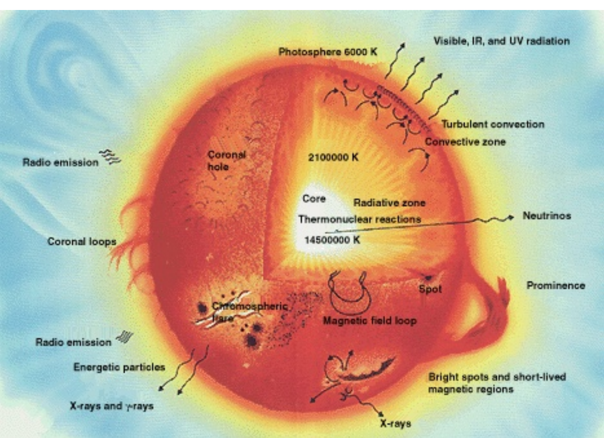

Figure 1: Sun regions (from wikipedia).

Half of the 174PW (Peta = 10^{15}) incoming solar power that hits our planet is lost in the atmosphere because of reflection and absorption phenomena caused by clouds, earth surface and the atmosphere itself (as discussed in the following paragraph). The remaining solar energy is the most powerful renewable energy source, in fact in less than an hour arrives to the Earth more energy than was consumed by the entire world in a year. However, the amount of available energy is only theoretical since that energy cannot be completely used and its intensity is subject to time variations.

1.2 Black body and solar spectrum

A black body is an ideal object that absorbs the entire incident spectrum end emits electromagnetic radiation in according to the Planck's law (1), for which the emitted

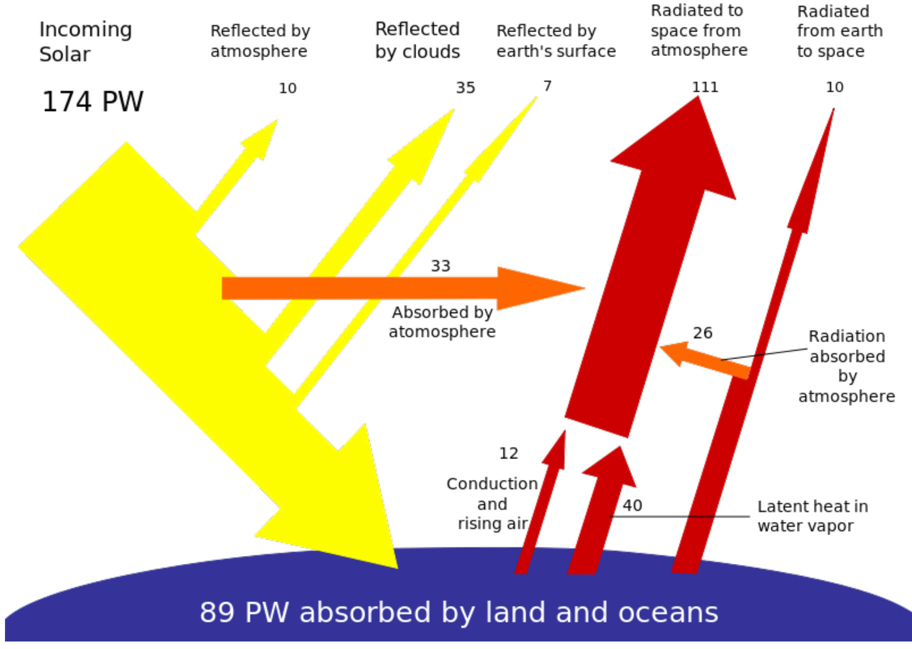

Figure 2: Solar power balance through the atmosphere (from wikipedia).

spectrum depends only on the body temperature:

$$B_\lambda(T) = \frac{2hc^2}{\lambda^5}\frac{1}{e^{\frac{hc}{k\lambda T}} - 1}, \tag{1}$$

where B is the spectral irradiance (energy per unit surface area, time and solid angle emitted at a wavelength λ), T is the absolute temperature of the black body, k is the Boltzmann constant, h is the Planck constant and c is the speed of light in vacuum:

$$k = 1.381 \cdot 10^{-23}[\mathrm{J} \cdot \mathrm{K}^{-1}] = 8.617 \cdot 10^{-5}[\mathrm{eV} \cdot \mathrm{K}^{-1}], \tag{2}$$

$$h = 6.626 \cdot 10^{-34}[\mathrm{J} \cdot \mathrm{s}] = 4.136 \cdot 10^{-15}[\mathrm{eV} \cdot \mathrm{s}], \tag{3}$$

$$c = 2.998 \cdot 10^{8}[\mathrm{m} \cdot \mathrm{s}^{-1}]. \tag{4}$$

A black body has two important properties: i) it is an ideal emitter, since it emits the maximum possible energy for a body at that temperature, and ii) it is a diffuse emitter, therefore, its energy is isotropicaly radiated. The total power density of a black body is calculated by integrating the spectral irradiance over all wavelengths, according to the Stefan–Boltzmann's law:

$$I = \sigma T^4, \tag{5}$$

where σ is the Stefan's constant,

$$\sigma = 5.670 \cdot 10^{-8} [\mathrm{W} \cdot \mathrm{m}^{-2} \cdot \mathrm{K}^{-4}]. \tag{6}$$

Another important parameter, which can be derived from the Wien's law (7), is the wavelength at which most of the power is emitted:

$$\lambda_{max} = \frac{b}{T}, \tag{7}$$

where b is the Wien's displacement constant,

$$b = 2.898 \cdot 10^{-3} [\mathrm{m} \cdot \mathrm{K}]. \tag{8}$$

The concept of black body was introduced because Sun and Earth's surface behave approximately as black bodies. Their solar spectral irradiance can be estimated (similarly to any other body with temperature above the absolute zero) by means of a black body at a certain temperature, called effective temperature, which emits the same amount of electromagnetic radiation. The sun is assumed to behave similarly to a black body with a temperature of $5777K$ Fig. 3. The incident radiation on the Earth is relatively con-

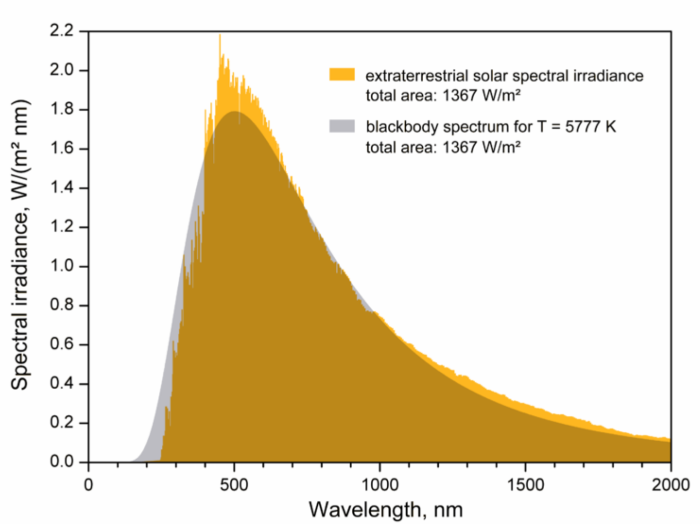

Figure 3: Solar spectrum compared to black body spectrum (from wikipedia).

stant, however, that on the Earth's surface is widely dependent on atmospheric effects, like absorption, scattering and local variations (clouds, water vapour and pollution); It also depends on the latitude of the considered location, the season of the year and the time of day. The variation does not involve just the overall received power but also the spectral content and the incident angle of the light on the Earth surface.

1.2.1 Absorption in the atmosphere

Specific gasses, like ozone (O3), carbon dioxide (CO2), and water vapour (H2O), exhibit very high photon absorption for energy close to the bond energies of these atmospheric gases yielding to deep troughs in the spectrum Fig. 4 that change the spectral content.

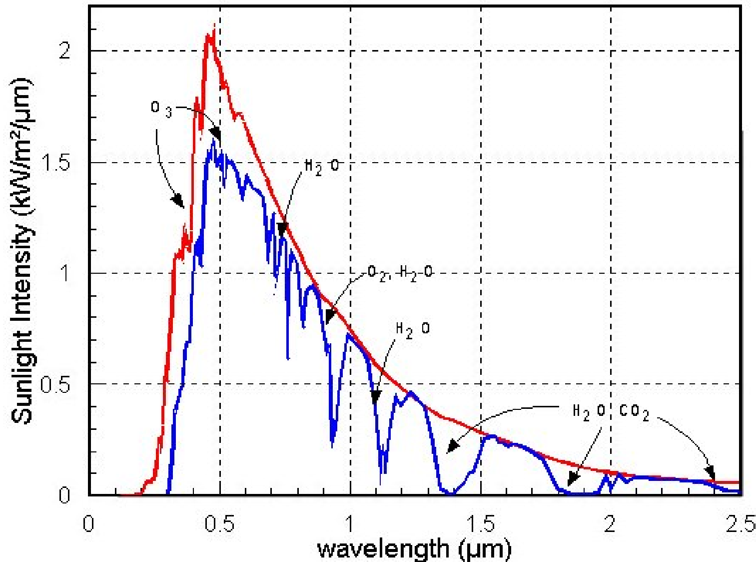

Figure 4: Effect of the atmosphere on the solar spectrum [3].

1.2.2 Rayleight scattering

When the wavelength exhibits dimensions comparable to the size of the particles, the light is subject to another important effect caused by scattering of molecules from the atmosphere. Such phenomenon is very effective at short wavelengths and the rays resulting from scattering form the diffused component of light, also called indirect component. The reason why sky is blue is that the prevalent contribution to diffused component comes from the blue wavelengths (the shortest of the visible spectrum); since direct light is deprived of the blue part of the visible spectrum the Sun appears to be yellow. Other kinds of scattering effects exist between dust and aereosols particles. On a clear day about 10% of the total incident light is diffused, however the intensity of the diffused component increases markedly during cloudy days.

1.2.3 Air mass

Air mass (AM) coefficient characterizes the path of light through atmosphere. It is defined from a reference point on the earth surface as the ratio between the real path to reach that point and the shortest path possible (with the sun at zenith position). It helps to quantify the reduction of light power when it passes through the atmosphere and is subject to all the phenomena described above. Higher is the AM coefficient, lower

is the intensity of the sunlight, which is maximum when the sun is at the zenith position:

$$AM = \frac{\text{light path}}{\text{minimum path}} = \frac{1}{\cos\theta}, \tag{9}$$

where θ is the zenith angle. Another way to calculate the AM coefficients is that off considering an obstacle and its shadow as shown in Fig. 5, simply adopting the Pythagoras theorem:

$$AM = \sqrt{1 + \left(\frac{s}{h}\right)^2}. \tag{10}$$

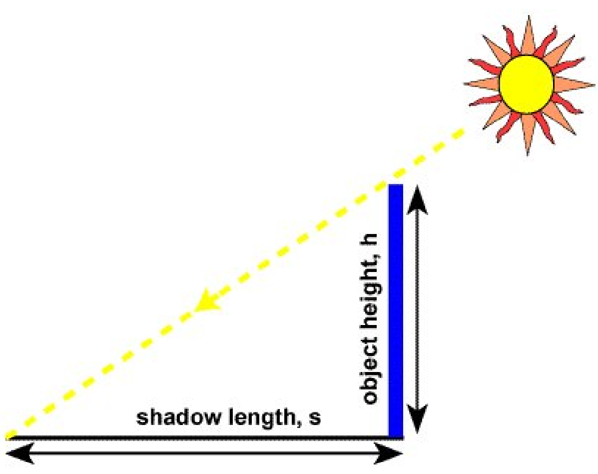

Figure 5: Calculation of the air mass coefficient [3].

The air mass coefficient is commonly used to characterize the performance of solar cells under standardized conditions, therefore a standard reference spectrum AM1.5 at the Earth surface is needed, which is called ASTM G173 − 03 [6]. The accounted spectrum features are: irradiation of $1000\,[\mathrm{W}\cdot\mathrm{m}^2]$, incident angle θ of $48,19^{\circ}$ (typical of mid-latitudes location like Europe, China, Japan, United States of America and many other) and temperature of 25°C.

1.3 Properties of light

The knowledge of light properties is necessary to understand the photovoltaic effect and the operating principles of solar cells. In the 19th century the wave-based model of light showed discrepancy between theory and experiments and it was clear that something was missing. In the 1900, thanks to Planck's research, evidence that light was made of indistinguishable energy element was found; later, Einstein correctly understood the value of this quantum energy elements. Problems with the latter theory were overcomed with the introduction of elementary particles called *photons* and a brand new way to see the light as a consequence.

Quantum mechanics nowadays can explain both wave and particles behaviour of light

by considering photons (as the other particles) as wave-packets, which are a collection of waves that can be treated in some case like waves and in others can be localized like particles.
A photon, as the other quantum particles, is defined by an energy E and a momentum $\vec{p}$, the first is a function of wavelength and the second of the wavevector $\vec{k}$:

$$E = hf = \frac{hc}{\lambda}, \tag{11}$$

$$\vec{p} = \hbar\vec{k}, \tag{12}$$

where h is the Planck's constant (3) and c is the speed of light (4). It is worth noticing that energy is inversal proportional to λ. The optical flux defines the number of photons impingin an interface during a certain amount of time:

$$\Phi = \frac{\text{number of photons}}{s \cdot m^2}. \tag{13}$$

Photon flux does not give information about energy but it is necessary in order to calculate the power density. Which can be obtain by multipling the number of photons hitting a surface per time unit with the photon energy:

$$H = \Phi \cdot \frac{hc}{\lambda}. \tag{14}$$

The general formula of the spectral irradiance can be defined as:

$$B_\lambda = \Phi \cdot E \cdot \frac{1}{\Delta\lambda}. \tag{15}$$

1.4 Semiconductor materials

In this section a brief introduction to physical properties of semiconductor materials will be presented. Semiconductors exhibit a conductivity whose value is between that of insulators and conductors. Pure semiconductor elements are in the fourth group of the periodic table (Fig 6) or can be either a compound of different elements (like AsGa, CdTe or InP) or an alloy. Silicon is the most common semiconductor material, used in electronic since its very beginning because of its interesting properties.
The atom structure consists in a core of protons and neutrons surrounded by electrons, however equal number of electrons and protons is necessary to maintain the electrical charge neutrality. Silicon valence number is 4 therefore, the third orbital is half full and it is be always tetravalentic bonded. The outer electrons recombine to generate new isoenergetic orbitals featuring different shapes leading to a phenomenon called hy-

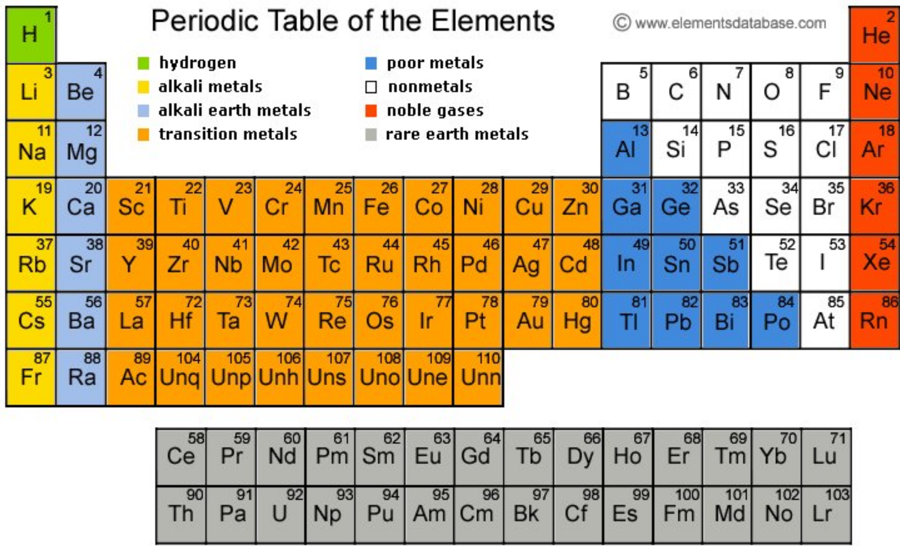

Figure 6: Periodic table of the elements [5].

bridization, which may occur in different ways however, in case of a silicon crystal, the shape of the orbital (shown in Fig. 7) that of the sp^3 hybridation.

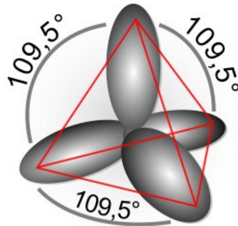

Figure 7: sp^3 type hybridation (from wikipedia).

Two sp^3 hybrid silicon atoms are bounded together with all σ bounds, which are the strongest type of covalent chemical bond coming from a direct overlap between atomic orbitals. Such orbitals form four full molecular bounds and four empty molecular anti-bounds; of course all the free electrons tend to lower energy states called HOMO (highest occupied molecular orbital), whereas the empty states are called LUMO (lowest unoccupied molecular orbital). The extension to a large number of silicon atoms leads to a continuous distribution of possible states, which is the concept of band theory. Another important property of semiconductor materials is the possibility of improving the current conduction by adding impurities in the crystal structure.

1.4.1 Conduction in semiconductors

Electrons collocated into the crystal structure cannot contribute to the current flow, because of the covalent bond between the silicon atoms that hold them in place, therefore they are localized within the atoms. This could be true only at absolute zero temperature

where there is no thermal energy and, for this reason, electrons can be considered totally blocked. At room temperature, instead, charge carriers can gain enough energy to free itself from the bonding. Thanks to the lattice thermal vibrations they can move in the crystal lattice and even contribute to the electrical transport. Two different states can be distinguished: a free state and a blocked state. Free charges have more energy than blocked ones and no intermediate levels of energy are possible. Electrons can just gain the proper amount of energy to reach the higher level or alternatively lose enough energy to fall into the lower level, energy surplus is therefore wasted. The number of free electrons is a very important parameter for all the operations of the electronic devices. The space left behind by an electron that frees itself is considered as a particle called hole. All the electrons still bind to the silicon crystal move into this space giving the appearance of a positive charge in motion, therefore holes take part in the semiconductor conduction.

1.4.2 Band structure

In silicon crystal lattice there is a superimposition of LUMO and HOMO energy levels, that leads to a continuous distribution of allowed states to electrons. These bands of allowed energies have been defined as *valence band*, which has the meaning of the highest occupied energy, and *conduction band*, which is the lowest free energy. Between them there is a band of forbidden energy called bandgap. More precisely a band is a range of energy that an electron in a certain material is allowed to have, derived from the Bloch's theorem. As direct consequence of this theorem all the bands for a given structure can be occupied. Theory assigns an infinite number of bands for each material but most of them have higher energy compared to the vacuum level. These could be ignored because an electron with such a high energy is no longer bind to the lattice. The vacuum energy can be derived from the sum of two characteristic energy levels. One of these levels, is the Fermi level defined as the highest occupied energy in a fermionic system at the absolute zero. A fermionic system is a class of particles that follows the Pauli's exclusion principle. As shown in Fig. 8, at ambient temperature some thermal energy is provided to the crystal structure and the Fermi level is no longer occupied, it is somewhere into the bandgap. It is worth noticing that this is not true for metal materials, for which even at absolute zero temperature conduction of current is possible. The other characteristic energy is the workfunction, which is the minimal energy that has to be given to an electron in order to extract it out of the material.
Electrons will fill bands following the Fermi-Dirac statistical distribution, if a band is not completely occupied this material is a conductor because electrons can move easily between very close energy levels and leading to high electrical mobility. Otherwise if the last occupied band is completely full the material could be either an insulator or

a semiconductor. The bandgap width allow to classify the different kinds of material. Insulators have large bandgaps, hence it is very difficult for a charge to obtain enough energy to break the covalent bond. Insulators are materials with low mobility and a very poor concentration of charge into the conduction band. The bandgap width of a semiconductor is not high as that of an insulator, therefore, it is possible for a charge to reach the conduction band and, even with thermal energy corresponding to room temperature, the concentration of free carriers is not zero. However, excitation of an

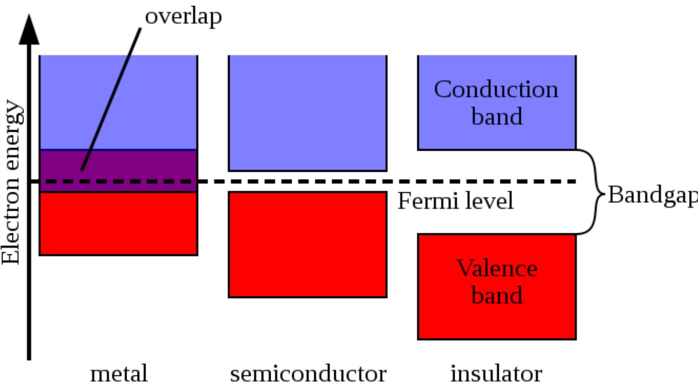

Figure 8: Band structure of metals, insulators and semiconductors (from wikipedia).

electron results not only in the presence of itself in the conduction band but also in the presence of a positive pseudo particle in the valence band.

1.4.3 Intrinsic concentration

A semiconductor without the addition of impurities is called intrinsic. The number of holes and electrons in valence and conduction band, respectively, depends on the bandgap width and on the crystal lattice temperature. Fermi statistics defines the occupation of the electronic states:

$$f(E) = \frac{1}{1 + e^{\frac{E-E_F}{kT}}}, \tag{16}$$

where E is the energy of the electron, E_F is the Fermi level and k is the Boltzmann constant. E_F is the energy at which the occupation probabilities pass from about one to almost zero and it depends on temperature. The density of charge carriers, both electrons n and holes p, can be calculated by:

$$n = \int_{E_C}^{\infty} f(E) g_C(E) dE, \tag{17}$$

$$p = \int_{-\infty}^{E_V} (1 - f(E)) g_V(E) dE, \tag{18}$$

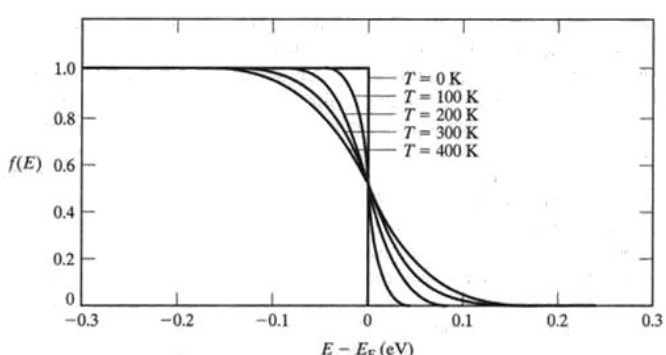

Figure 9: Fermi statistic (from wikipedia).

where E_C and E_V are respectively the energies of conduction and valence band, g_C and g_V are the densities of allow states into the respective band (shown in Fig. 11). All the calculation steps will be omitted and the resulting carrier densities are:

$$n = N_C e^{\frac{-(E_C - E_F)}{kT}}, \tag{19}$$

$$p = N_V e^{\frac{-(E_F - E_V)}{kT}}, \tag{20}$$

where N_C and N_V are the effective density of states in band. An intrinsic semiconductor has the same number of electrons and holes:

$$n = p = n_i = \sqrt{N_C N_V} e^{\frac{(E_V - E_C)}{2kT}}, \tag{21}$$

the density of carriers decrease exponentially with an increasing bandgap and a reduction of temperature.

1.4.4 Doping

In order to improve the conduction of a semiconductor material, a doping process is necessary. A doped silicon crystal lattice is obtained with the introduction of impurities, relatively small concentration of atoms from the third or the fifth group of the periodic table. Silicon atoms have four electrons available for covalent bonds, therefore, if an atom with five as valence number is added in the structure (e.g. Phosphorous), four electrons are bounded while the other one is free to move and it contributes to conduction. Holes are free charge carriers as well and also their concentration in the valence band can be increased; to that purpose, an impurity of the third group (e.g. Boron) can be introduced in the crystal lattice. In this situation an electron is missing, hence not all the four covalent bonds are formed leading to the creation of a hole. In doped materials,

concentration of carries is always different: in p-type materials holes are the majority carriers while electrons are the minority ones. In n-type semiconductors it is the opposite.

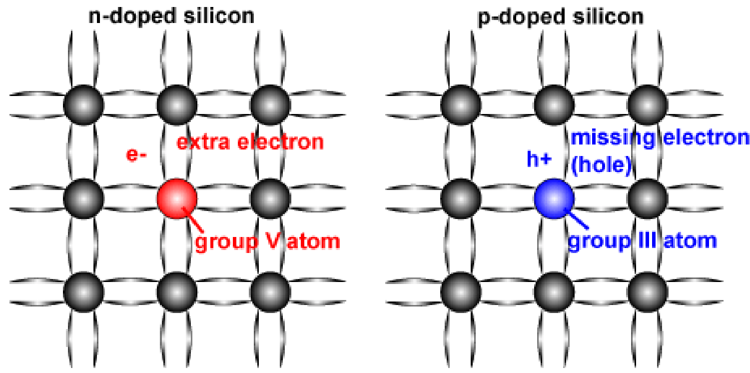

Figure 10: Doped silicon structure [3].

Concerning the band structure, a doping process creates allowed energy states into the bandgap but very closed to conduction band (n-type doping) or valence band (p-type doping) edges. Such states of energy are very close to their respective band, therefore, a little energy is required in order to ionize the dopant atoms and to create a free carrier; for such purpose the room temperature is usually enough. Fig. 11 shows the density of states for different kinds of materials.

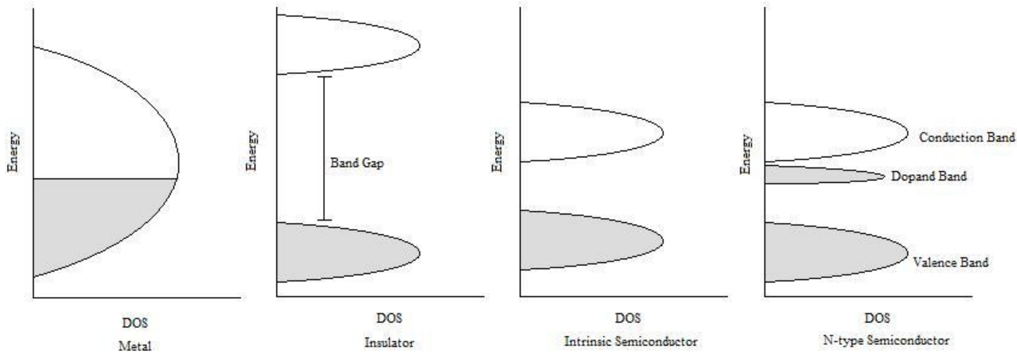

Figure 11: Comparison between density of states DOS (from wikipedia).

In the following carriers concentration will be calculated in equilibrium case, when no external bias is applied to the structure. In this case the product of majority by minority carriers is constant and defined by the mass action law:

$$n_0 p_0 = n_i^2, \tag{22}$$

where n_0 and p_0 are the electrons and the holes density at equilibrium conditions, respectively. Majority carriers concentration is equal to the sum of intrinsic and doping

concentration both, however it can be approximated without considering n_i because it is typically several magnitude orders lower. From (22) also the minority concentration can be derived. For n-type doped materials:

$$n_0 = N_D, \tag{23}$$

$$p_0 = \frac{n_i^2}{N_D}, \tag{24}$$

where N_D is the concentration of donor-like dopant atoms; similarly for p-type semiconductors:

$$p_0 = N_A, \tag{25}$$

$$n_0 = \frac{n_i^2}{N_A}, \tag{26}$$

where N_A is the concentration of acceptor-like dopant atoms. Those equations show that minority concentration decreases with doping density because, for instance in case of a n-type material, part of the free electrons occupy some of the holes.

1.5 Photovoltaic effect

The photovoltaic effect is a direct way by which the radiation from the Sun can be converted in electric energy. This phenomenon was first observed by Becquerel in 1839 and later a complete physics explanation was proposed by Einstein in the 1905. Under certain conditions, an incident electromagnetic radiation can provide enough energy to the external electrons to free themselves from the structure. Photon energy depends only on his wavelength, as shown in equation (11). The intensity of the incoming light indicates the number of the incident photons.

1.5.1 Refractive index

When a ray hits an interface between two media (which are, typically, in photovoltaic devices air and silicon) it is split into two components, one reflected and the other one transmitted through the crystal lattice. Assuming that the silicon thickness is infinite, only light which is not reflected is available for electron-holes generation and the refractive index help to quantify intensity and direction of these two components. As shown in Fig. 12, this index is a complex number ($n_c = n - ik$), where its real part n is the factor by which the velocity of the radiation is reduced with respect to the speed of light in vacuum c; by means of the Snell's law it is possible to calculate the incidence angle of a transmitted ray, the knowledge of the incident ray angle and the refraction

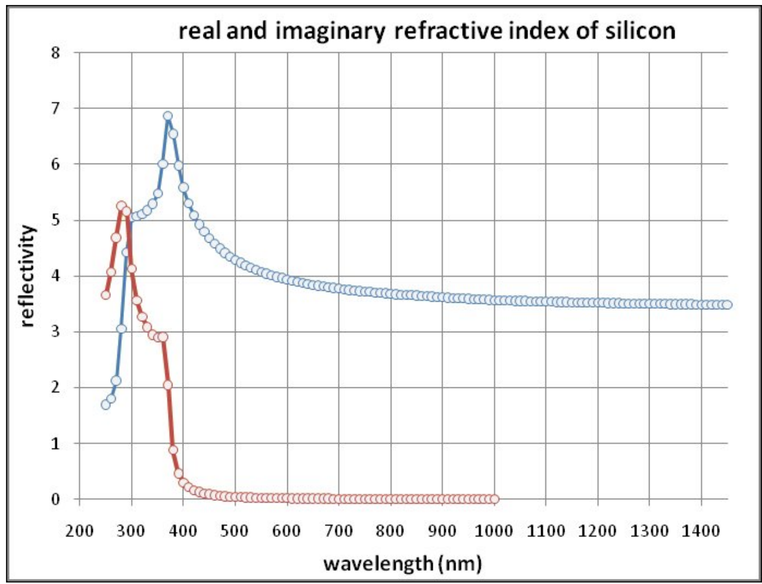

Figure 12: Real and complex part of the silicon refractive index [3].

index n of the two medium it is necessary:

$$n_1 \sin \phi_1 = n_2 \sin \phi_2. \tag{27}$$

The reflected and transmitted light intensity have to be calculated by Fresnel's law.

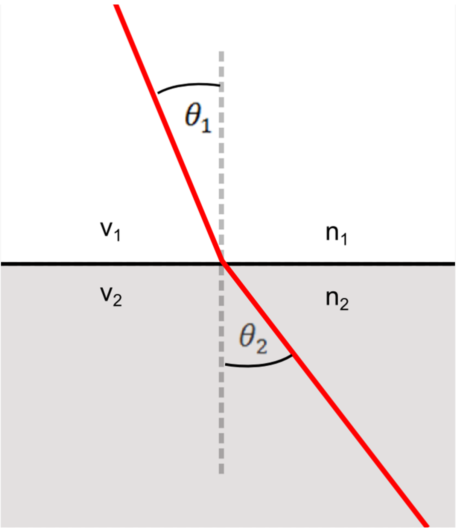

Figure 13: Incident and transmitted ray at an interface [3].

Reflection index R is defined as the ratio between the intensity of reflected and incident radiation while the trasmission index T is the ratio between transmitted and incident intensities. A simplified expression is given under the assumption that light rays are almost perpendicular at the surface ($\phi_1 = \phi_2 = 0$):

$$R = \left(\frac{n_1 - n_2}{n_1 - n_2} \right)^2, \tag{28}$$

$$T = \frac{4n_1 n_2}{(n_1 + n_2)^2}. \tag{29}$$

The imaginary part k indicates the extinction factor, which is the absorption which every wave passing through a material is subject to; when k is above zero there is an attenuation of light intensity, if k is zero the ray pass through without absorption. The value of n and k are expressed as a function of real and imaginary part of permettivity ε of the two materials:

$$n = \sqrt{\frac{\sqrt{\varepsilon_1^2 + \varepsilon_2^2} + \varepsilon_1}{2}}, \tag{30}$$

$$k = \sqrt{\frac{\sqrt{\varepsilon_1^2 + \varepsilon_2^2} - \varepsilon_1}{2}}, \tag{31}$$

where ε_1 and ε_2 are the real and the imaginary parts, respectively, of the permettivity.

1.5.2 Absorption of light in semiconductor

If a photon is absorbed, it has a chance to excite an electron from the valence to the conduction band and the probability of this transition depends on its energy E_{ph}. It is worth considering three case: if E_{ph} is minor than the bandgap width E_g, the photon is not absorbed and it passes through the semiconductor; if E_{ph} is greater than E_g the photon is absorbed and an electron-hole pair is photo-generated; lastly, when carriers gain more energy than that corresponding to the edge of the conduction band, the probability of transition increases but all the energy in excess is wasted releasing thermal energy. Such effect creates both majority and minority carriers, but the majority photo-carriers are order of magnitude less than that doping concentration.

The probability for a photon to be absorbed is proportional to its energy and higher energy means lower wavelength. Blue light is, therefore, absorbed closer to the silicon interface than red light. An *absorption coefficient* α can be defined as a measure of how far photons penetrate into the material. After a certain radiation wavelength, corresponding to a determinated energy, the value of α drops to zero because the bandgap cannot be overcomed. That is because, in order to allow a possible band to band transition, when a photon has an energy equal to the bandgap, an electron should have its energy corresponding to the edge of the valence band and move to the edge of the conduction band, that is quite unlikely. However, α depends also on the physical characteristics of the material. The absorption coefficient can be calculated as:

$$\alpha = \frac{4\pi k}{\lambda}. \tag{32}$$

The coefficient α depends on k, which is the extinction coefficient defined in the previous subsection.

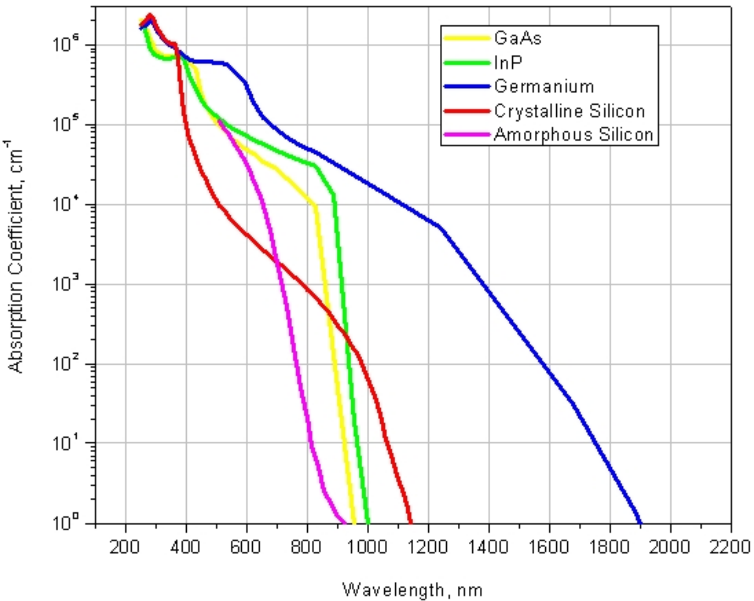

Figure 14: Comparison between absorption coefficient of various materials [3].

The *absorption length* is defined as α^{-1}, it indicates the length of the path within light intensity (for a given wavelength) drops of an $1/e = 36\%$ factor. Light intensity, at the depth x from the interface, can be calculated thanks to the Lambert-Beer's law and it depends on the depth of penetration along the material:

$$I(x) = I_0 e^{-\alpha x}, \tag{33}$$

where I_0 is the light intensity at the surface. The absorption of light into the material attenuates the intensity, assuming that this is directly correlated to the generation of electron-hole pairs the optical generation rate can be calculated. By considering a lossy thin slice of material and by differentiating the equation (33), the *optical generation rate* at any point of the device can be express as:

$$G(x) = \alpha \phi_0 e^{-\alpha x}, \tag{34}$$

where ϕ_0 is the photon flux at the surface. The incident light on a surface is a superimposition of different wavelengths. Intensity of these monochromatic components decreases exponentially into the material and the associated optical generation rate is higher at the device surface.

1.5.3 Indirect bandgap of silicon

Band structure in Fig. 8 is a very simplified model, in fact E_V and E_C energy values only represent the bands edge. The knowledge of the real material band structure is necessary to understand the quantum mechanics. Block's waves can represent an electron into the crystal only if the Schrodinger equations are satisfied with a given potential energy of the periodic lattice. In order to obtain a not zero solution, for a given wave vector k, only specific energy values E are possible, which are the only allowed energies for this electron. The periodic function $E(\vec{k})$, which is called *dispersion relation* of the wave, represents an electron in the crystal; in Fig. 15 the silicon band structure is shown as example.

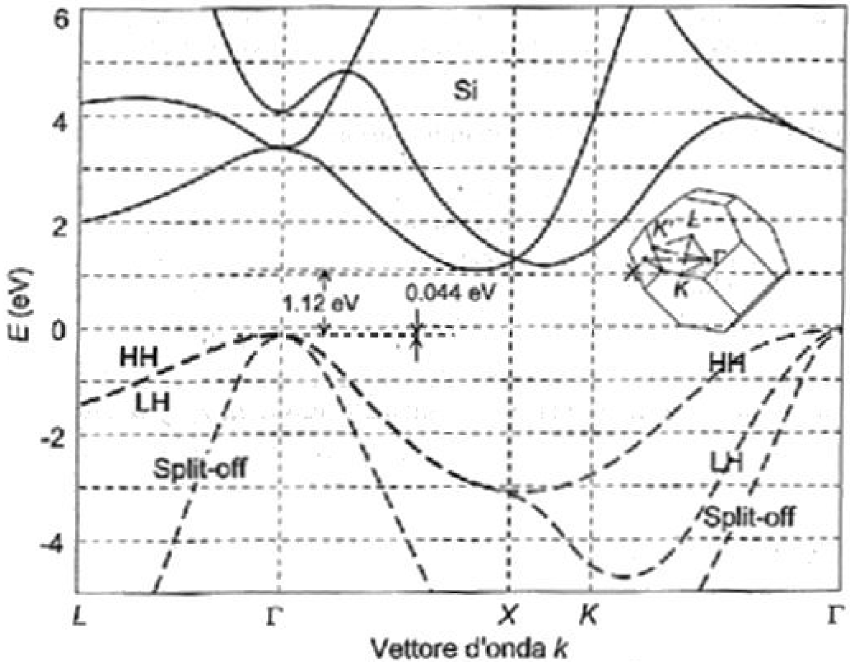

Figure 15: Dispersion relationship of silicon crystal lattice [1].

The minimum energy transition starts from the highest energy in the conduction band and ends in the lowest energy in the valence band. It is simple noticing that it is not possible only with an energy variation, since the two states lie at different values of k. A photon, when is absorbed, can provide just an improve of energy but its momentum has a negligibly small value. It is possible for an electron to gain a momentum with an interaction between itself and the crystal lattice, whose vibration motion, due to thermal energy, is propagating in the structure. A quantum mechanics energy exchange is possible with discrete packets, called *phonon*. A phonon is a boson which has a low energy and a considerable momentum. The mechanism of absorption assisted by a phonon is typical of materials with indirect bandgap, like silicon. It consist of a photon

absorption followed by a phonon absorption or emission:

$$E_{photon} \pm E_{phonon} \geq E_g. \tag{35}$$

The probability of this kind of transition is negligible compared to that of a direct one. Direct absorptions can occur as well in silicon but with higher energies than E_g, therefore, they are usually localized very closed to the front interface. Indirect mechanisms involve lower energy (higher wavelength) and occur deeper into the material. Also semiconductors with direct band gap exist, like AsGa, in which the phonon assisted generation is negligible.

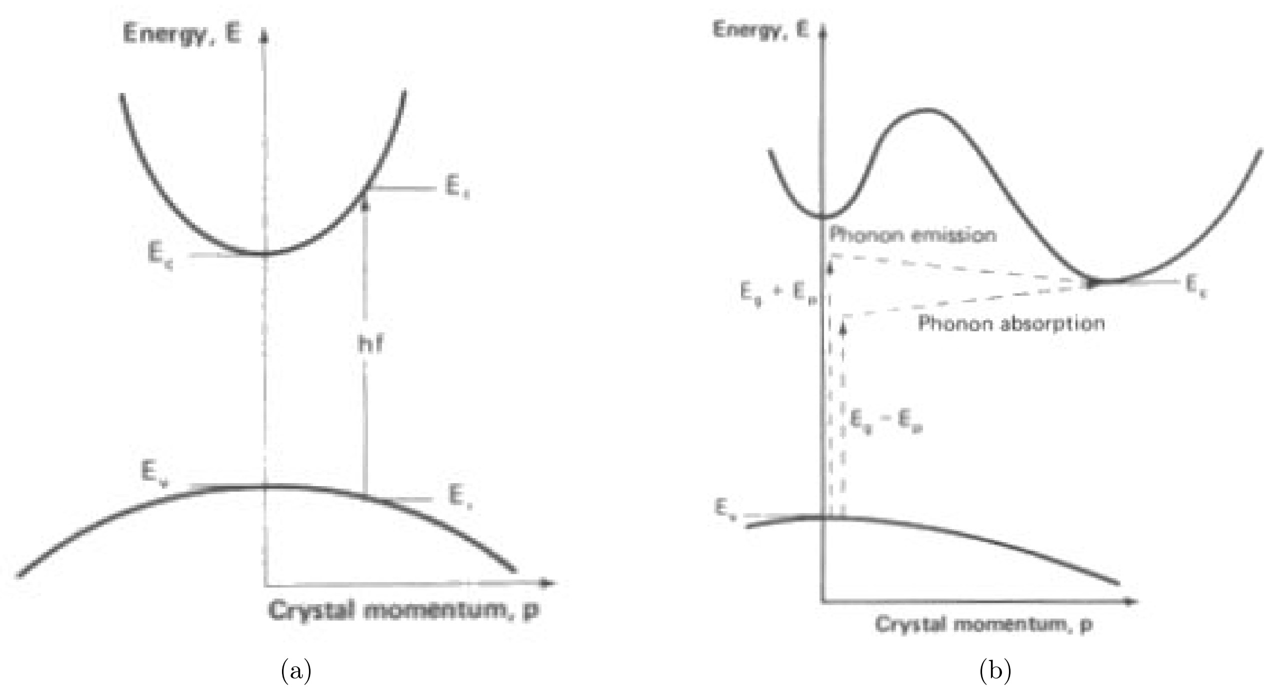

(a) (b)

Figure 16: Comparison between direct and indirect band gap structure [1].

1.6 Recombination mechanisms

Generation mechanisms have their opposite phenomena, which are the case of free carriers (electron and hole pairs) that lose their energy and they returned to their equilibrium state, where electrons are located in the valence band. Different kind of recombination mechanisms will be presented because they are loss factors to the photovoltaic technology. Under equilibrium conditions recombinations and generations are equal, therefore carrier density is constant. A recombination rate U per unit time and volume can be defined as the difference between the recombination rate R and the generation rate G:

$$U = R - G. \tag{36}$$

1.6.1 Radiative recombination

Radiative recombinations consist of an electron transition from conduction to valence band, where the particle loss energy is in form of a light radiation. The energy of this emitted photon has to be, in direct bandgap materials, at least equal to the bandgap width, in which such phenomenon is prevalent. On the contrary, in indirect bandgap semiconductors this mechanism is not very relevant because, in order to have this, it is necessary a much higher photon energy or it has to be assisted by an emission or by an absorption of a phonon. The radiative recombination rate is defined as:

$$R_{rad} = Bnp, \tag{37}$$

where B is the radiative recombination coefficient, n and p are, respectively, the electrons and holes concentration. In dark condition, where there is no incident photons, radiative generation can be obtain from the mass action law (22) and the net recombination rate result:

$$U_{rad} = B(np - n_i^2). \tag{38}$$

1.6.2 Auger recombination

In this kind of recombinations when an electron recombines with a hole it yields energy to another carrier, whose gain energy and reach an excited state. Now it can release thermal energy (that mean phonon emission) to return to its original state. Such phenomenon is particularly relevant in highly doped semiconductors, where a high carriers density is present, in one or both bands. The relative generation process is called impact ionization, in which a carrier gains energy from another carrier and generates an electron-hole pair. The net recombination rate can be expressed as:

$$U_{auger} = (C_n n + C_p p)(np - n_i^2), \tag{39}$$

where C_n and C_p are, respectively, the electrons and the holes Auger coefficients, which depend on the considered material.

1.6.3 Schokley Read Hall recombination

Defects in the crystal lattice may arise from different causes: material impurities, crystallographic defects or defects at semiconductors surface; hence they can lead to allowed energy levels in the forbidden band. With such midgap states a two steps mechanism, called traps assisted, is possible; and it is the most relevant thermal recombinations and generations. Recombination consists of an electron that, when it loss energy, relaxs itself from the conduction band to a midgap level and then in the valence band. For crys-

talline silicon, it can be assumed a single level trap, therefore the net recombination rate, according to the Shockley-Read-Hall's (SRH) model in stationary condition, is expresses as:

$$U_{SRH} = \frac{(np - n_i^2)}{\tau_n^{SRH}(p + p_1) + \tau_p^{SRH}(n + n_1)}, \tag{40}$$

where τ_n^{SRH} and τ_p^{SRH} are, respectively, the average lifetime of electrons and holes; n_1 and p_1 are defined as in the following:

$$n_1 = N_C \exp\left(\frac{E_{trap} - E_C}{kT}\right), \tag{41}$$

$$p_1 = N_V \exp\left(\frac{E_V - E_{trap}}{kT}\right), \tag{42}$$

where E_{trap} is the trap energy level, N_C and N_V are the effective density of states in the respective bands. When U_{SRH} reaches its maximum value the energy trap level is located at the middle of the band gap. The defects at a semiconductor surface are caused by the interruption of the periodicity in the crystal lattice, which causes dangling bonds at the semiconductor surface and an higher defects concentration. This can be modeled with a slightly different equation than the previous one:

$$U_{SRH}^{SURF} = \frac{S_n S_p (np - n_i^2)}{S_n(p + p_1) + S_p(n + n_1)}, \tag{43}$$

where S_n and S_p are the surface recombination velocities, expressed in cm/s.

1.6.4 Carrier lifetime

When the number of minority carriers increased above the equilibrium, by means of some kind of generation mechanisms, the excess of excited particles will decay to zero by means of the recombination phenomena described previously. The lifetime is the average time in which a carrier is in an excited state. Therefore the recombination rate could be expressed as:

$$U(n,p) \approx U(n_0, p_0) + \left(\frac{\partial U}{\partial p}\right)_0 (p - p_0) + \left(\frac{\partial U}{\partial n}\right)_0 (n - n_0) \tag{44}$$

where n_0 and p_0 are the carrier concentrations under equilibrium conditions; the first addend is zero because generations and recombinations mechanism balance themselves in equilibrium. The terms $(n - n_0)$ and $(p - p_0)$ indicate the excess of minority carriers, whereas the lifetime is the reverse of the partial derivative:

$$\tau_n = \frac{1}{(\frac{\partial U}{\partial n})_0}, \tag{45}$$

$$\tau_p = \frac{1}{(\frac{\partial U}{\partial p})_0}, \tag{46}$$

therefore the net recombination rate can be expressed as:

$$U(n,p) = \frac{(p - p_0)}{\tau_p} + \frac{(n - n_0)}{\tau_n}. \tag{47}$$

For each recombination mechanisms a specific expression of the lifetime can be obtained:

$$\tau_{RAD} = \frac{1}{Bn}, \tag{48}$$

$$\tau_{auger} = \frac{1}{C_n n^2}, \tag{49}$$

$$\tau_{SRH} = \frac{1}{\sigma_n v_{TH} N_T}, \tag{50}$$

where σ_n is the capture cross section of the recombination center, v_{TH} is the carriers thermal velocity and N_T is the traps concentration. The overall lifetime is defined as:

$$\frac{1}{\tau} = \frac{1}{\tau_{RAD}} + \frac{1}{\tau_{auger}} + \frac{1}{\tau_{SRH}}. \tag{51}$$

Another important parameter is the diffusion length, which is the average distance that a carrier can move from the generating point before recombine:

$$L = \sqrt{D\tau}, \tag{52}$$

where D is the minority carrier diffusivity, measured in m^2/s.

1.7 Basic equations of semiconductor-device physics

A set of equations to describe the electrical behaviour of a semiconductor device [1] is introduced in this section. Those equations are in one dimension (1D), whereas for a three-dimensional theory it is necessary to replace the spatial derivatives with a devergence operator, in case of vector quantities, or with a gradient operator, for each scalar quantities. A further assumption is to consider only stationary equations, which is correct in order to obtain the electrical characterization of photovoltaic devices.

1.7.1 Poisson's equation

Poisson's equation relates the electric field divergence to the space charge density; its 1D expression is:

$$\frac{d\xi}{dx} = \frac{d^2\phi}{dx^2} = \frac{\rho}{\varepsilon}, \tag{53}$$

where $d\xi/dx$ is the variation of the electric field along the x axis, ϕ is the electrostatic potential, ρ is the charge density and ε is the electrical permittivity. Contributions to the charge density come from both the free carriers (electron as negative charge and hole as positive) and doping density. An acceptor ionized impurity, that acquired an electron, has a net negative charge, similarly a ionized donor has a negative charge. Hence,

$$\rho = q(p - n + N_D - N_A), \tag{54}$$

where p and n are holes and electrons densities, N_D and N_A total density of donors and acceptors, q is the elementary electrical charge equal to $1.602 \cdot 10^{-19}[C]$.

1.7.2 Drift-Diffusion model

Free carriers, which are no more bounded to the atoms, can move in the crystal lattice structure of the semiconductor. However, this is not a direct motion, in fact, it consists of particles which collide with atoms nucleo and change their direction; therefore this scattered constant velocity motion have a random direction. The average speed of electrons depends on material temperature:

$$V = \frac{1}{2mv_{TH}}, \tag{55}$$

where m is the carriers mass and v_{TH} is the thermal velocity, which is the average carriers velocity. The average distance travelled by an electron between two collisions is called the scattered length. Without any external stimulus there is no net movement of carriers, due to their random directions.

One of the possible reason for a net movement is a concentration gradient between different regions of the device. In a low concentration area there is more space for other carriers, creating a favorite movement direction therefore a net flow charge occurs in order to obtain an uniform distribution. The rate on which diffusions occur depends on thermal velocity and scattering length. One-dimensional diffusion equations are:

$$\begin{aligned} J_n &= qD_n\frac{dn}{dx}, \\ J_p &= -qD_p\frac{dp}{dx}, \end{aligned} \tag{56}$$

where D_n and D_p are the diffusion coefficient for electrons and holes, measured in cm^2/s. Diffusion current densities J_n and J_p are proportional to the diffused particles flux.
In presence of an electric field the superimposition of random directed movement results in a net direction flow; holes are accelerated in the same direction of the electric field while electrons move in the opposite direction, because they have a negative charge. The net carrier movement it is characterized by mobility, which varies between different semiconductor materials. Drift transport always occurs when an electric field is applied; therefore it is not an exclusive phenomenon of semiconductor materials. One-dimensional drift equations are:

$$J_n = qn\mu_n\xi, \qquad J_p = qp\mu_p\xi, \tag{57}$$

where μ_n and μ_p are the electrons and the holes mobility and ξ is the electric field. The drift diffusion model considers both the conduction phenomena and it is express as:

$$J_n = qn\mu_n\xi + qD_n\tfrac{dn}{dx}, \qquad J_p = qp\mu_p\xi - qD_p\tfrac{dp}{dx}, \tag{58}$$

where diffusivity and mobility are related by means of the Einstein's relationship:

$$D_{n,p} = \left(\frac{kT}{q}\right)\mu_{n,p}. \tag{59}$$

The total current is the sum of electrons and holes current since they both participate to the conduction flow:

$$J = J_n + J_p. \tag{60}$$

1.7.3 Continuity equations

The continuity equation merely keeps trace of the particles number in the material. Considering a volume element of length δ_x and a cross section area A it can be stated that the increase net rate of electrons is the rate at which they enter minus the rate at which they exit.

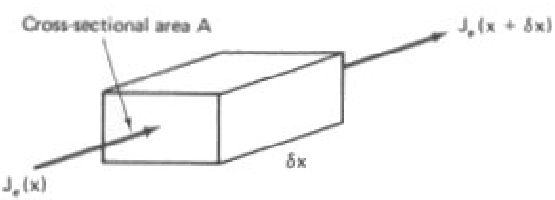

Figure 17: Elemental volume for deriving the continuity equation [1].

The number of ingoing and outgoing electrons depends on the current density. The net increase rate must be zero under stationary condition, therefore for electron and hole both result:

$$\frac{1}{q}\frac{dJ_n}{dx} = (U - G),$$
$$\frac{1}{q}\frac{dJ_p}{dx} = -(U - G), \tag{61}$$

where G is the net generating rate by external processes, like illumination, and U is the net recombination rate.

1.8 Pn junction

Typical solar cells are essentially a very large pn junction diode, which is formed by two semiconductor regions with different kinds of doping in contact. The n-type region has a high electrons concentration whereas the p-type one has a high holes concentration; therefore majority carriers will flow, respectively, to the other region. In order to stop this conduction the fixed dopant atoms are the source of an electric field, which quickly drive free carriers out leading to the creation of *depletion region* $(-x_N < x < x_P)$ and a substantial equilibrium situation. Assuming that n-region and p-region are thick enough, the regions around the depleted one, where $x \leq -x_N$ and $x \geq x_P$) Fig. 18 are called quasi-neutrals regions.

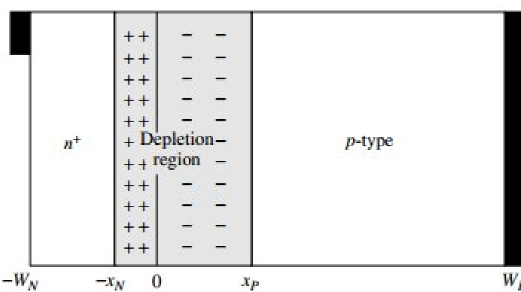

Figure 18: Structure of a pn junction with depleted and quasi-neutrals region[8].

By means of this junction a potential change occurs, which is defined as the built-in potential ψ_{bi}.

$$\psi_{bi} = \frac{kT}{q}\ln\left(\frac{N_A N_D}{n_i^2}\right). \tag{62}$$

The Poisson's equation (53) can be defined for each regions, with the assumption that in the depleted regions the dominant charges are the dopants:

$$\frac{d^2\phi}{dx^2} = \begin{cases} 0 & \text{if} \quad x \leq -x_N, \\ \frac{qN_A}{\varepsilon} & \text{if} \quad -x_N < x < 0, \\ -\frac{qN_D}{\varepsilon} & \text{if} \quad 0 < x < x_P, \\ 0 & \text{if} \quad x \geq x_P, \end{cases} \tag{63}$$

the overall system is neutral, therefore the charge in the p-region have to be equal to the charge in the n-region and result:

$$N_A x_P = N_D x_N, \tag{64}$$

hence the depleted zone thickness depends on doping concentration. By integration of the equations (63) the trend of the electric field can be obtained; as shown in Fig. 19 its maximum is reached at the metallurgic junction:

$$E_{max} = |E(x=0)| = \left|\frac{d\phi}{dx}\right|_{x=0} = \frac{qN_D x_N}{\varepsilon} = \frac{qN_A x_P}{\varepsilon}. \tag{65}$$

By further integrating over the space the trends of the electrostatic potential is:

$$\phi = \begin{cases} \psi_{bi} & \text{if} \quad x \leq -x_N, \\ \psi_{bi} - \frac{qN_D}{2\varepsilon}(x + x_N)^2 & \text{if} \quad -x_N < x < 0, \\ \frac{qN_A}{2\varepsilon}(x - x_P)^2 & \text{if} \quad 0 < x < x_P, \\ 0 & \text{if} \quad x \geq x_P. \end{cases} \tag{66}$$

In order to ensure the potential continuity at $x = 0$,

$$\psi_{bi} - \frac{qN_D}{2\varepsilon}(x + x_N)^2 = \frac{qN_A}{2\varepsilon}(x - x_P)^2. \tag{67}$$

From the equations (64) and (67) the width of the depleted region is derived:

$$W_{DEP} = x_N + x_P = \sqrt{\frac{q}{2\varepsilon}\left(\frac{N_D + N_A}{N_D N_A}\right)\psi_{bi}}, \tag{68}$$

in which, when an external voltage V_A is applied, the relationship results:

$$W_{DEP} = \sqrt{\frac{q}{2\varepsilon}\left(\frac{N_D + N_A}{N_D N_A}\right)(\psi_{bi} - V_A)}, \tag{69}$$

By means of substitution the values of x_N and x_P are deduced from equation (69) and equation (65), therefore, the maximum electric field value is:

$$E_{max} = \sqrt{\frac{2q}{\varepsilon}(\psi_{bi} - V_A)\left(\frac{1}{N_D} + \frac{1}{N_A}\right)^{-1}}. \tag{70}$$

The excess of minority carriers in quasi neutral regions (where the diffused current component only exist) are expressed as:

$$\begin{aligned} p_n &= \frac{n_i^2}{N_D}\exp\left(\frac{qV_A}{kT}\right) = p_{n0}\exp\left(\frac{qV_A}{kT}\right), \\ n_p &= \frac{n_i^2}{N_A}\exp\left(-\frac{qV_A}{kT}\right) = n_{p0}\exp\left(-\frac{qV_A}{kT}\right). \end{aligned} \tag{71}$$

1.8.1 Dark characteristic

Under low injection assumption (which asserts that the minority carrier number is much lower than that of majority ones) without considering any generation and recombination mechanism in the depleted region and no photogenerated carriers occur the current can be calculated as described in the following. In the n-type quasi neutral region the holes diffusion current is obtained from equation (56) and the continuity equation (61); therefore, by considering a net recombination rate equal to $(p_n - p_{n0})/\tau_p$ with no generation, results:

$$D_p \frac{d^2 p_n}{dx^2} = \frac{p_n - p_{n0}}{\tau_p}. \tag{72}$$

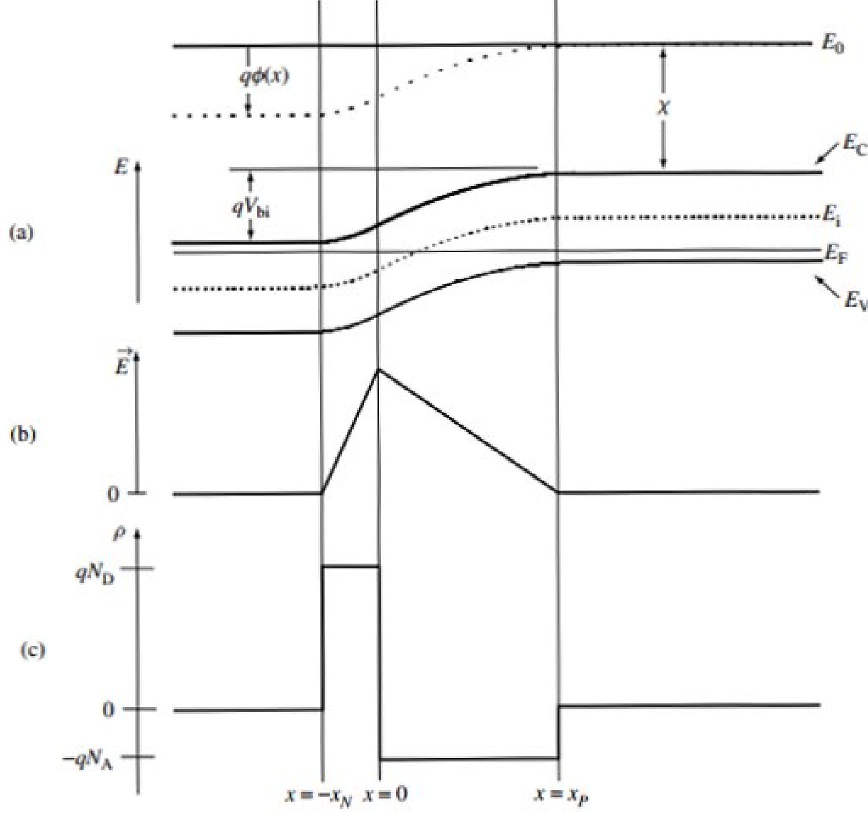

Figure 19: Solar cell equilibrium conditions: (a) energy bands, (b) electric field and (c) charge density [8].

This differential equation can be solved as:

$$p_n(x) = p_{n0} + p_{n0}\left(e^{\frac{qV}{kT}} - 1\right)e^{-\frac{x}{L_p}}, \tag{73}$$

where L_p is the diffusion length for holes. From (56) and the previous expression, the hole current can be derived as:

$$J_p(x) = \frac{qD_p p_{n0}}{L_p}\left(e^{\frac{qV}{kT}} - 1\right)e^{-\frac{x}{L_p}}. \tag{74}$$

Current is constant in the depleted zone, therefore, the hole density current, from the n-region, and the electron density current, from the p-type region, can be added:

$$J_{TOT} = J_p(x)|_{x=0} + J_n(x)|_{x=0} = \left(\frac{qD_n n_{p0}}{L_n} + \frac{qD_p p_{n0}}{L_p}\right)\left(e^{\frac{qV}{kT}} - 1\right), \tag{75}$$

and, as consequence, the expression of the current is:

$$I = I_0\left(e^{\frac{qV}{kT}} - 1\right), \tag{76}$$

where I_0 is the saturation current.

1.8.2 Illuminated characteristic

A constant optical generation in the photovoltaic device is assumed, the equation (72) becomes:

$$\frac{d^2 p_n}{dx^2} = \frac{p_n - p_{n0}}{L_p^2} - \frac{G}{D_p}, \tag{77}$$

which differential equation's solution is:

$$J_p(x) = \frac{qD_p p_{n0}}{L_p}\left(e^{\frac{qV}{kT}} - 1\right)e^{-\frac{x}{L_p}} - qGL_p e^{-\frac{x}{L_p}}. \tag{78}$$

The generated current in the depleted region has to be considered as well:

$$J_n^{depl} = \left|J_p^{depl}\right| = q\int_{-W_{DEP}}^{0} -G dx = qGW_{DEP}, \tag{79}$$

and the resulting total current is:

$$I = I_0\left(e^{\frac{qV}{kT}} - 1\right) - I_L, \tag{80}$$

in which the photogenerated current is the sum of all the current, generated in the three different regions:

$$I_L = qAG(W_{DEP} + L_p + L_n), \tag{81}$$

where A is the device surface area.

2 Solar cells

The first solar cell was invented in 1883 by Charles Fritts, it was based on selenium and it had a conversion efficiency of 1%. In 1954 Bell laboratories produced the first silicon solar cell based on a pn junction, which had an efficiency of 6%; whereas the first commercial devices was developed by Sharp in 1963.

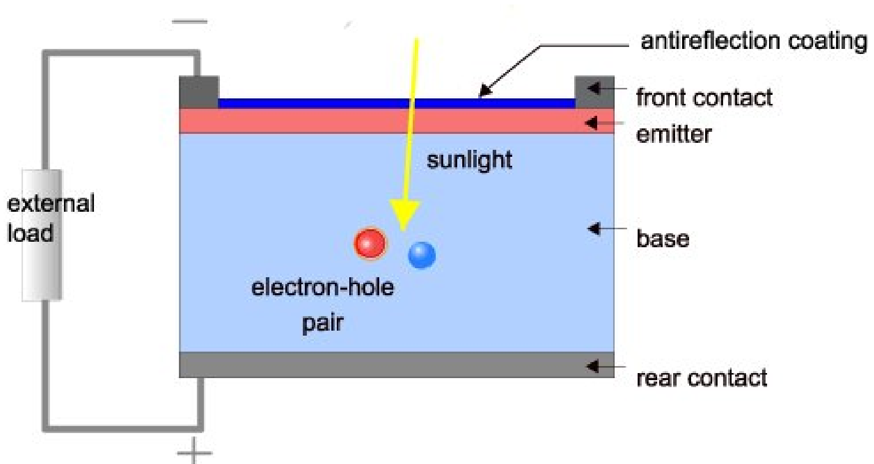

Figure 20: Architecture of a typical solar cell [3].

Standard solar cells are large pn junctions, with a highly doped n region and a p doped region called emitter and base, respectively. Front and back metal contacts are both necessary to collect the photogenerated carriers. Photocurrent generation in solar cell can be considered a two-steps process: i) photons are absorbed in order to generate electron-hole pairs and ii) carriers are separated by the electric field due to the pn junction.

2.1 I-V characteristic

Fig. 21 shows a typical solar cell IV curve, where the three main output parameters are in evidence. *Short-circuit current* I_{sc} can be defined from equation (80) by setting a zero voltage; under ideal conditions it is approximately equal to the photogenerated current I_L defined in equation (81). I_{sc} is the results of two different contributions: the short circuit currents due to depleted and the ones due to the quasi neutrals regions; whose are expressed in detail in [8]. The *open-circuit voltage* V_{oc} value can be obtained from equation (80):

$$V_{oc} = \frac{kT}{q} \ln \left(\frac{I_L}{I_0} + 1 \right). \tag{82}$$

In Fig. 21 the maximum power point (MPP) (V_{mp},I_{mp}) is highlighted; which is the operating point that lead to the maximum possible output power. The ratio between

the maximum output power and the product $V_{oc}\ I_{sc}$ is called *fill factor*:

$$FF(\%) = \frac{V_{mp}I_{mp}}{V_{oc}I_{sc}} \cdot 100. \tag{83}$$

Ideally $FF = 100\%$, practical solar cells exhibits value of FF within the 70%-80%. An empirical expression [2] for the fill factor could be defined as:

$$FF = \frac{V_{oc} - \frac{kT}{q}\ln\left[qV_{oc}/kT + 0.72\right]}{V_{oc} + \frac{kT}{q}}, \tag{84}$$

which depends only on open circuit voltage and cell temperature. The energy conversion efficiency is the ratio between output and input power:

$$\eta = \frac{V_{mp}I_{mp}}{P_{in}} = \frac{V_{oc}I_{sc}FF}{P_{in}}, \tag{85}$$

in order to reach a good efficiency V_{oc}, J_{sc} and FF have to be maximized.

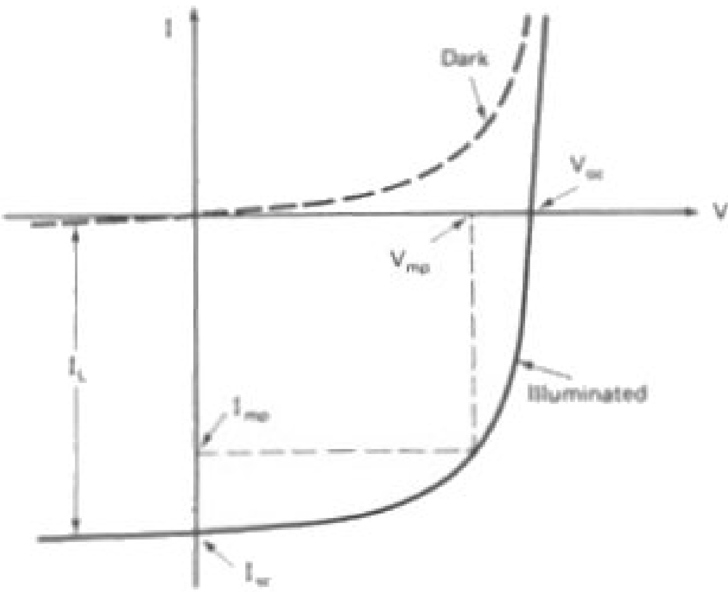

Figure 21: I-V characteristic under dark and illuminated conditions [1].

2.1.1 Saturation current

The saturation current I_0 is an important parameter obtained by the equation (75). The total current is:

$$I = I_{sc} - I_{01}(e^{\frac{qV}{kT}} - 1) - I_{02}(e^{\frac{qV}{2kT}} - 1). \tag{86}$$

I_{01} is the dark saturation current due to the quasi-neutral regions and it has both an electron and a hole component:

$$I_{01} = I_{01,n} + I_{01,p}, \tag{87}$$

where $I_{01,n}$, under the assumption of finite dimension junction, in given by [1] as:

$$I_{01,n} = qA\frac{n_i^2}{N_A}\frac{D_n}{L_n}\left\{\frac{\frac{D_n}{L_n}\sinh\left[(W_p - x_p)/L_n\right] + S\cosh\left[(W_p - x_p)/L_n\right]}{\frac{D_n}{L_n}\cosh\left[(W_p - x_p)/L_n\right] + S\sinh\left[(W_p - x_p)/L_n\right]}\right\}. \tag{88}$$

W_n and W_p are the length of the quasi neutral regions, D_n and D_p are the diffusivity of electrons and holes, L_n and L_p are the diffusion length and A is the surface area. Such current depends also on the surface recombination velocity S, which has to be considered for a finite dimension devices. A similar expression exists for $I_{01,p}$.
I_{02} is the dark saturation current due to the recombinations in the depleted region:

$$I_{02} = qA\frac{n_i W_{DEP}}{\tau_{DEP}}, \tag{89}$$

where τ_{DEP} is the carriers lifetime and W_{DEP} is the width of the depleted region. Its dimension is defined as in equation (69) and it depends on the applied voltage, therefore I_{02} is bias-dependent. The circuital model (two diode model) corresponding to equation (86) is shown in Fig. 22.

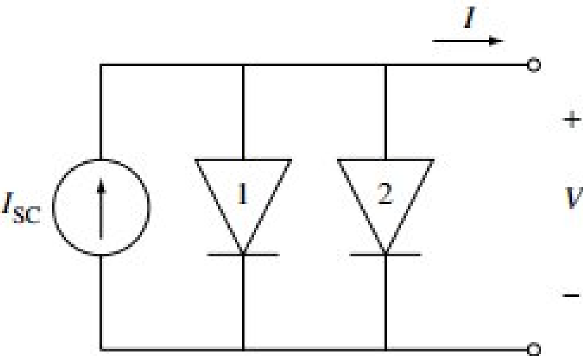

Figure 22: Two diode solar cell model [8].

2.2 Other figures of merit

2.2.1 Trasmittance, reflectance and absorbance

Reflectance and trasmittance can be defined as in section (1.5.1):

$$R(\lambda) = \frac{P_{reflected}}{P_{incident}},$$
$$T(\lambda) = \frac{P_{transmitted}}{P_{incident}}, \tag{90}$$

where $P_{reflected}$ is the light power reflected by the solar cell surface and $P_{transmitted}$ is the power passing through the device, without being absorbed, and transmitted from the back. The absorbance index $A(\lambda)$ could be defined in order to satisfy the optical conservation law:

$$A(\lambda) + R(\lambda) + T(\lambda) = 1. \tag{91}$$

2.2.2 Quantum efficiency

The external quantum efficiency EQE is defined as the ratio of the number of carriers, collected by the solar cell in short circuit conditions, to the number of photons for a given incident energy:

$$EQE(\lambda) = \frac{J_{sc}(\lambda)}{J_{IN}(\lambda)}, \tag{92}$$

where J_{IN} is the density current in case that every incident photon gives rise to an electron-hole pair:

$$J_{IN}(\lambda) = q\phi(\lambda) = q\frac{I_0(\lambda)}{E_{ph}(\lambda)}, \tag{93}$$

where ϕ is the incident power flux, I_0 is the input irradiance and E_{ph} is the photons energy. The internal quantum efficiency is the ratio of the number of charge carriers collected by electrodes to the number of incidents photons, with a given energy, which are absorbed. It can be measured from the EQE deprived of the reflected component:

$$IQE(\lambda) = \frac{EQE(\lambda)}{1 - R(\lambda)}. \tag{94}$$

IQE is higher than EQE, low IQE values indicate high recombinations in the semiconductor material. In Fig. 23 is presented an example of a typical quantum efficiency characteristic; it is worth noticing that it is lower for both high and low photon energy, which is due, respectively, to strong recombinations at the front surface and to rear surface recombination and low absorption of the greater wavelengths.
The collection efficiency η_C describes the probability that photogenerate carriers are collected and, hence, contribute to the photocurrent. The spectral response $SR(\lambda)$ is

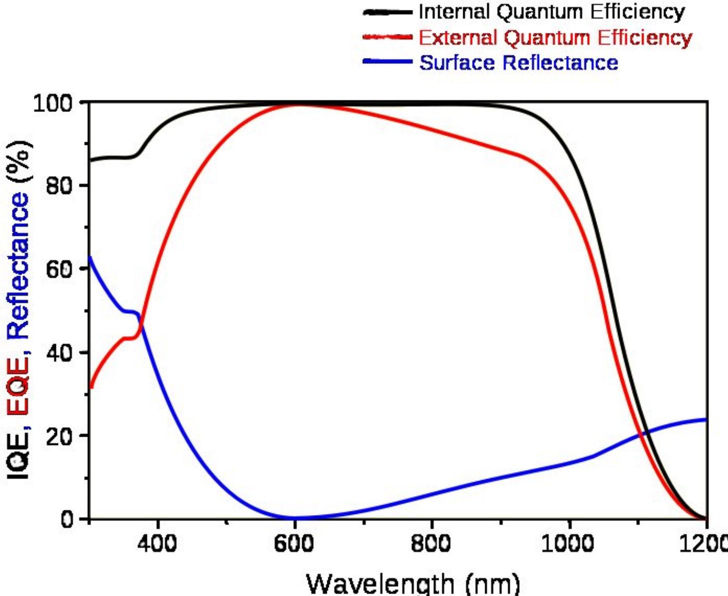

Figure 23: Typical reflectance, external and internal quantum efficiency characteristic (from wikipedia).

the ratio of the generated current to the incident power:

$$SR(\lambda) = \frac{qQE(\lambda)}{E_{ph}(\lambda)}, \tag{95}$$

where QE could be either internal or external quantum efficiency.

2.3 Efficiency limits

Equation (85) shows that conversion efficiency depends on all the three main parameters discussed in section (2.1). It also shows that the fill factor could be expressed as a function of V_{oc}; therefore in order to predict the maximum efficiency, only V_{oc} and J_{sc} trends have been considered. The upper limit for J_{sc} is obtained considering an ideal situation where all incident photons on the cell, with greater energy than the bandgap width E_g, lead to an electron-hole pair creation that flows in the external circuit. Hence, the photon flux $\phi(\lambda)$ has to be integrated over its wavelength range; therefore the maximum J_{sc} is obtained as a function of E_g as shown in Fig. 24 for $AM0$ and $AM1.5$ spectrums. Density current improves as the bandgap is reduced but, on the other hand, with smaller E_g the thermal energy wasted by excited electrons improves.

The upper limit for V_{oc} is a little more complicated to obtain; its value is given from equation (82), where its dependency on the inverse of the saturation current is explicited. Also low recombination rates, which means long diffusion lengths, are necessary to improve V_{oc}. The expression of I_0 in the subsection (2.1.1) can be simplified under the approximation of short base diode (where the minority carriers diffusion length is greater

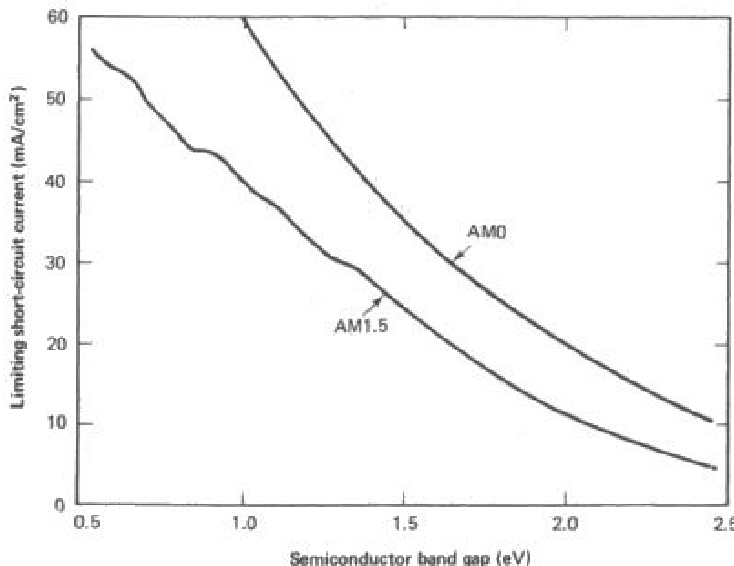

Figure 24: Short circuit density current trend compared to the bandgap [3].

than the length of the device):

$$I_0 = A\left(\frac{qD_n n_i^2}{L_n N_A} + \frac{qD_p n_i^2}{L_p N_D}\right), \tag{96}$$

I_0, which has to be as small as possible, depends on the quality of the semiconductor material. The intrinsic concentration n_i value can be obtained from equation (21):

$$n_i^2 = N_V N_C \exp\left(-\frac{E_g}{kT}\right), \tag{97}$$

where N_V and N_C are the effective density of states in the respective bands. By replacing n_i^2 by the expression given by (96) the dependence of the saturation current on the bandgap width can be expressed; a widely accepted lower bound value of I_0 is proposed by M.A. Green in [1]:

$$I_0 = 1.5 \cdot 10^5 \exp\left(-\frac{E_g}{kT}\right)\left[A/cm^2\right]. \tag{98}$$

Therefore the value of V_{oc} increases linearly with the bandgap following an opposite trend with respect to J_{sc}. The optimum bandgap width to maximize the efficiency is shown in Fig. 25, where also different semiconductors bandgap values are in evidence. GaAs is the closest material to the peak of the maximum efficiency (with E_g in a range from 1.4 eV to 1.6 eV) close to 25%.

Since photons with energy smaller than E_g are not absorbed, the efficiency is affected by an efficiency reduction of 55% relatively. Other effects that reduce potential efficiency are related to the phenomena discuss in the previous section, as recombination, reflection,

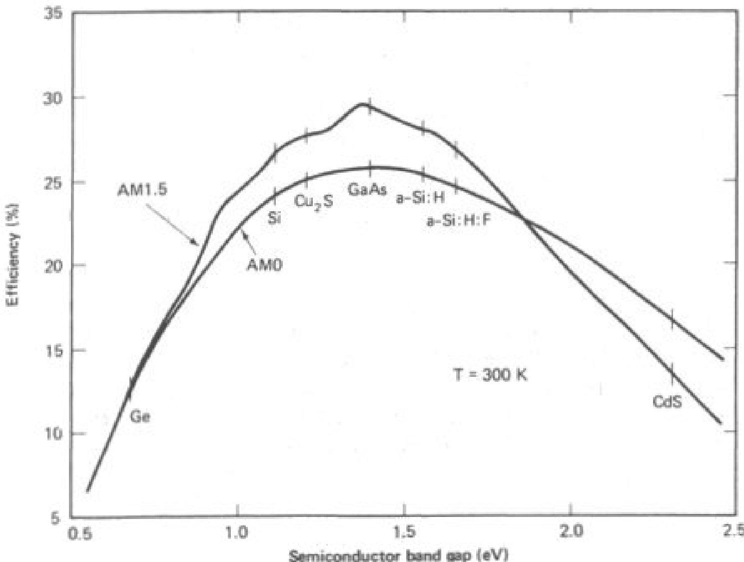

Figure 25: Solar cell efficiency limit as function of the semiconductor bandgap [1].

transmission. While other losses are due to parasitic resistance effects, which all will be better explained in section (2.5).

2.4 Effect of temperature

Operating temperature may vary significantly in a solar cells, therefore the effect of its variations on performance has to be investigated. Short circuit current has a slight sensitivity to temperature (T) however, it slightly improves due to the decreasing bandgap width when temperature raises. The dependency on E_g is well modeled in [8] with the formula:

$$E_g(T) = E_g(0) - \frac{\alpha T^2}{T + \beta}, \tag{99}$$

where α and β are specific constants for a certain semiconductor. Dependence of V_{oc} on temperature can be expressed by means of a simplified expression of the equation (86), under an open circuit conditions is:

$$I_{sc} \approx I_{01} e^{qV_{oc}/kT} \approx BT^{\zeta} e^{-E_g(0)/kT} e^{qV_{oc}/kT}, \tag{100}$$

where B is a constant and the term $T^{\zeta} e^{-E_g(0)/kT}$ took into account for the temperature dependency of the saturation current. By differentiating with respect to T and by assuming $dI_{sc}/dT = 0$, the temperature dependency of the open-circuit voltage can be expressed as:

$$\frac{V_{oc}}{dT} = \frac{\frac{1}{q} E_g(0) - V_{oc} + \zeta \frac{kT}{q}}{T}. \tag{101}$$

Such equation predicts an approximately linear dependence on temperature; for instance, for silicon $-2.3\ mV/°C$ variation is calculated.

2.5 Efficiency losses

The sketch of a real conventional solar cell is shown in Fig. 26. The efficiency is significantly lower than the theoretical upper bound limit discussed before, because of the loss mechanisms outlined in this subsection.

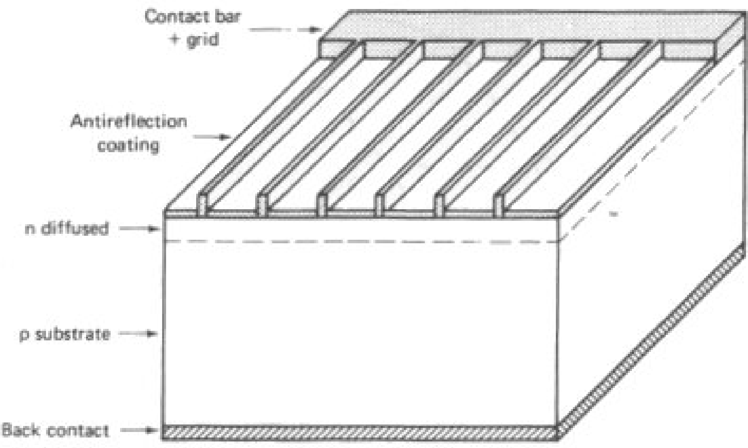

Figure 26: Standard solar cell schematic [1].

2.5.1 Short-circuit current losses

I_{sc} is affected by two types of losses: optical and electrical losses. Bare silicon is quite reflective and almost 10% of the incident light is reflected. Reflection can be highly reduced by the introduction of different materials as anti reflection coating (ARC). Another loss mechanism is the shadowing effect; which is due to the reduction of the light exposed area caused by the metal contacts front grid. The last one of the considered optical losses is caused by the not absorbed photons; the cell thickness has to be compared to the absorption length, which was defined in section (1.5.2). Furthermore, if the cell is not thick enough with reference to the absorption length of the light for the considered material,

some photons are transmitted and do not contribute to the photocurrent. It is worth noticing that thicker device is necessary for indirect bandgap semiconductors to obtain the same value of photocurrent of a direct bandgap material. Also recombinations both bulk and surface are loss mechanisms, therefore higher recombinations is fewer is the probability to be collected at the metal contacts (see collection probability in section (2.2.2)).

2.5.2 Open-circuit voltage losses

Recombinations of bulk and at surfaces level are loss factors for either J_{sc} and V_{oc}. One of the most effective phenomenon is the recombination through traps into the depleted region; it can be noticed, from equation (40), that this effect has a peak value when traps have a midgap energy value. In order to consider it an additional term n, which is called ideality factor, has to be included in the dark current saturation expression (76):

$$I = I_0(e^{qV/nkT} - 1), \tag{102}$$

n is 1 under ideal conditions.

2.5.3 Fill Factor losses

A reduced open circuit voltage also affects the fill factor and, by defining a normalized voltage $v_{oc} = V_{oc}/(nkT/q)$, its expression is:

$$FF = \frac{v_{oc} - \ln(v_{oc} + 0.72)}{v_{oc} + 1}. \tag{103}$$

In practical solar cells parasitic resistances play a crucial role and they are correlated to several physical phenomena; both series and shunt resistance are included in the two diode model in Fig. 27 and they both lead to reduced fill factor. Major contributions to the series resistance (R_S) are the bulk semiconductor resistance, the resistance of both contacts, interconnections and the contact resistance between metal and semiconductor. The shunt resistance R_{SH} is caused by leakage due to crystal defects and to the edge of pn junctions.

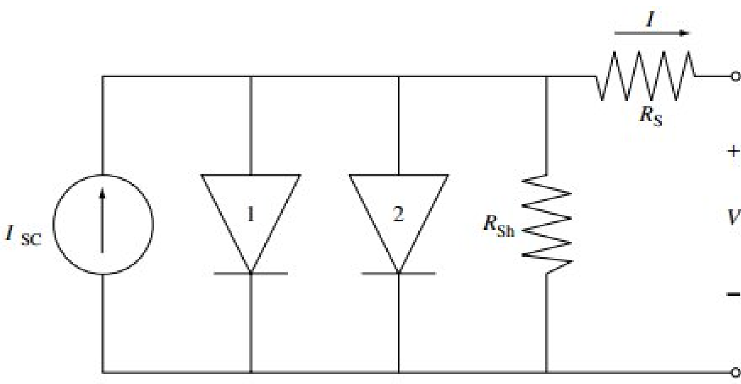

Figure 27: Two diode model including the parasitic resistances [8].

High value of R_S also affects the short circuit current and a very low R_{SH} degrades the open circuit voltage, as shown in Fig. 28. In order to highlight the impact of different parasitic resistance values in the fill factor it is convenient to define a *characteristic*

resistance as:

$$R_{CH} = \frac{V_{oc}}{I_{sc}}. \tag{104}$$

When R_{CH} is larger than R_S and smaller than R_{SH} the parasitic resistances are not very effective to FF. With the definition of the normalized resistances $r_S = R_S/R_{CH}$ and $r_{SH} = R_{SH}/R_{CH}$ two expressions could be derived:

$$\begin{aligned} FF &= FF_0(1 - r_S), \\ FF &= FF_0\left\{1 - \frac{(v_{oc} + 0.7)}{v_{oc}}\frac{FF_0}{r_{SH}}\right\}, \end{aligned} \tag{105}$$

where FF_0 is the ideal fill factor without any parasitic resistance, expressed like in equation (84).

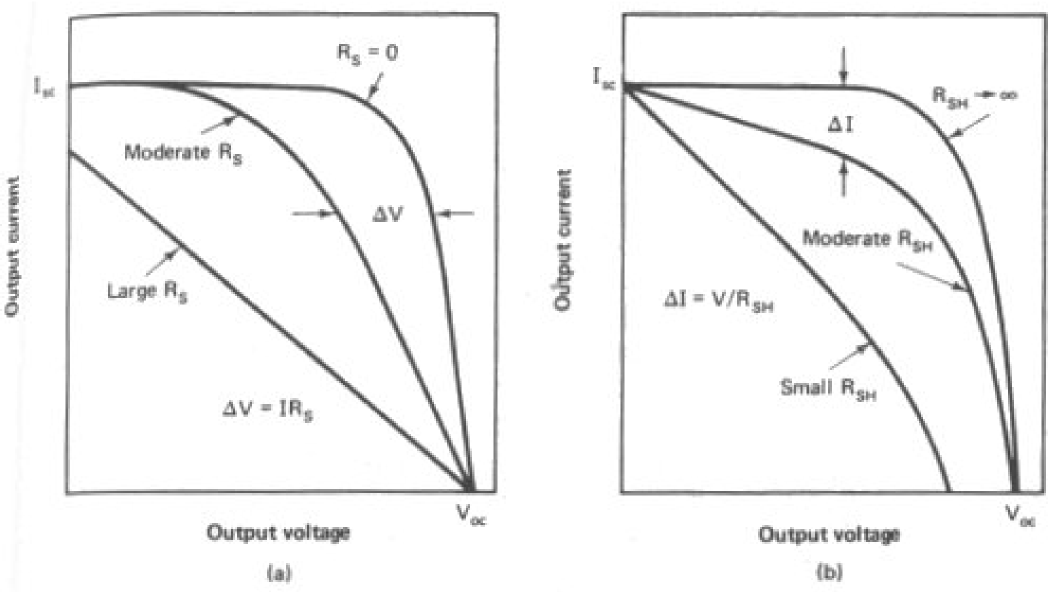

Figure 28: Variations of the output characteristic with different value of (a) R_S (b) R_{SH} [1].

2.6 Design of solar cells

Solar cells design consists of the definition of several geometrical, physical and electrical parameters towards the efficiency enhancement. The theoretical upper bound limit of η, under one sun illumination, is about 29% for a silicon cell; Such limit is calculated under the assumption of unitary quantum yield, according which every photon with an energy equal to the bandgap is absorbed. In the design of commercial solar cells, a trade off between maximum achievable efficiency and solar cell cost has to be considered. Some technological innovations are presented in the following in order to reduce the efficiency losses outlined in the previous subsection. The influence of optical losses is mainly

observed on J_{sc}. Different ways to reduce those losses have been proposed: minimizing the front contact shadowing, reducing reflection by using anti reflective coating (ARC) and increasing light absorption by means of light trapping techniques. The solar cell front shadowing is due to the front metal grid, which is necessary to the photogenerated carriers collection. An advanced contact scheme aimed at minimizing the shadowing effects while the contacts parasitic series resistance is kept low. More effective solutions are necessary also to reduce the effect of recombination at contacts.

2.6.1 Anti-reflection coating

Antireflection coating ARC consists of one or more thin layers of dielectric material with a thickness chose in order to minimize the amount of reflected rays. Interference effects due to such layers cause a phase shift between the wave reflected from the anti-reflection coating top surface and the wave reflected from the semiconductor surfaces. A zero net reflected energy is possible if the two waves destructively interfere with one another. The calculation of the optimum refractive index of the ARC is discussed in [1]. For a single layer ARC, the thickness is chosen as:

$$d_1 = \frac{\lambda_0}{4n_1}, \tag{106}$$

where n_1 is the refraction index of the ARC which is given by:

$$n_1 = \sqrt{n_0 n_2}, \tag{107}$$

where n_0 and n_2 are the indices of the external medium and of the semiconductor. Such optimization technique is valid only for one incident wavelength but not over all the spectrum; typically the ARC is optimized for a 600 nm wavelength.

2.6.2 Light trapping

The advantage due to a thinner substrate is remarkable; the bulk recombination is reduced and the cell is cheaper, because the solar cell cost is proportional to the amount of used material. On the other hand the absorption probability decrease. Light trapping techniques are aimed at maximizing the optical path, within the absorbing media. The easiest form of light trapping is a back reflector, such as the back aluminum plate, which can double the optical path. More advanced light trapping schemes are obtained by modifying the incidence angle of light by means of a textured front surface. Texturing contributes to the reduction of external front reflectivity and increases the internal reflectivity due to multiple bounces of light, which lead to an enhancement of the photon absorption probability. Two light trapping scheme are possible: Lambertian and

geometrical light trapping. A Lambertian reflector randomizes the direction of the incident light leading to an increased path length, approximately $4n^2$ times (where n is the refractive index) with reference to a single pass scheme. Such bound is known as the Yablonovitch limit which represents the maximum achievable absorbance enhancement for a light trapping scheme in the geometric optics regime. However, this limit is not valid for thin layer materials whose dimensions are comparable to the incident ray wavelength. Geometrical light trapping purpose is that to deviate the incident ray angle by means of a regular geometric patterns on the surface. Patterns are specifically designed for normal incident light and do not suffer from the previous limit. The easiest scheme was proposed by Redfield [9] and it consists of an oblique back surface that, for normal incident radiation, leading to four passages of light into the absorber layer; however, it may vary depending upon the incident angle. More effective schemes have been proposed, such as grooves (symmetric or asymmetric) and upright or inverted pyramids. Due to technological limitation, 3D pyramids are not regular, therefore their dimensions and positions are randomly distributed Fig. 29.

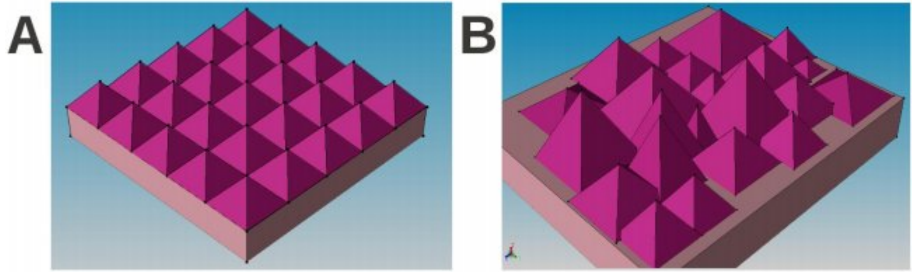

Figure 29: Periodic (A) and random (B) pyramids three-dimensional scheme [4].

2.6.3 Recombinations and parasitic resistances reduction

Recombinations are loss mechanism for both V_{oc} and J_{sc}. Effective recombination centers are the semiconductor interfaces (as the grain boundaries in multicrystalline devices) where high density of dangling bonds are typically present. High recombination rates of carriers in front surface are particularly detrimental in J_{sc}. A reduction of the dangling bonds density can be achieved by passivating the front layer by means of a dielectric material. In commercial devices this is usually obtained by a thermally grown silicon dioxide layer which has low defects state density at the interface. Ohmic metal contacts cannot be passivated with an insulator, hence it is necessary a heavily doped diffusion which degrades the carrier diffusion length. Junction of different concentrations doping, p/p^{++} in the rear and n/n^{++} in the front junction, forms an electric field which increase the potential barrier for the minority carriers, therefore they cannot flow to the metal-semiconductor interfaces. The front surface field (FSF) and the back surface field

(BSF) have the same effect as of passivation layer; all these technological options are summarized in Fig. 30.

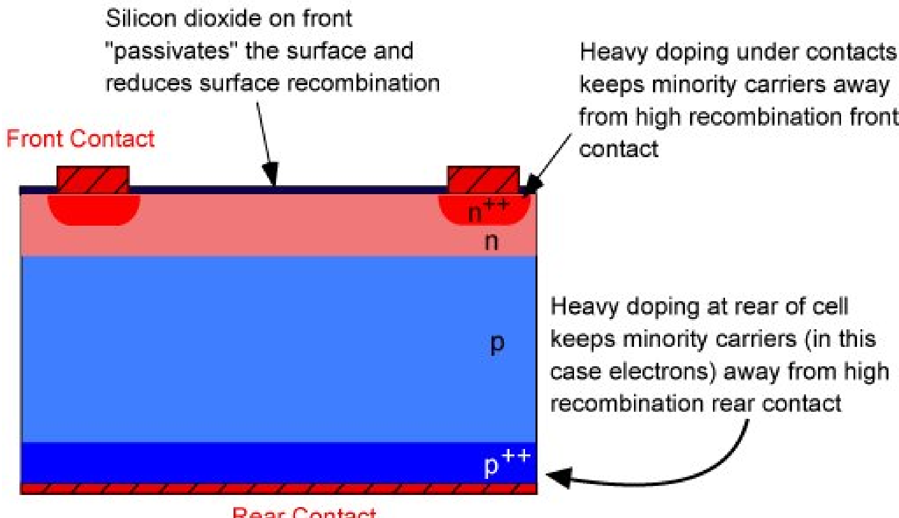

Figure 30: Summary of the technological options for surface recombination reduction [3].

2.7 Advanced silicon solar cells

Different photovoltaic technologies have been classified as generation: the first one consists of the crystalline silicon solar cells, exploiting one or another of the innovations previously described in this section. It is worth noticing that silicon can be single crystal or multicrystalline. The second one has simpler and cheaper production techniques than those of monocrystalline wafer based solar cells. However, the material quality of second generation is lower because crystal lattice is not overall regular but only a short-range order within regions of the semiconductor called grains is ensured. The boundaries between grains are recombination centers, therefore in order to avoid excessive recombination rates, a minimal grain size in the millimeters range is required. Since the introduction of second generation devices, new semiconductor materials have been investigated, such as amorphous silicon, polycrystalline silicon, cadmium telluride and many others. In addiction thin film, selective emitter, local point and others solar cell structures have been introduce. The third generation consists of technologies as nanocrystal and polymer materials solar cells, which are promising but currently are not very reliable. In this subsection, interdigitated back contact and hetero-junction solar cells are briefly described.

2.7.1 Interdigitated back contact

The main feature of the cell in Fig. 31 is that metal contacts lay only in the back cell, where n and p contacts are interdigitated and isolated. The main advantage is the total absence of shadowing effect that leads to an increased J_{sc}. To avoid high recombinations in the front and back surface a diffusion of a high concentration doping occurs, providing a front and a back surface field. Light trapping techniques and ARC layer are also implemented in the cell. The goal of many articles in literature was the optimization of physical and geometrical parameters to obtain the maximum possible efficiency. F.J. Castano and co-authors [11] by means of low cost fabrication process, like screen printing, reported an efficiency 19.1%, a J_{sc} of 41.5 mA/cm^2, V_{oc} equal to 641 mV and FF is almost 72%. Aleman and co-authors [12] used more expensive and complex technique to reports a 23.3% efficiency, a 41.6 mA/cm^2 J_{sc}, a 641 mV V_{oc} and a FF of 80.4%.

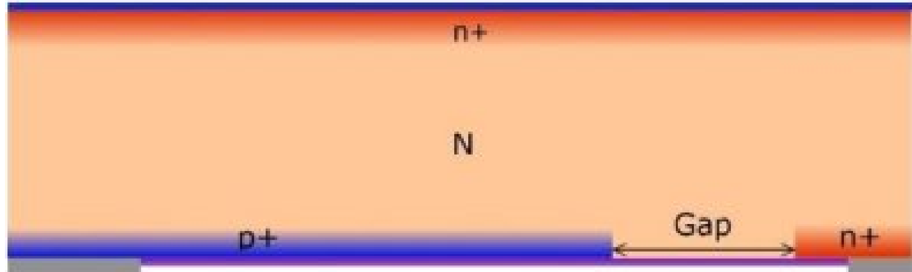

Figure 31: Cross section of a homojunction IBC solar cell [10].

2.7.2 Heterojunction with intrinsic thin layer

Heterojunction with intrinsic thin layer HIT solar cell is shown in Fig. 32. An intrinsic amorphous silicon (a-Si) layer and a p-doped a-Si layer are deposited on a randomly textured n-type crystalline silicon substrate, therefore, a p/n heterojunction is formed. On the rear side of the c-Si wafer, i-type and n-type a-Si layers are deposited. Metal grids and transparent conductive oxide are formed in both side of the device. The main advantage of these kind of cells is the high open circuit voltage V_{oc} due to a very good passivation of the c-Si dangling bonds at its surfaces. Which is obtained by means of intrinsic amorphous silicon layers, produced with low temperature process, therefore cheaper than doping diffusion in crystalline solar cells. The fabrication cost is high and a thinner cSi layer is certainly attractive but it will cause a decreased J_{sc}. In literature a trade off between saving material and absorbed current loss is researched. Fujishima and co-authors report an efficiency of 22.8%, with a very high V_{oc} equal to 743 mV, J_{sc} and FF are respectively 38.9 mA/cm^2 and 79.1% at the research and development stage.

Ballif and co-authors [14] report several research groups and industry efficiency above 20%.

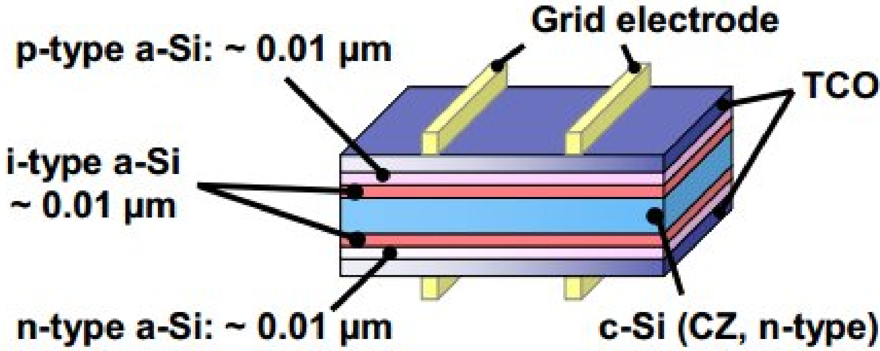

Figure 32: Schematic of a heterojunction with intrinsic layer solar cell [13].

3 Interdigitated back contact hetero-junction solar cells

The considered advanced solar cells architecture is the interdigitated back contact hetero-junction IBC-HJ. In this section its main characteristics are described as well as the main literature results on their modeling. Two main articles are taken as reference in this thesis: i) the Allen and co-authors' [15] and ii) the Lu and co-authors' [16]. IBC-HJ has the potential for high efficiency because it combines the advantages of both the architectures described previously in section (2.7): high short circuit current density J_{sc} due to a back metal grid and a high open circuit voltage V_{oc} due to surface passivation and heterojunction contacts. Even the parasitic series resistances are minimal because back contacts avoid limitations due to the trade off between parasitic resistances and optical losses. Literature simulations results are discussed in this chapter. The reference cell is shown in Fig. 33, which is the cell structure studied by [15]. It is formed by a high quality n-doped floating zone (FZ) crystalline silicon c-Si substrate featuring an intrinsic amorphous silicon a-Si thin layer at its top and its back interfaces. Such layers are necessary to passivate the surface dangling bonds and to lower the emitter saturation current, towards an increase of both V_{oc} and J_{sc}. At the front side a double layer ARC contributes to the reduction of the reflection losses. The ARC is formed by a layer of amorphous silicon nitride (a-SiNx) and by one of amorphous silicon carbide (a-SiC), both hydrogenated. At the rear side there is an interdigitated pattern of n and p contacts, made by doped amorphous silicon (a-Si) layers. The geometrical gaps between contacts are filled with a-SiNx to ensures electrical isolation.

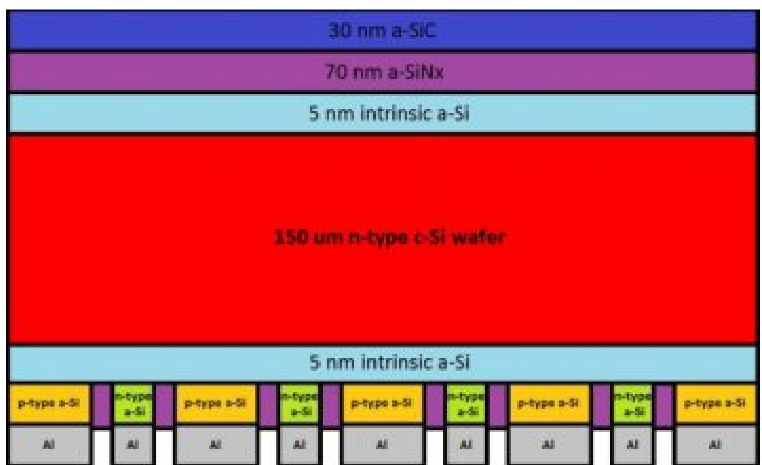

Figure 33: Cross section of an interdigitated back contact hetero-junction solar cell [15].

Performance of IBC-HJ depend on the band structure alignment at the interface, therefore, if the intrinsic a-Si layer properties are not properly chosen, device will exhibits low FF due to JV characteristic featuring s-shape, as described later in the subsection (3.3).

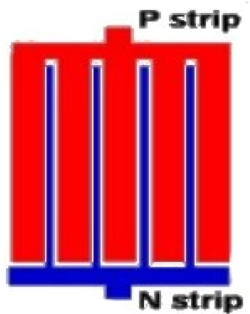

Figure 34: Bottom view of an IBC-HJ solar cell [17].

3.1 Amorphous silicon

Amorphous silicon a-Si is the non-crystalline form of silicon, in which the chemical bonds are similar to that of crystalline silicon but with small variations of the bond angles and short regularity of the lattice it is not guaranteed. Such disordered material nature leads to an anomalous electrical behaviour and to high recombination rates caused by the dangling bonds. In order to improve material quality, in electronic devices, a-Si is usually passivated by an hydrogen diffusion, which reduces the defects density by several orders of magnitude. Hydrogenated amorphous silicon (a-Si:H) exhibits lower performance than c-Si but it features several advantages: i) reduced production cost of the device, ii) thin film layers can be deposited over larger areas with referred to c-Si and by using lower temperature and relatively cheaper process. Band gap increases from 1.1 eV of crystalline silicon to about 1.7 eV in amorphous silicon, furthermore the absorption coefficient is much higher making this materials suitable for thin film solar cells. Nevertheless, the presence of a large number of dangling bonds causes a high defect density and a low diffusion lengths. The use of a-Si:H in photovoltaic technology is also limited by the light induced material degradation, called the Staebler-Wronski effect [18], which consists on a reduction of both dark conductivity and photoconductivity when amorphous silicon is subject to a prolonged illumination by means of an intense light. A complete comparison between c-Si and a-Si photovoltaic technology is presented in [19]. Doping process in a-Si is similar to that for c-Si but in this case, because the lattice is not regular, it is rather inefficient because most dopant atoms do not contribute to free carriers or they can recombine with unpassivated dangling bonds. The typical bandgap width of a-Si is 1.72 eV, however the bandgap can be changed by modifying the manufacturing process conditions. Zhang and co-authors [22] investigated three possible ways to change E_g: i) by changing the power of the R_f plasma, ii) by changing the deposition temperature or iii) by changing the H_2/SiH_4 ratio. To lower the band gap of the i-layer, the deposition temperature can be increased, the H_2/SiH_4 ratio can be increased or the power of the plasma can be reduced.

3.1.1 Density of states

In Fantoni and co-authors [20] a model suitable for density of states (DOS) in a-Si is described, it consists of a distribution of allowed energy states per unit of volume per unit energy. Singularities in the density of states distribution at the borders of the bands are replaced by more gradually decreasing exponential distributions which penetrate into the energy gaps. Such distributions are called *band tails* and their extension represents the disorder degree of the atomic structure. Higher disorder leads to more allowed states in the bandgap, which are localized and behave like traps. Tail states are responsible for shallow trapping, hence the trapped carriers do not contribute to any transport phenomena, except those through tunneling from an occupied to an unoccupied state at equivalent energies. Besides such states are also localized within the midgap allowed states exist, which are due to dangling bonds in the material and exhibits a Gaussian distribution. Trap centers can be divided into two species: i) donor-like states, in which a trap is charged by electrons and are neutral for holes, and ii) acceptor-like states, where a trap is charged by holes and is neutral for electrons.
The energy dependent DOS model consists on the superimposition of two exponential distributions of tail states $g^e(E)$ and two Gaussian shaped DOS distributions $g^g(E)$; both kinds of states are divided into donor-like states ($g_D(E)$) and acceptor-like states ($g_A(E)$):

$$g(E) = g_D^g(E) + g_A^g(E) + g_D^e(E) + g_A^e(E). \tag{108}$$

Exponential tails are defined as:

$$\begin{aligned} g_D^e(E) &= \frac{g_0}{2}\exp\left(-\frac{E-E_m}{E_D}\right), \\ g_A^e(E) &= \frac{g_0}{2}\exp\left(\frac{E-E_m}{E_A}\right), \end{aligned} \tag{109}$$

where g_0 is the tail distribution peak value reached at the energy E_m, E_A and E_D are the energy slopes for acceptor-like and donor-like states, respectively. Gaussian distributions are defined as:

$$\begin{aligned} g_D^g(E) &= \frac{N_D^g}{\sigma_D}\exp\left[-\frac{(E-E_D^g)^2}{2\sigma_D}\right], \\ g_A^g(E) &= \frac{N_A^g}{\sigma_A}\exp\left[-\frac{(E-E_A^g)^2}{2\sigma_A}\right], \end{aligned} \tag{110}$$

where N_D^g and N_A^g are the total number of states, σ_D and σ_A are the standard deviations, E_D^g and E_A^g are the energy peaks position for the Gaussian distributions.
Such model features a direct dependency on the doping densities and can be also applied to doped a-Si:H; the impact of dopant species on the DOS profile must be taken into

account also in the deep defect states distribution. As the Fermi level shifts towards the conduction (valence) band for n-type (p-type) materials, the donor-like (acceptor-like) defects distribution is enhanced but it maintains its position unchanged. After defining the DOS function, it is possible to derive explicit expressions for the probability occupation function of both kinds of traps:

$$f_D(E) = \frac{nC + N_V \exp\left[(E_V - E)/kT\right]}{nC + p + CN_C \exp\left[(E - E_C)/kT\right] + N_V \exp\left[(E_V - E)/kT\right]},$$
$$f_A(E) = \frac{n + CN_V \exp\left[(E_V - E)/kT\right]}{n + pC + N_C \exp\left[(E - E_C)/kT\right] + CN_V \exp\left[(E_V - E)/kT\right]}, \tag{111}$$

where n and p are free electrons and holes concentration, N_C and N_V are the densities of states in the conduction and in the valence band, E_C and E_V are the bottom and top limits of the conduction and the valence bands, C is the ratio between the trap section of a charge σ_C and the trap section of a neutral one σ_N:

$$C = \frac{\sigma_C}{\sigma_N}. \tag{112}$$

The calculated density of states is can be considered in an extended Shockley-Reed-Hall model to account for a continuous distribution of states.

3.2 JV characteristic and contact width design

As shown in [16] IBC-HJ has a 2D current from base to the emitter at the cell rear side. Carriers are mainly generated close to the front surface and have to move through the entire c-Si wafer, which is the reason why a high quality substrate is necessary. Interfaces between c-Si and doped a-Si are very defective and lead to high front surface velocities. In order to reduce such losses, thin a-Si intrinsic passivation layers are necessary. By considering a solar cell without the back amorphous intrinsic layer, the effect of p-contact and n-contact dimension are investigated. The overall device width and contacts number (five p-finger and four n-fingers) are fixed in the simulation, therefore n-strips wider, p-strips narrower. The n-contact width vary from 100 to 1400 μm and, such variation, affects only the J_{sc} value, which decreases as shown in Fig. 35. Minority carriers, generated within the n-strip region, need to travel vertically to the back junction but also along the laterally direction to reach the emitter, therefore longer paths lead to higher recombinations probability.

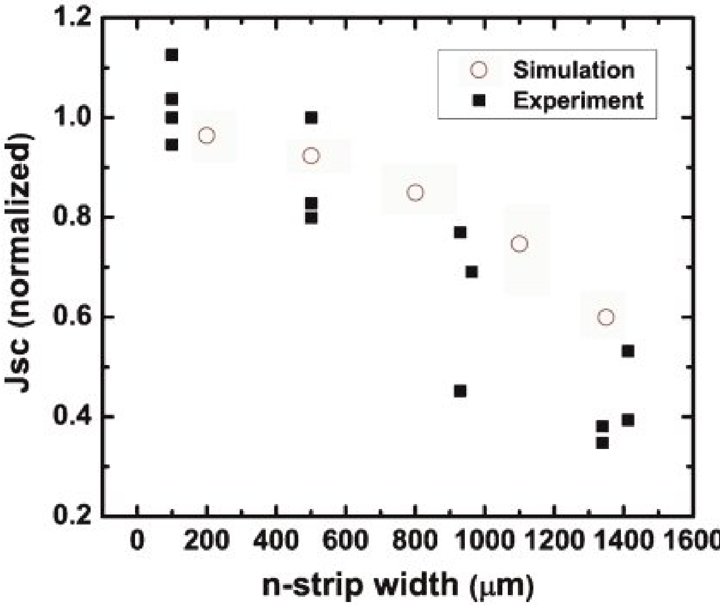

Figure 35: Sensitivity of J_{sc} to the n-contact length, where both simulated (circle) and experimental (square) results are reported [16]. The total device length is kept constant.

3.3 Benefits and disadvantages of a-Si intrinsic back layer

Surface passivation is necessary also at the back interface, between crystalline silicon and doped amorphous doped silicon (both emitter and base). Fig. 36 compares J-V curves with and without a 10 nm-thick back buffer layer of intrinsic a-Si which improves the surface passivation V_{oc} (J_{sc}) increase. Such figures of merit increase from 600 mV (27 mA/cm^2) to 683 mV (36 mA/cm^2). In order to obtain an acceptable cell performance a relatively high lifetime τ is required therefore floating zone (FZ) substrate are typically adopted in all back contact architectures for which τ is equal to 5 ms. The carriers effective lifetime τ_{eff} is affected by the interface quality, hence it depends on the presence of the a-Si buffer layer. The measured τ_{eff} reported by [16] is equal to 600 μs with the buffer layer whereas it is about 10 μs without buffer layer.
On the other hand the FF severely decreases, from 73% to 37%, and the J-V characteristic exhibits a s-shape characteristic. In [16], the performance of a front contact hetero-junction, as discussed in (2.7.2), are compared with an IBC-HJ device. With the same a-Si buffer layer thickness, the HIT solar cell does not results in a s-shape and its FF is much higher than that of the IBC cell. The FF losses are not due to shunting between n- and p- contacts, because J-V curves are both flat under reverse bias condition. The s-shape characteristic may be exhibited by IBC-HJ cells, the possible causes are: i) differences in device manufacturing process between IBC-HJ and HIT, ii) higher series resistances, iii) different bands alignment at the hetero-emitter interface and iv) the different operating conditions of the buffer layer. In case if HIT solar cells, the buffer layer is located at the front surface, therefore, it significantly affects the light absorption

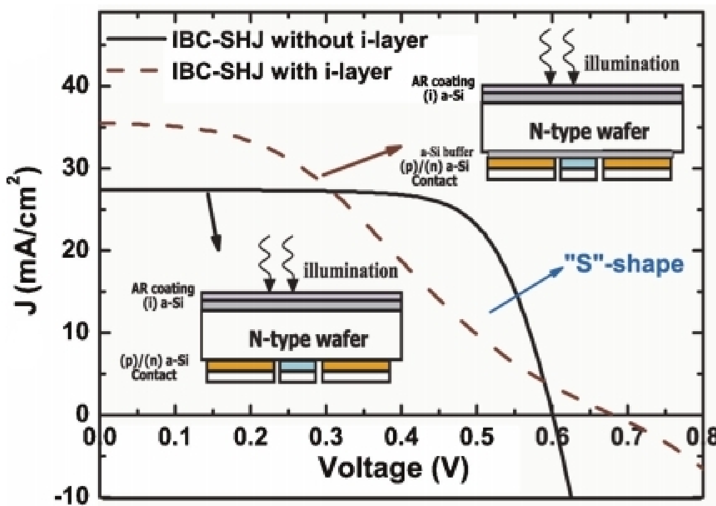

Figure 36: Illuminated J-V curves for IBC-HJ solar cells with and without back surface buffer [16].

process. IBC solar cell features higher current densities but it also has a reduced contact area, which causes additional losses due to series resistance. Different processes quality, therefore, may affect the band alignment of the two structures.

3.4 Band structure analysis

In [15] amorphous silicon bandgap width is, at first, considered equal to 1.72 eV; electron affinities of c-Si and a-Si:H are equal to 4.05 eV and 3.90 eV ,respectively. Such difference causes a discontinuity at the conduction band edge ΔE_C. In the analysis shown in Fig. 37, in which the x-axis is the distance from the back surface, the depleted region is highlighted. Such region is almost located completely into the c-Si because of the high p-contact doping and the low intrinsic layer thickness. The band bending leads to the creation of an inversion layer, which repels the majority carriers (electrons) and attracts the minority carriers (holes). The alignment of a-Si:H and c-Si Fermi levels also induces an energy barrier to holes at the interface caused by a large valence band offset ΔE_V. ΔE_V strongly depends on buffer intrinsic layer properties and its value is in a range between 0.40 eV and 0.71 eV [15].
Fig. 38 shows the band structure with a bias of 0 V and 0.5 V; at 0 V a high electric field intensity occurs, therefore, no limitation to the holes transport through the junction. At 5 eV the valence band shifts down, the electric field is reduced and the interface behaves as a potential barrier to minority carriers; the collected photocurrent is lower, FF is degraded and the J-V curve shows the typical s-shape.
At the base contact the conduction band is almost flat for both values of bias, therefore, it does not influence majority carriers transport.

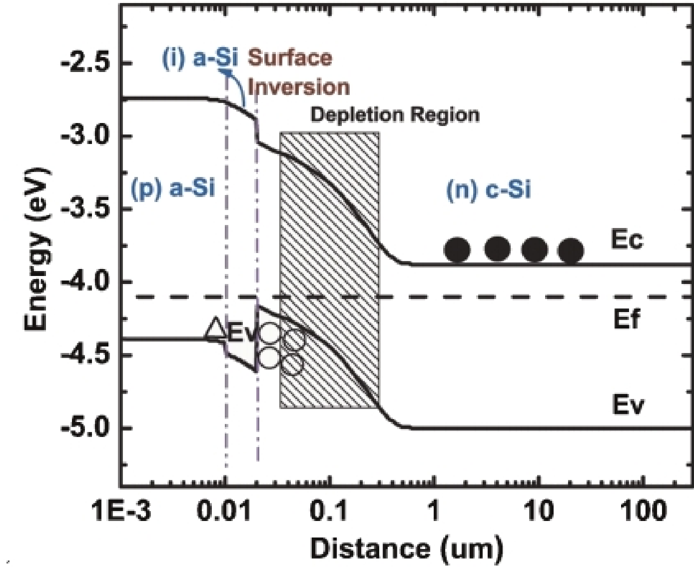

Figure 37: Equilibrium band aligment for hetero junction p-contact [16].

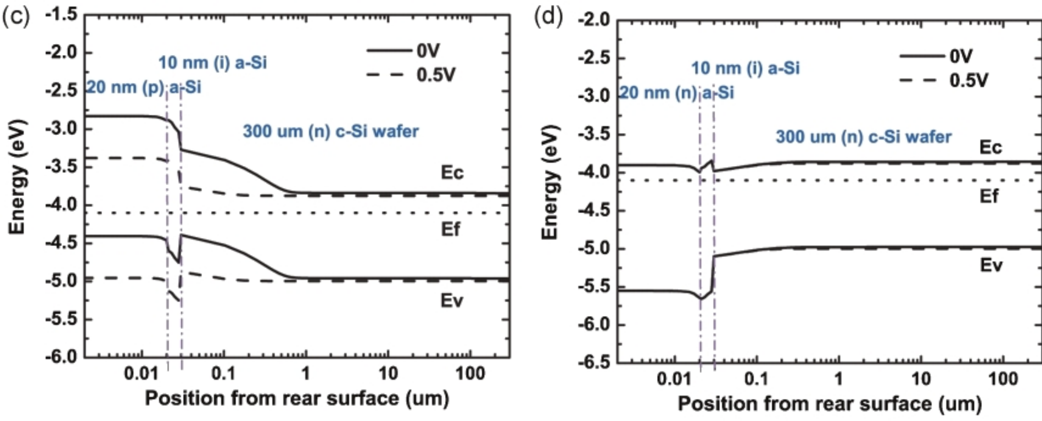

Figure 38: Bias and unbias band aligment for hetero-junction p-contact and n-contact [16].

3.5 Improving fill factor

As previously discussed, S-shaped curve is caused by the introduction of the a-Si intrinsic passivation layer on the p type emitter contact. The impact of the back buffer layer features on the main figures of merit is investigated and discussed in the following.

3.5.1 Buffer layer conductivity

One way to improve the holes transport through the buffer layer is that of properly adjusting the p-type doping process. Fig. 39 shows a JV characteristic obtained by adopting a lightly doped buffer layer, which is inserted only between c-Si and p-contact. Simulations in [16] are performed with an ideal surface passivation and a zero surface recombination velocity S at the gap between the contacts. Surface defects density and electron affinity are assumed to be constant with the doping variations; under such conditions, FF improves monotonically with increasing the doping concentrations. Experimental results show a similar FF trend with respect to the simulated one; on the other hand, V_{oc} and J_{sc} are much more degraded. Such degradation is due to the poor passivation effects of a doped a-Si layer and to the absence of passivation at both base contact and at the gap. Lifetime measurements are performed in order to estimate the passivation effectiveness of doped a-Si layers.

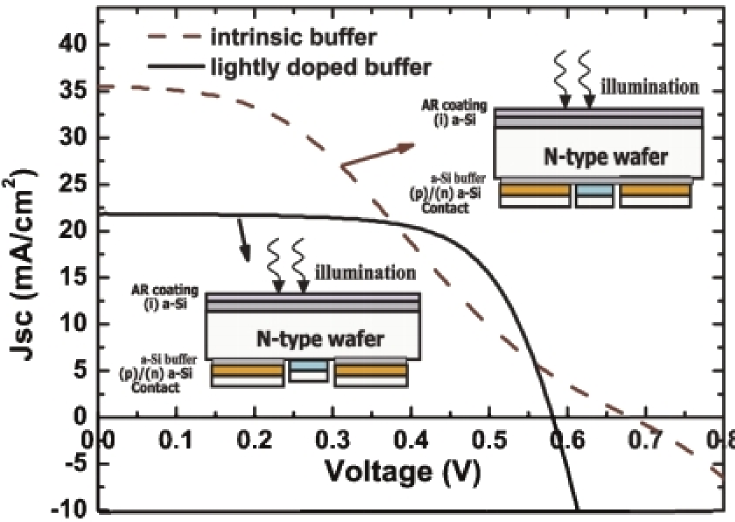

Figure 39: Experimental J-V curves with buffer layer, intrinsic and doped [16].

3.5.2 Buffer layer thickness

The buffer layer degrades the FF value whichever its thickness is, therefore as the thickness decreases, the FF improves. In Fig. 40a the band structure is shown, an increased

thickness leads to a decreasing of the band bending in the crystalline layer and to an increasing bending in the amorphous silicon, in order to maintain the charge balance. Such effects result in a lower electric field which leads to a higher and wider potential barriers for holes, therefore their transport to emitter became more difficult. Once the thickness is reduced, also its passivating effect is less effective, as it result from experiments shown in Fig. 40b, therefore the open circuit voltage V_{oc} results reduced.

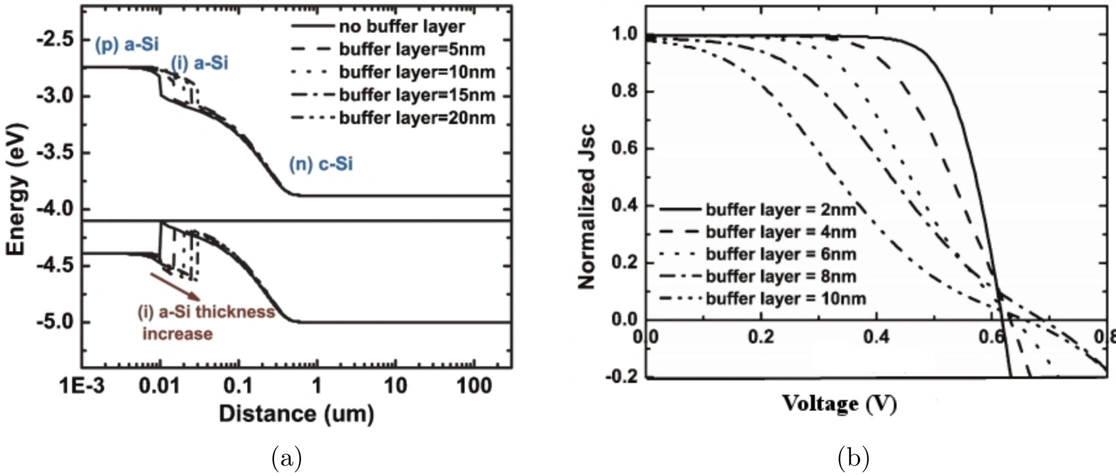

(a) (b)

Figure 40: Equilibrium band structure and experimental JV characteristic with a-Si buffer layer thickness as parameter [16].

3.5.3 Back surface i-layer bandgap

Bandgap of amorphous silicon can be changed by means of modifications related to its fabrication process. In [15] is reported that by lowering the rear i-layer's bandgap below 1.65 eV it is no more a good passivating layer. In Fig. 41 the impact of different bandgaps width in the J-V characteristic is illustrated, FF improves with smaller value of E_g because of smaller valence offset ΔE_V. J-V characteristic s-shaped results from larger bandgap and higher potential barrier.

In [15] three sets of simulations are performed to evaluate the influence of the bandgap width on fill factor with three different values of thickness: 5 nm, 8 nm, 10 nm. Fig. 42 reports the results and shows that, in order to increase the FF, a back buffer with lower bandgap width is necessary. Lower buffer thickness allows higher E_g with relatively improved FF values.

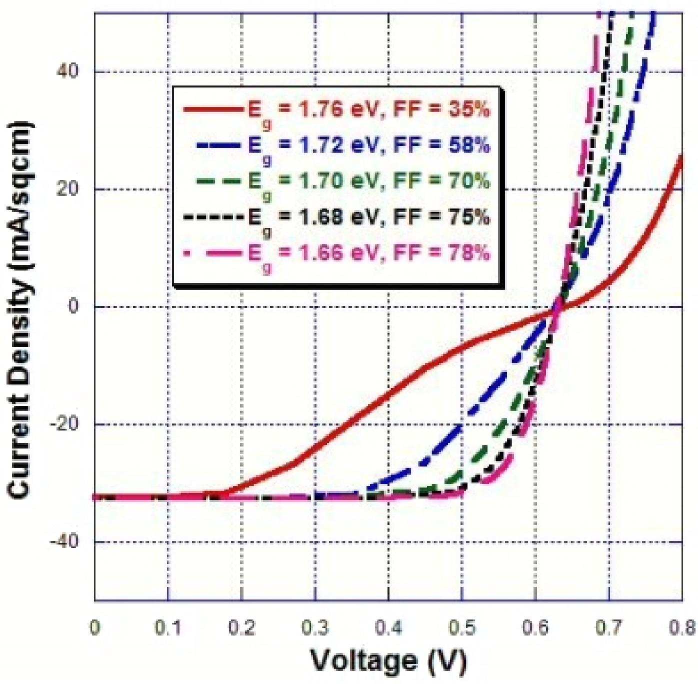

Figure 41: Simulated J-V curves with a 8 nm-thick buffer layer with variable E_g [15].

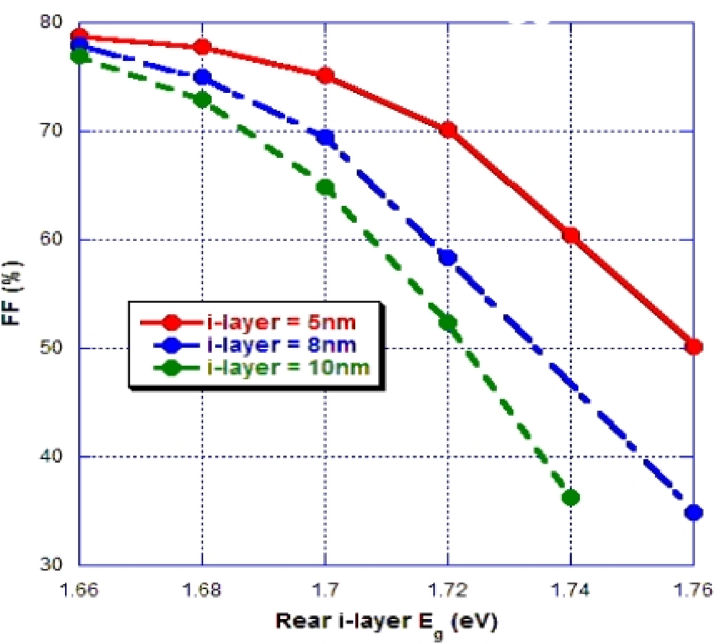

Figure 42: FF trends versus intrinsic a-Si layer bandgap E_g. Three different thicknesses are simulated [15].

3.6 Doped layers defects

Allen and co-authors [15] analyzed in detail the dependency of all main figures of merit on the defects distribution in the doped amorphous silicon layer. Two exponential band tails and two Gaussian midgap distributions have been accounted for. Results are summarized in Fig. 1 in which densities are defined by H and $L(2 \cdot 10^{19} cm^{-3} eV^{-1}$ and $2 \cdot 10^{16} cm^{-3} eV^{-1}$ respectively). H^* indicates an increase of two magnitudes orders in the intrinsic layer defects, while in the doped layer defects are equal to H. Tail state energies are kept constant at 0.07/0.12 eV, instead of midgap defects in the a-Si doped layers, which are varied one at the time in order to estimate their influence on the cell performance. The increase in n-contact dangling bonds concentration does not significantly affect the device performance, on the other hand a three magnitude orders increase in p-contact midgap traps reduced FF of about 11% and V_{oc} of 10 mV.
Other simulations are performed with narrower band tails at the a-Si doped layer, from 0.12/0.07 eV to 0.07/0.04 eV. FF improves of almost 5% and the s-shape at the J-V curve does not appears, which is not dependent on the midgap defects density. Since band tail states are responsible for shallow trapping while midgap states are responsible for recombinations in [15] authors concluded that S-curves are due to trapped charge rather than recombination in the doped layer. Midgap defects in the i-layer have a negligible effect on the cell performance; possible explanations for such effects are: i) i-layer defect densities are much lower than those in doped layers, ii) high electric field intensity ensures negligible recombinations in the buffer layer and/or iii) SRVs do not dependent on i-layer defects density.

Tail state energies	p^{db} density	n^{dp} density	V_{oc} mV	J_{sc} mA/cm^2	FF %	Eff. %
0.12/0.07 (eV)	L	L	675	34.1	75.0	17.3
	L	H	674	34.0	74.9	17.2
	H	L	666	34.1	63.4	14.4
	H	H	665	34.0	63.3	14.3
	H*	H*	665	34.0	63.0	14.2
0.07/0.04 (eV)	L	L	675	33.9	79.7	18.2
	H	H	676	34.1	78.4	18.1

Table 1: Effect of dangling bonds midgap defects and tail states on cell figures of merit [15].

3.7 Impact of c-Si resistivity

The influence of bulk resistivity ρ on cell performance are simulated in Diouf and co-authors [23] article, the dependence of ρ on the bulk recombinations is expressed as:

$$\rho = \frac{1}{q\mu_n N_{c-Si}}, \tag{113}$$

where N_{c-Si} is the doping concentration in the substrate. By considering only Auger and SRH bulk recombination mechanisms and by neglecting surface recombinations, the effective lifetime is:

$$\frac{1}{\tau} = \frac{1}{\tau_{SRH}} + \frac{1}{\tau_{Auger}}, \tag{114}$$

where Auger recombinations become dominant at high doping concentration, in which ρ is low. The impact of c-Si resistivity for substrate with different lifetimes on cell performance is shown in Fig. 43. As ρ decreased the V_{oc} at first increases and then decreases, due to higher Auger recombinations with higher doping densities. Such recombinations are also very effective to short circuit current. FF increases with decreasing ρ, due to a reduction of the potential drop in the substrate. An optimum value of bulk resistivity can be found in the efficiency line graph; a quite flat characteristic can be observed, therefore, ρ can be chosen within rather wide range. As consequence of the several competing mechanisms occurring, the chosen ρ is equal to 2.5 $\Omega \cdot cm$ high quality FZ wafer with a lifetime equal to 5 ms.

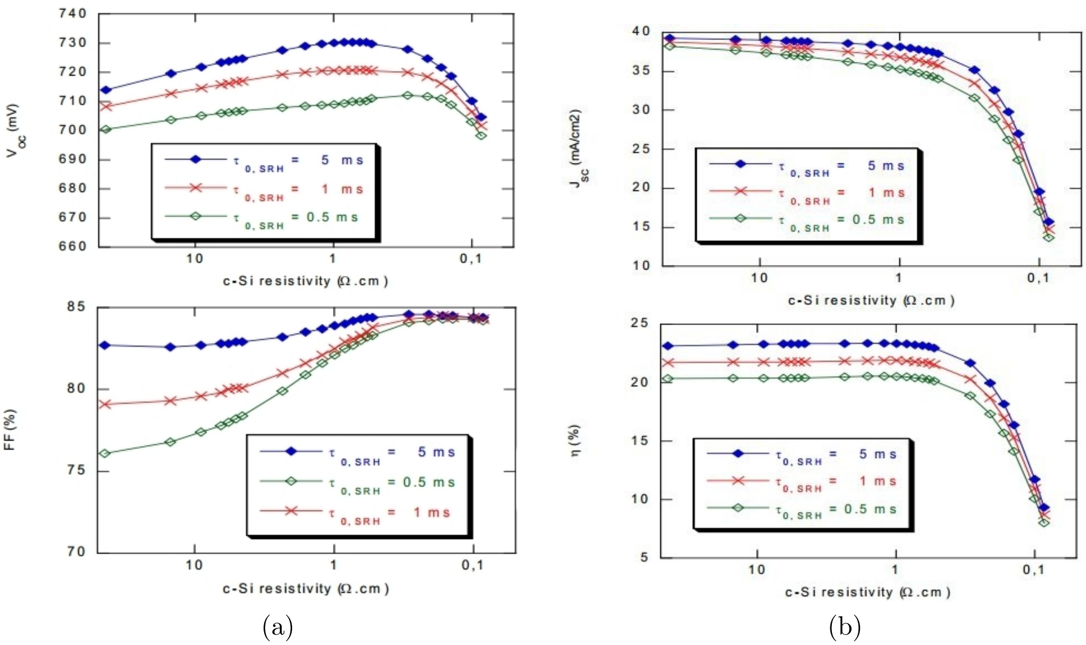

Figure 43: Impact of c-Si resistivity on the main figures of merit [23].

4 Numerical simulator

The numerical simulator used in this thesis is Sentaurus, the commercial tool by Synopsys; the typical tools flow is illustrated in Fig. 44. Sentaurus is a software environment capable of simulating the electrical, thermal and optical behaviour of semiconductor devices. Such general purpose simulation tool offers simulation capability in many categories of devices like: CMOS technologies, compound semiconductor technologies, optoelectronic devices, power electronic devices, Monte Carlo device simulations, memory devices, radiation effects as well as novel semiconductor technologies. Modeling and simulation of integrated circuit devices are useful at the research and development stage because it allows to minimize the development time and to perform an easier performance optimization. Once a conceptual model has been developed and tested, device performance can be easily studied and optimized. The main tools necessary in this work are: Sentaurus structure editor, Sentuarus device, Inspect and Sentaurus visual. Inspect and Sentaurus visual are necessary to visualize and to post-process the spatial resolved maps of carrier lifetimes, electric fields as well as of calculated output data, much as current-voltage.

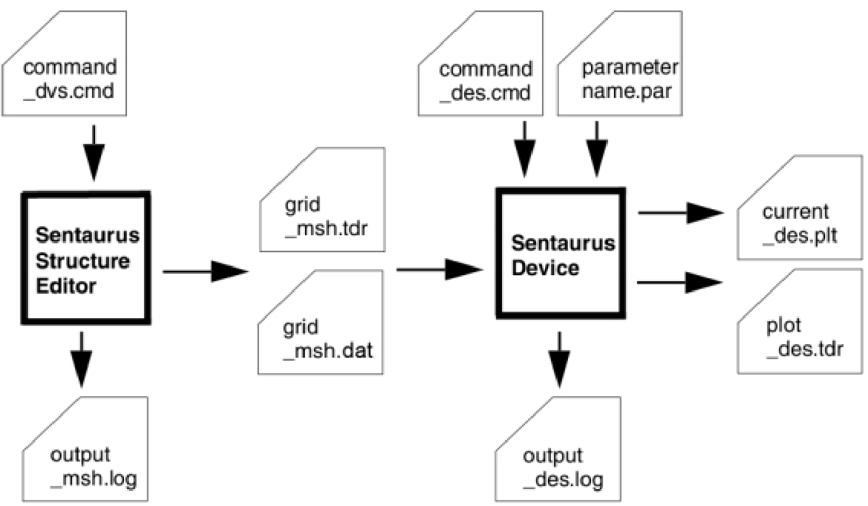

Figure 44: Simulation tools flow in Sentaurus [25].

4.1 Sentaurus structure editor

Sentaurus structure editor allow to create 2D and 3D architectures by means of basic shapes such as rectangles, cuboids, circles and cylinders and to define different regions within those. For each regions constituent materials and doping profiles have to be defined in the model; doping profile can be constant, analytic or externally generated. In order to solve the drift diffusion model equations by the electrical simulator the si-

mulation domain has to be discretize by means of a mesh. In order to generate such mesh, Sentaurus produces the necessary input files (either DF-ISE boundary file or TDR boundary file), moreover, it can also defined local refinements and loads external submeshes. Electrical contact regions have to be defined and placed. Output files are the grid file `grid_mesh.tdr` and the data file `grid_mesh.dat`, whose include information about: i) the main structure, ii) the doping profile and iii) the mesh refinement. Furthermore, the `*.tdr` and `*.dat` are input files for the Sentaurus device tool, which is outlined in the following subsection. All the possible geometrical operations are specified in the Synopsys user guide [24].

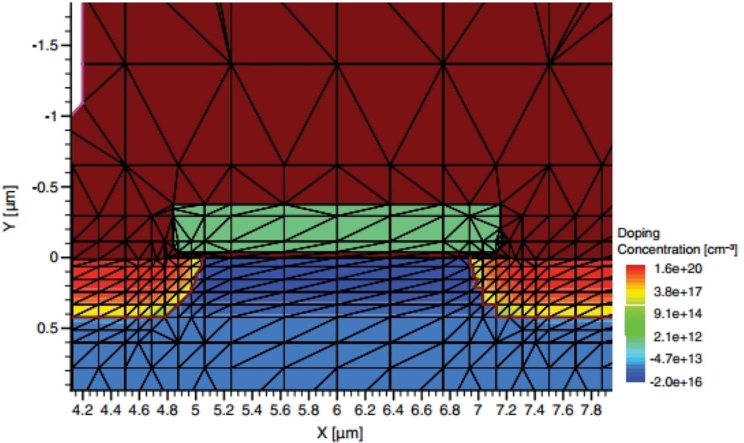

Figure 45: Design example of a MOS architecture, in which mesh and doping profile are defined [25].

4.1.1 Simulated symmetry element

In order to model the reference architecture, in Fig. 33, and to save computation time a basic structure has been considered. The main feature of such basic structure is that of be a symmetry element for the entire solar cell. All the geometrical features of this symmetry element, which are imported in the structure editor, are listed in Tab. 2. Doping concentrations are also implemented and their set values are in Tab. 3; a-Si doping densities have been taken from [15] whereas cSi doping concentration value has been considered from [16].

ARC	30 nm	aSiBottom	5 nm	p length	600 μm
FrontPass	70 nm	pcont	20 nm	n length	250 μm
aSiTop	5 nm	ncont	20 nm	gap length	25 μm
cSi	150 μm	BackPass	30 nm		

Table 2: Geometrical parameters of the elementary cell.

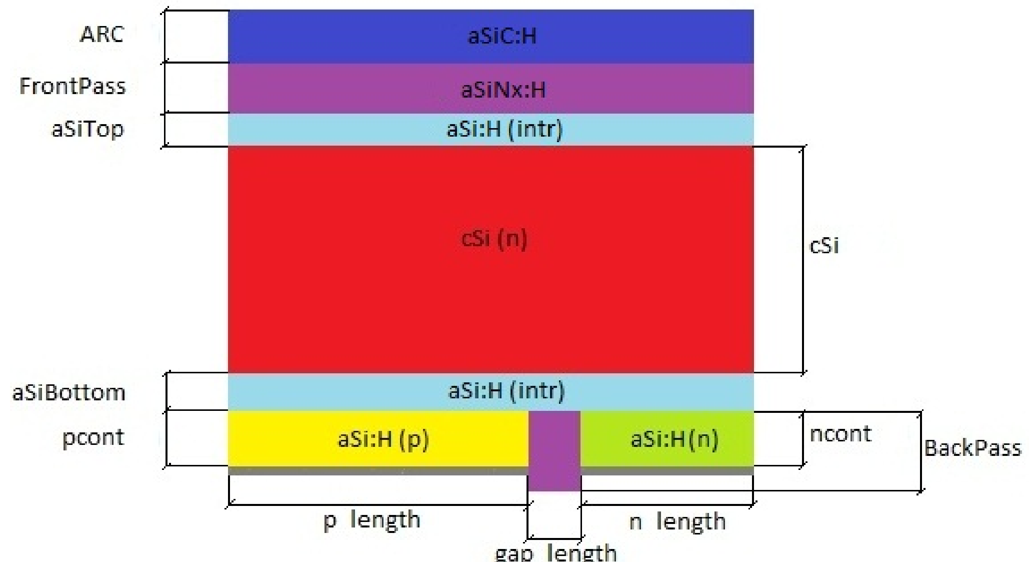

Figure 46: Element of symmetry if the simulated structure.

	cSi	aSi:H (intr)	aSi:H (p)	aSi:H (n)
Doping densities (cm^{-3})	$1.90 \cdot 10^{15}$	$2.20 \cdot 10^{15}$	$2.05 \cdot 10^{19}$	$1.51 \cdot 10^{19}$
Type	Phosphorus	Phosphorus	Boron	Phosphorus

Table 3: Doping concentrations adopted for the simulation described in 4.1.1.

4.2 Sentaurus device

Sentaurus device is a drift-diffusion numerical solver which computes the carriers transport coupled with the Poisson and the continuity equations in a self-consistent way. The input files of this tool are: i) the structure editor output (as `grid_mesh.tdr` and `grid_mesh.dat`), ii) the command file `command_des.cmd` and iii) the parameter file `parameter_name.par`, in which all the physical parameters are defined. The `*.tdr` file contains a description of each region, with its boundaries and its materials, the location of the electrical contacts as well as the locations of all the discrete nodes. The data file `*.dat` contains the device properties, such as the doping profiles, in form of data associated to discrete nodes. The command file can be organized in six different sections: the *file section* in which the input and the output file are defined, the *electrode section* with the definitions of the boundary conditions, the *physics section* in which all the physical models are chosen, the *plot section* which contains all the plot to save in the output file, the *math section* defines the numerical parameters of the specifc solver and the *solve section* which defines the problems to solve.

4.2.1 Models implemented

In the `*_des.cmd` file all the necessary parameters are set and, with regard to the entire structure, the Fermi statistics and a temperature of $T = 298.15\ K$ are defined. In the c-Si physics section several models are implemented; the activated recombination models are: i) Auger, ii) radiative and iii) doping dependent SRH. Sentaurus device supports different methods to compute the electron mobility, such as `PhuMob(Phosphorus)`. Mobility saturation, due to high electric field intensity value, is also considered by means of the `HighFieldSaturation` command. The bandgap model can be selected within the `EffectiveIntrinsicDensity` statement, in which the impact of doping density on the bandgap narrowing are taken into account by means of a table, which is specified in the parameter file by means of the `BandGapNarrowing(TableBGN)` keyword. In case of amorphous silicon a-Si, less standard models exist, therefore a wider set of physical features have to be defined in the parameter file. Mobility values for a-Si are constant, from [27], independently on doping concentration and they are specified in the parameter file as shown in Tab. 4:

	electrons	holes
$\mu\ (cm^2/Vs)$	1	0.1

Table 4: Constant mobility values which are set for a-Si.

Exponential traps distribution has to be defined, as in the section (3.1.1), as:

$$g^{exp}(E) = N_0 \exp\left(-\left|\frac{E - E_0}{E_S}\right|\right), \tag{115}$$

while Gaussian distributions are express as:

$$g^{gauss}(E) = N_0 \exp\left(-\frac{(E - E_0)^2}{2E_S^2}\right). \tag{116}$$

N_0, which is the defects density, is defined by `Conc`, E_0 is the density of states (DOS) peak energy and it can be set by `EnergyMid` and E_S is the standard deviation `EnergySig`. Other keywords are necessaty to specify an energy reference for each of the previously parameters, which can be either the valence band edge `FromValBand` or the conduction band edge `FromCondBand`. Electrons and holes capture cross section are defined by `eXsection` and `hXsection`, respectively. Traps densities in a-Si depend on doping concentrations, therefore, different parameters for intrinsic, n-type doped and p-type doped have to be implemented. A typical DOS for a p-type a-Si is illustrated in Fig. 47 and the related parameters are in Tab. 7.

	Exponential donor-like states	Exponential acceptor-like states	Gaussian donor-like states	Gaussian acceptor-like states
Reference point	valence band	conduction band	valence band	valence band
`Conc` (cm^{-3})	10^{18}	10^{18}	10^{16}	10^{16}
`EnergyMid` (eV)	0.00	0.00	0.90	1.10
`EnergySig` (eV)	0.09	0.06	0.15	0.15
`eXsection` (cm^2)	10^{-15}	10^{-17}	10^{-14}	10^{-15}
`hXsection` (cm^2)	10^{-17}	10^{-15}	10^{-15}	10^{-14}

Table 5: Intrinsic a-Si DOS set parameters.

	Exponential donor-like states	Exponential acceptor-like states	Gaussian donor-like states	Gaussian acceptor-like states
Reference point	valence band	conduction band	valence band	valence band
`Conc` (cm^{-3})	10^{21}	10^{21}	10^{19}	10^{19}
`EnergyMid` (eV)	0.00	0.00	0.45	0.70
`EnergySig` (eV)	0.12	0.07	0.20	0.20
`eXsection` (cm^2)	10^{-15}	10^{-17}	10^{-14}	10^{-15}
`hXsection` (cm^2)	10^{-17}	10^{-15}	10^{-15}	10^{-14}

Table 6: n-type doped a-Si DOS set parameters.

	Exponential donor-like states	Exponential acceptor-like states	Gaussian donor-like states	Gaussian acceptor-like states
Reference point	valence band	conduction band	valence band	valence band
`Conc` (cm^{-3})	10^{21}	10^{21}	10^{19}	10^{19}
`EnergyMid` (eV)	0.00	0.00	1.10	1.30
`EnergySig` (eV)	0.12	0.07	0.20	0.20
`eXsection` (cm^2)	10^{-15}	10^{-17}	10^{-14}	10^{-15}
`hXsection` (cm^2)	10^{-17}	10^{-15}	10^{-15}	10^{-14}

Table 7: p-type doped a-Si DOS set parameters.

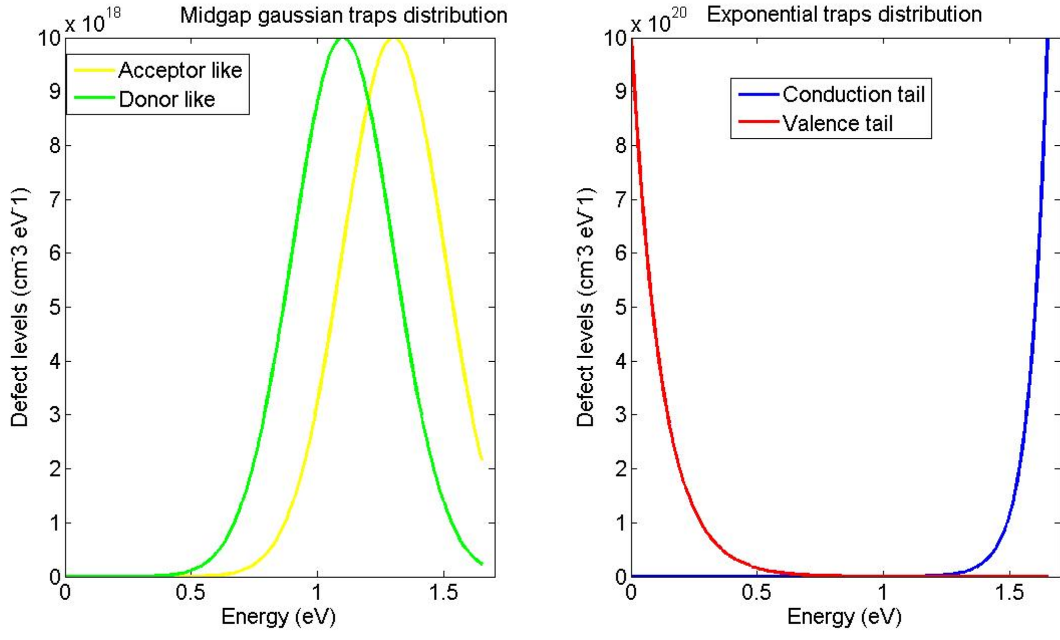

Figure 47: Traps distribution in p-type doped a-Si.

Each implemented model in the parameter file have tunable parameters. In c-Si substrate the average lifetime adopts the Scharfetter model, which is doping and temperature dependent is :

$$\tau = \tau_{min} + \frac{\tau_{max} - \tau_{min}}{1 + \left(\frac{N}{N_{ref}}\right)^{\gamma}}, \tag{117}$$

in which parameters are set as in Tab. 8 in order to obtain a certain lifetime value (5 ms in the table).

	electrons	holes
τ_{min} (s)	0.00	0.00
τ_{max} (s)	0.01	0.01
N_{ref} (cm^{-3})	$1.90 \cdot 10^{15}$	$1.90 \cdot 10^{15}$
γ (1)	0.00	0.00

Table 8: Scharfetter model setting.

Auger recombination rates can be obtained by equation 39, furthermore, electrons and holes Auger coefficients can be both modified by means of this formula:

$$C_{n,p} = \left(A + B\left(\frac{T}{T_0}\right) + C\left(\frac{T}{T_0}\right)^2\right)\left(1 + H\exp\left(-\frac{n,p}{N_0}\right)\right), \tag{118}$$

where T_0 is 300 K, while the others parameters have been listed in Tab. 9:

	electrons	holes
A (cm^6/s)	$2.800 \cdot 10^{-31}$	$7.910 \cdot 10^{-32}$
B (cm^6/s)	0	$-1.239 \cdot 10^{-32}$
C (cm^6/s)	0	$3.231 \cdot 10^{-32}$
H (1)	8	8
N_0 (cm^{-3})	$2.500 \cdot 10^{17}$	$2.500 \cdot 10^{17}$

Table 9: Auger coefficients setting.

Bandgap width model in c-Si is expressed as:

$$E_g = E_{g0} + dE_{g0} + \alpha \frac{T_{par}^2}{\beta + T_{par}} - \alpha \frac{T^2}{\beta + T}, \tag{119}$$

where E_{g0} is equal to 1.175215, the others are default Sentaurus parameters in case of c-Si whereas dE_{g0} is the bandgap narrowing term, which values are listed in the `TableBGN`. In order to set the electron and hole effective masses in a-Si, the keywords `eDOSMass` and `hDOSMass` are necessary. Furthermore such values are constant and defined as in [27] as $2.50 \cdot 10^{20}$ (cm^{-3}). The same bandgap model of c-Si (equation (119)) is assumed but without considering the bandgap narrowing effect. E_g values, for each a-Si layers, are listed in Tab. 10 in which the E_{g0} value are modified in order to obtain the desired bandgap value. Electron affinity, which is the difference between vacuum energy and the conduction band edge, is model as:

$$\chi(T) = \chi_0 + \frac{(\alpha + \alpha_2)T^2}{2(T + \beta + \beta_2)} + \texttt{Bgn2Chi} \cdot E_{bgn}, \tag{120}$$

where χ_0 is constant and the other parameters are standard.

	i-layer(Front)	i-layer (Back)	p-layer	n-layer
E_g (eV)	1.78	1.72	1.65	1.72
E_{g0} (eV)	1.82541	1.76541	1.69541	1.76541
χ (eV)	3.90	3.90	3.90	3.90
χ_0 (eV)	3.87726	3.87726	3.87726	3.87726

Table 10: Bandgap model parameters.

Traps parameters have been also set: i) `G` is the degeneracy factor, which is the number of electronic states at the same energy level, ii) `Xsec` is the capture cross section and iii) `v_th` is the thermal velocity.

Such parameters define the capture rate for both electrons and holes as:

$$c_C^n = \sigma_n^0 v_{th}^n n,$$
$$c_V^p = \sigma_p^0 v_{th}^p p, \tag{121}$$

where the thermal velocity model is:

$$v_{th}^{n,p} = v_0^{n,p}\sqrt{\frac{T}{300}}. \tag{122}$$

	electrons	holes
G (1)	1	1
Xsec (cm^2)	10^{-15}	10^{-15}
v_th (cm/s)	$2.042 \cdot 10^7$	$2.042 \cdot 10^7$

Table 11: Traps further setting for amorphous silicon.

Front and back surface recombinations between c-Si and a-Si are model as:

$$S = S_0\left[1 + S_{ref}\left(\frac{N_i}{N_{ref}}\right)^{\gamma}\right], \tag{123}$$

where S_{ref} was fixed equal to zero, therefore $S = S_0$; its values are listed in Tab. 12.

S_0 (cm/s)	electrons	holes
Front	10	10
Back	20	20

Table 12: Recombination surface velocity.

Interfaces between a-Si and c-Si are abrupt heterojunctions, which are supported by Sentaurus. In order to model them the keyword `HeteroInterface` has to be specified within the physics section of the command file. In case of abrupt interfaces the conventional transport equations are not valid, therefore currents and energy flux have to be redefined. In heterojunctions also the thermionic emission current, for both electrons and holes, has to be activated by means of the keyword `Thermionic`.
Fixed charges within silicon nitride can be implemented by the keyword `FixedCharge` in the physics section, the value of such density is constant and equal to $5 \cdot 10^{16}$ cm^{-3}.

4.3 Optical simulation

Optical generation rate profile in a structure can be either imported from an external file or calculated. Four different methods are possible in order to compute the optical generation map by means of Sentaurus: i) raytrace (RT), ii) beam propagation (BPM), iii) transfer matrix (TMM) and iv) finite-difference time-domain (FDTD). Furthermore, for each one, it is necessary to define excitation parameters, to choose a proper refractive index model and to control the solution achievement within the solve section of the command file. *Finite-difference time-domain* and *beam propagation method* are not used in this thesis, therefore, they are not outlined. *Transfer matrix method* is suitable to calculate the propagation of plane waves through layered media. Each layer must be homogeneous, isotropic, optically linear and the amplitudes of forward and backward running waves are calculated in each layer by means of transfer matrices. Such matrices are function of the complex wave impedances which depend on complex refraction indexes and refraction angles. *Raytrace method* assumes linear polarization and refraction, transmission, and reflection are obtained under the assumption of geometric optics, as described in subsection (1.5.1), moreover, different boundary conditions can be defined.

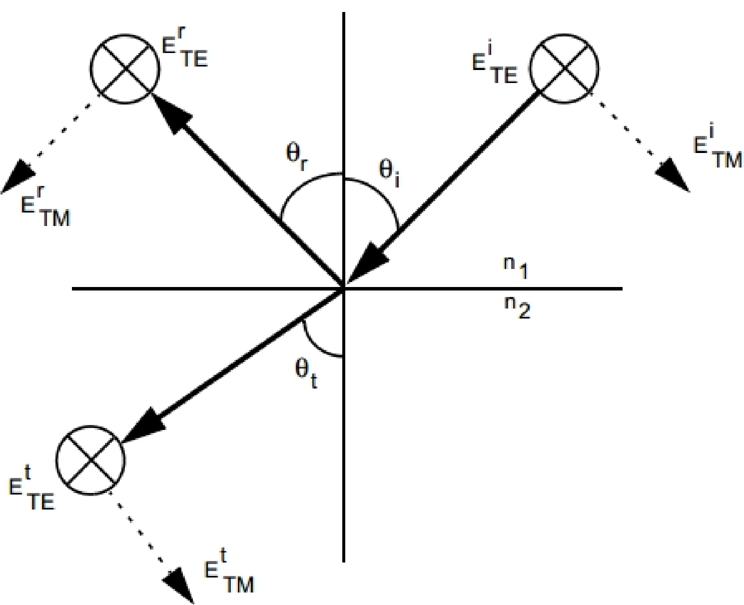

Figure 48: Incident ray splits into reflected and transmitted rays at an interface [25].

The recursive raytrace algorithm, starts with a source ray, builts a binary tree in which reflected and transmitted rays are traced within the device. A ray is defined as a plane wave in which its polarization vector exhibits a direction which is perpendicular to that of propagation. It worth noticing that the boundary conditions (BC) can be specified in different ways: Fresnel BC, Constant reflectivity/transmittivity BC, raytrace PMI BC, multilayer antireflective coating BC and photon-recycling BC. In order to simulate a

solar cell architecture with thin back and front layers the multilayer boundary condition is necessary. The raytracer simulator treats the physics of thin film layers by means of TMM method in order to compute the BC, therefore, during the raytrace process it neglects such layers. Raytracer simulator is the only method in order to simulate textured solar cells. Lastly, the resulting optical generation profile must be imported in the electrical simulator in order to simulate the illuminated response of a device. The extraction of a 1D optical generation profile from 2D or 3D structures is possible by means of a transformation of the z-coordinate. Such transformation is performed in a fashion to maintain constant the number of photogenerated carriers in the volume of the integration regions in the original textured layer and in the cuboid volume of the 1D profile, as shown in Fig. 49.

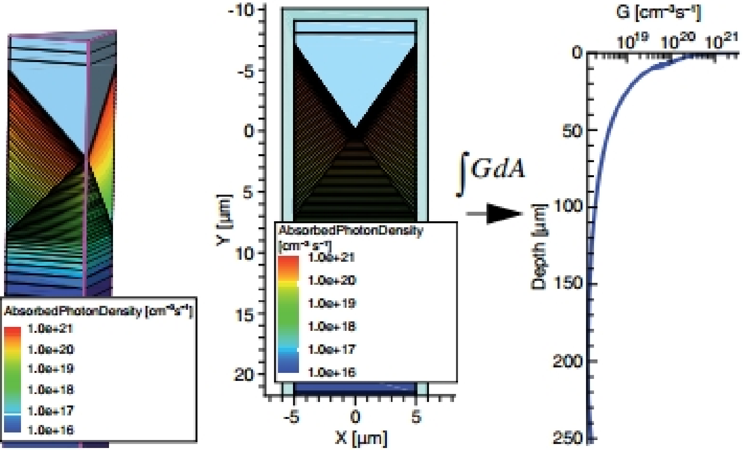

Figure 49: Integrating horizontal slices to extract 1D optical generation profiles [28].

4.3.1 Complex refraction indexes

Wavelength dependent complex refractive indexes are key parameters which are necessary to the optical simulation, regardless of the considered method. Refractive indexes n and absorption coefficients k, for both a-Si and c-Si, are known and included within the parameter file. The anti reflecting coating (ARC) is formed by an a-Si:H/a-SiNx:H/a-SiC:H stack. Such ARC has been analysed by Shu and co-authors [17]. The complex refractive index depends on fabrication parameters, as the gas flow rates R of the different layers, and an optimized stack was outlined in [17]. In Fig. 50 n and k for different gas flow rates are reported, the optimum stack features aSiNx:H with a $R_{NH_3/SiH_4} = 2$ (blue line) and aSiC:H with a $R_{CH_4/SiH_4} = 5$ (blue line). Values of n and k was extrapolated from the figure and, then, imported in the device structure.

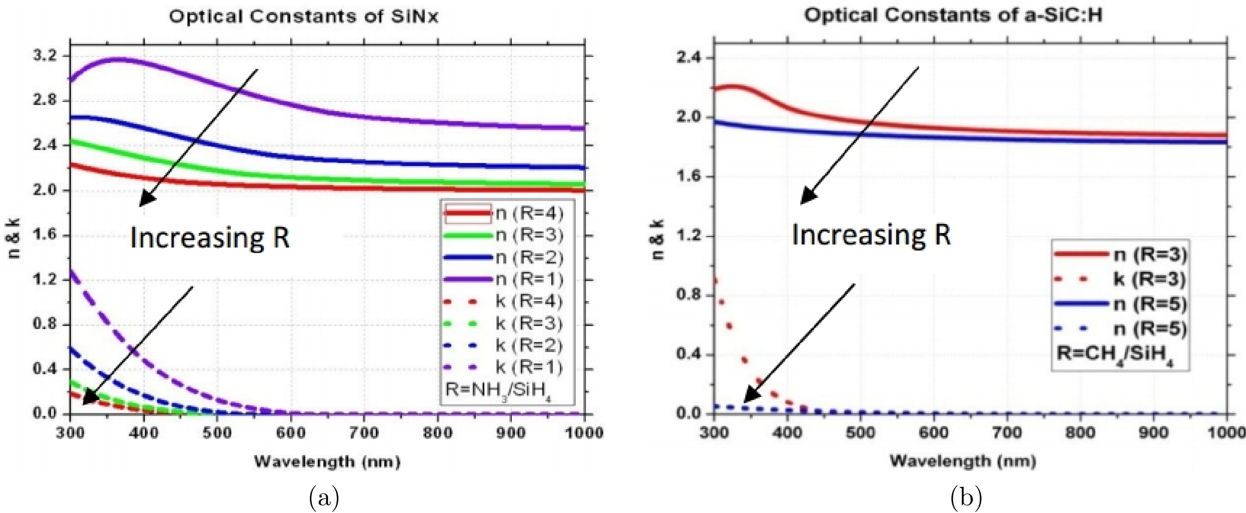

(a) (b)

Figure 50: Complex refraction indexes of ARC layers [17].

4.3.2 Transfer matrix method setting

An example of 1D TMM method is described in the Synopsys application note [28]. In the `*_des.cmd` file wavelength-dependent complex refractive index model is considered by using the `ComplexRefractiveIndex` keyword with the `WavelengthDep(Real Imag)` option. The properties of incident light are defined within the excitation section by means of the keywords `Polarization` and `Theta` (incident angle). In the case of a direct and unpolarizated light (`Theta` = 0 and `Polarization` = 0.5). The illumination window has to be defined, in the case of an all back solar cell it covers the whole cell. Within the optical solver section the the superstrate and the substrate have to be defined. TMM has two ways to solve the optical problem, `StandingWave` and `Envelope`; the first one accounted for the interference effects due to standing waves and the light phase whereas the second one neglects them. Such approximation is valid only in case of thick layer, as the c-Si bulk substrate of the reference architecture. Moreover, the `NodesPerWavelength` set the number of nodes for each wavelength in order to perform the optical equation, it is set to 1000.

4.3.3 Raytracing setting

A raytracing 3D simulation example is described in the Synopsys application note [29]. Textured and planar surface can be both simulated. In both cases the overall volume of the semiconductor material is kept constant. The number of rays can be defined in the workbench by setting `NRays`. TMM is necessary for the optical simulation of the thin layers, located in both front and back interfaces of the device. `ComputeFromMonochromaticSource` activates the optical generation computation by means of a single wavelength, outlined within the excitation section, in which the light

intensity is as well set to a value of 0.1 W/cm^2. Within the optical solver section, various parameters have to be defined: i) the incident angle by `theta`, ii) a polarization vector for the starting ray by `PolarizationVector` $= (1, 1, 0)$ set, iii) the direction vector of the starting rays by `RayDirection` and iv) the stopping criteria for the raytracer. Such criteria have to be defined by means of `DepthLimit`, which sets the maximum number of material boundaries that a ray can pass through, and `MinIntensity`, which controls the minimum intensity of a ray for which the raytracer has to keep trace.

NRays	DepthLimit	MinIntensity
50000	80000	10^{-5}

Table 13: Raytracer setting.

5 Optical simulation

In order to perform a proper optical simulation of an IBC-HJ, two different cell structures, as in Fig. 51, have to be considered, therefore two optical generation profiles have been imported. The two sections are distinguished by their back layers which are doped a-Si and aluminum, in the first section (A), whereas it is only a silicon nitride passivating layer in the second section (B).

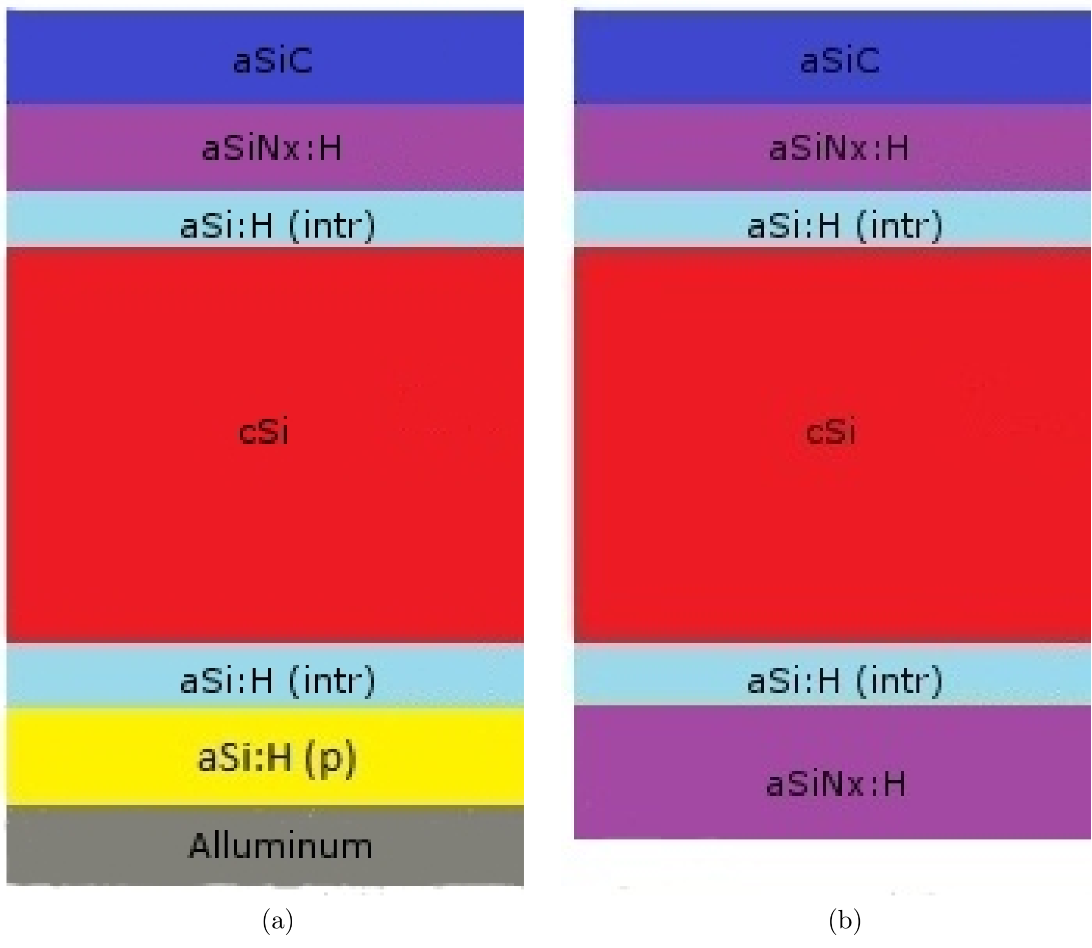

(a) (b)

Figure 51: Different cross sections assumed in the optical simulation.

The resulting optical generation profiles are imported within the IBC-HJ structure in Fig. 46, regardless of the simulation method. The photocurrent density J_{ph} can be obtained by means of the following equation:

$$J_{ph} = q \int_V GdV = qW \int_S GdS, \quad (124)$$

where W is the cell depth. Such length can be obtained by assuming a surface device area of 1 $cm^2 = 10^8$ μm^2 as:

$$W = \frac{S}{L} = \frac{10^8}{875}\ [\mu m] = \frac{10^8}{875} 10^{-4}\ [cm], \tag{125}$$

where the device length L is, at first, the value reported by Tab. 2. The resulting photogenerated density current expression is:

$$J_{ph} = qW \int_S GdS\ \left[A/cm^2\right] = qW 10^3 \int_S GdS\ \left[mA/cm^2\right], \tag{126}$$

where $\int_S GdS$ is a value which can be calculated by Sentaurus visual.

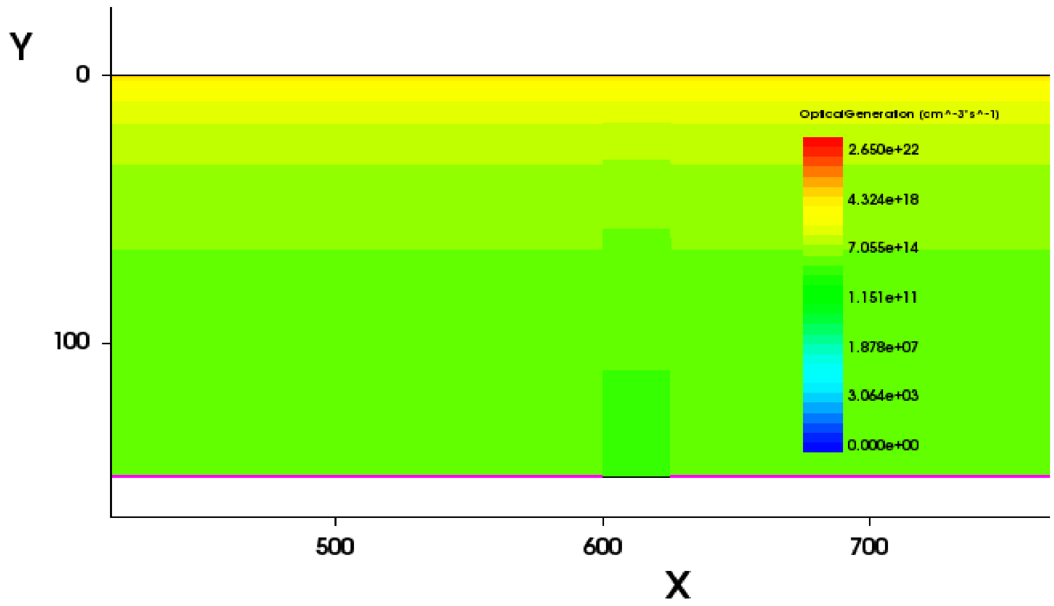

Figure 52: Optical generation profile in the 2D IBC-HJ architecture.

5.1 Transfer Matrix Method results

The first simulation was performed by means of TMM as described in (4.3.2). Two different values of the substrate thickness have been simulated, 150 μm and 300 μm. The impact of bulk thickness on the photogenerated current is evaluated. In order to validate the TMM simulator, Shu and co-authors article [17] is considered as reference. The ARC stack is formed by a 5 nm aSi layer, 40 nm aSiNx:H and 60 nm aSiC:H whose complex refractive indexes are reported in subsection (4.3.1). The TMM simulation setup was successfully validated by means of comparison with the article results, as listed in Tab. 14.

A different ARC is considered, as in Fig. 46; TMM simulations are performed for an ideal front layer and a real one, in which the optical absorption is accounted for.

Simulated value	Literature
34.66 mA/cm^2	34.80 mA/cm^2

Table 14: TMM simulator validation.

The resulting photogenerated currents J_{ph} are reported in Tab. 15, therefore undesired photons absorption in aSiNx:H and aSiC:H leads to a 0.6 mA/cm^2 loss.

ideal ARC	real ARC
33.93 mA/cm^2	33.33 mA/cm^2

Table 15: TMM simulator results.

The J_{ph} of the two sections, both A and B, are computed and the results are reported in Tab. 16.

	Section A	Section B
ideal ARC	35.20 mA/cm^2	34.03 mA/cm^2
real ARC	34.32 mA/cm^2	33.16 mA/cm^2

Table 16: TMM simulator results distinct by section.

A c-Si substrate thickness of $300\mu m$ is considered, hence as the absorbing material increases the amount of photogenerated electron-hole pairs. A single layer ARC, which is formed by a 75 nm layer of silicon nitride SiNx, is considered as in the Lu and co-authors [16] article. The complex refractive index of SiNx is defined as its default Sentaurus value. The resulting photocurrent is reported in Tab. 17.

5.2 Raytracing results

In the case of the raytracer simulation a workbench allows to simulate both planar and textured front surfaces. Furthermore, such simulations are performed by assuming the same amount of semiconductor material. Its total volume is the sum of the two volume V_{rec}^{text} and V_{pyr}^{text}, which has to be equal to the planar cell volume V_{rec}^{plan}; therefore the height of the textured cell can be obtained as:

$$h_{rec}^{text} = \frac{(V_{rec}^{plan} - V_{pyr}^{text})}{S_{base}}, \tag{127}$$

where S_{base} is the area of a pyramids base, which has a square shape. The workbench, which is based on the one from the Synopsys application note [29], does not compute the generation rate in thin front and back a-Si layers of the device. In order to compute

J_{ph}	$36.8\ mA/cm^2$

Table 17: Photocurrent density in a 300 μm substrate.

the absorption in such layers the Inspect command file has to be modified; a constant optical generation rates can be defined as:

$$G_0 = \frac{\phi_{inc} Abs A}{V}, \tag{128}$$

where ϕ_{inc} is the incident flux, Abs is the aSi layers absorbance, A is the front/back area and V is the volume. Such G_0 is set as the optical generation in the middle of the front a-Si layer, whereas the value G_1 at the top of the aSi layer is obtained by means of linear interpolation between G_0 and G_2:

$$G_1 = 2G_0 - G_2, \tag{129}$$

where G_2 is the generation in the c-Si surface. At the back aSi layer an interpolation is not performed, which is due to the low absorption of such layer, therefore a constant optical generation rate is assumed. The A and B optical profiles, computed by adopting of such settings, are then imported in the elementary cells Fig. 46 and the photogenerated density current is computed as (126). Simulations are performed with and without absorption in the ARC layer. The simulated domain in the raytracer has the size of the basic texturing element and the bulk underneath it, as in Fig. 53; therefore, by means of the spatial repetition of such element the entire cell can be simulated. In case of a regular pattern of pyramids, the minimum simulation domain is a quarter of a pyramid.

At first the raytracer workbench needs to be validated by means of comparison with the TMM results, therefore a planar surface is simulated and the results are reported in Tab. 18; J_{ph} differ of about 1.3% of their values, which is an acceptable mismatch.

ideal ARC	real ARC
$33.47\ mA/cm^2$	$32.89\ mA/cm^2$

Table 18: RT planar simulator results.

Then a textured cell is simulated, in which pyramid geometrical parameter are listed in Tab. 19; the impact of light trapping techniques on the photogenerated current is evaluated and results are shown in Tab. 20.

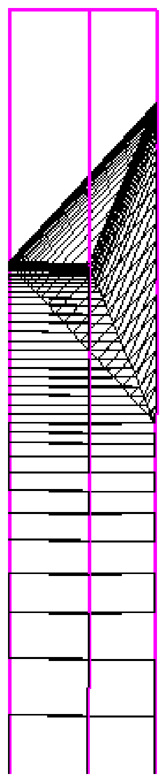

Figure 53: Top part of the basic simulated element in case of textured cell.

Base side	vertex angle	height
10 μm	70.5°	7.07 μm

Table 19: Pyramid dimensions of the simulated texturing into Sentuarus workbench.

ideal ARC	real ARC
37.97 mA/cm^2	36.98 mA/cm^2

Table 20: RT textured simulator results.

Textured solar cells gains almost 5 mA/cm^2, when no losses in the ARC layer are considered, and about 4 mA/cm^2, in case of absorbing ARC, with respect to their planar counterparts. Losses due to ARC absorption are relatively higher compare to planar surface. A comparison with Allen article results it is not possible, due to the fact that a J_{ph} value it is not provided. Nevertheless the resulting J_{sc} in [15] is equal to 34.00 mA/cm^2, such value is certainly higher than that the simulated results, even in case of very low SRV and high quality substrate. Probably only A optical profile, which has aluminum at its back Tab. 16, is imported or if no ARC absorption are considered. Different textured surface has been also tested, such as pyramids with a 5 μm instead of 10 μm; however the resulting J_{ph} is lower and equal to 36.80 mA/cm^2.

Family Tree	Tool	Parameter	1	2
	SDE		--	
		geo	_upright	_planar
		Angolo_al_vertice	70.5	70.5
		base	5	10
		Altezza_cella_NOtextur	150	150
		Spessore_Alluminio	0.5	0.5
		Spessore_BackOxide	0.03	0.03
	SDE		--	--
	SDEVICE		--	--
		specfile	15g_1.2um_equi-10nm.t	g_1.2um_equi-10nm
		nrays	50000	50000
		minintens	1e-3	1e-5
		depthlimit	80000	80000
		Spessore_aSi_Front	0.005	0.005
		Spessore_SiNx	0.070	0.070
		Spessore_SiC	0.030	0.030
		Spessore_aSi_Back	0.025	0.025
		Spessore_aSiINTRINSECO_Back	0.005	0.005
		model	_tmm	_tmm
	SDEVICE		--	--
	INSPECT		--	--
	INSPECT		--	--

Figure 54: Sentuarus workbench parameters for the optical simulation. Both planar and textured cell can be simulated with raytracing method.

6 Electrical simulation

The reference architecture for the electrical simulations performed in this thesis is shown in Fig. 55, which is related to the Lu and co-authors article [16]. Geometrical parameters and doping concentration are defined in Tab. 3 while defects distribution in amorphous silicon is defined in section (4.2).

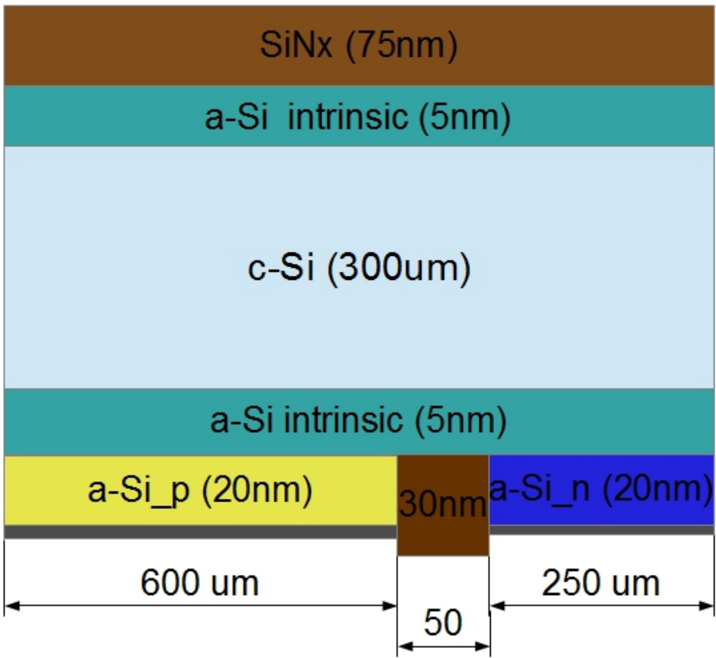

Figure 55: Structure of the reference device for the electrical simulations.

In order to validate physical models adopted for the electrical simulation the simulation results have been compared to those of [16]. After the model validation, simulations have been performed to investigate the sensitivity of performance of IBC-HJ on different physical and geometrical parameters.

6.1 Electrical simulator validation

In [16] the impact of the intrinsic a-Si back layer thickness on the FF has been evaluated. As discussed in (3.4) such layer leads to a potential barrier to the carriers conduction, therefore the J-V characteristic exhibits a s-shape. Simulation are performed under the assumption of ideal surface, in which no recombinations are accounted for. The J-V characteristic is shown in Fig. 56, in which it is highlighted that the fill factor degrade with increasing layer thickness, FF values are reported in Tab. 21. Such J-V curves features a trend similar to that reported by [16].

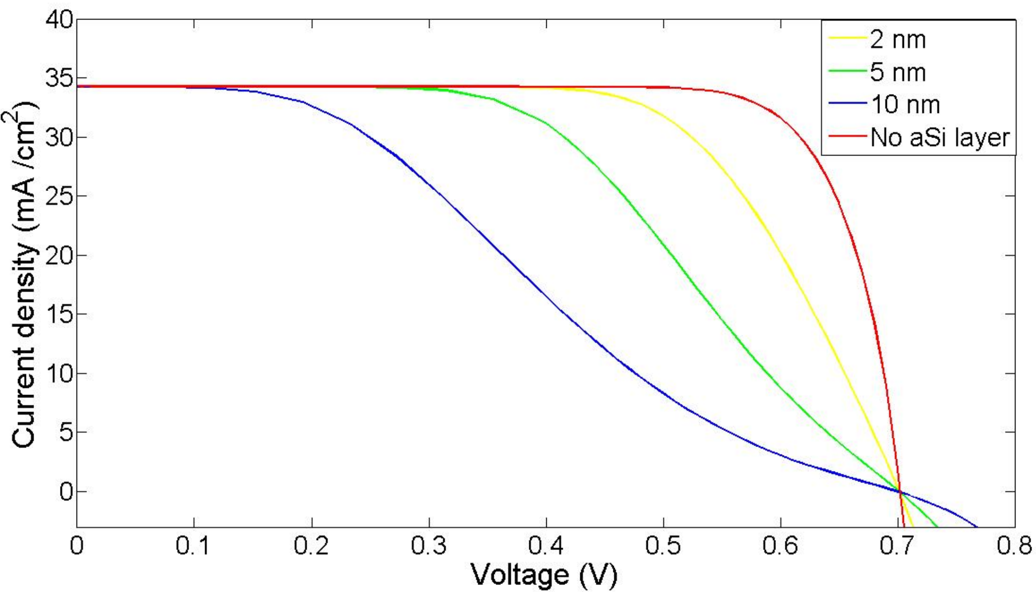

Figure 56: Influence of buffer back layer thickness on FF.

Buffer thickness (nm)	J_{sc} (mA/cm^2)	V_{oc} (mV)	FF (%)	η (%)
10	34.25	700	32.44	7.78
5	34.25	700	51.89	12.46
2	34.25	700	64.14	15.88
No layer	34.25	700	79.19	19.04

Table 21: Variations of figures of merit for different buffer layer thickness when surface recombinations are neglected.

However the interfaces between c-Si and doped a-Si are typically very defective, therefore, the figures of merit reported in Tab. 21 may be not realistic. In fact, the performance of solar cells are very degraded by defects at such interfaces, as discussed in the following. Interface between c-Si and intrinsic a-Si are less defective but still the SRV is not zero. In Tab. 22 the influence of different values of SRV at interface between a-Si and c-Si are reported.

SRV (cm/s)	J_{sc} (mA/cm^2)	V_{oc} (mV)	FF (%)	η (%)
0	34.25	700	51.89	12.46
10	33.50	695	51.77	12.05
100	27.89	656	53.00	9.73

Table 22: Impact of SRV between a-Si and c-Si.

6.2 Efficiency limits analysis

Different solar cells architecture are considered and their maximum achievable performance are compared. In order to estimate the ultimate efficiency, devices with ideal electrical behaviour are simulated. In such simulations physical properties and thickness of the crystalline silicon (c-Si) substrate have been kept constant to maintain the same simulation conditions, moreover only radiative recombinations are accounted for and resistive losses are neglected. No interface defects are considered between c-Si and silicon nitride (SiNx). However, a surface recombinations velocity (SRV) of 10^6 cm/s is assumed at the metal contact, which is constant for each structure. Only planar front surface are accounted for. Furthermore, in order to estimate realistic performance, bulk and surface defects have to be accounted for.

6.2.1 Homogeneous emitter HE solar cell

A solar cell with a crystalline n-type substrate is considered, as in Fig. 57, with thickness 300 μm and front contact pitch 2 mm. The front contact is 50 μm wide. The main figures of merit of an ideal HE solar cell are assumed in Tab. 23. According to the assumptions described previously, the maximum efficiency of the HE cell is 19.87 %. In order to simulate a real photovoltaic device all the recombination mechanisms have to be considered with their proper models, as described in section (4.2.1). A passivating layer at the planar front surface is deposited to reduce the interface defects between c-Si and SiNx. The surface recombination velocity (SRH) is set to $1.812 \cdot 10^5$ cm/s. Practical device performance are reported in Tab. 23.

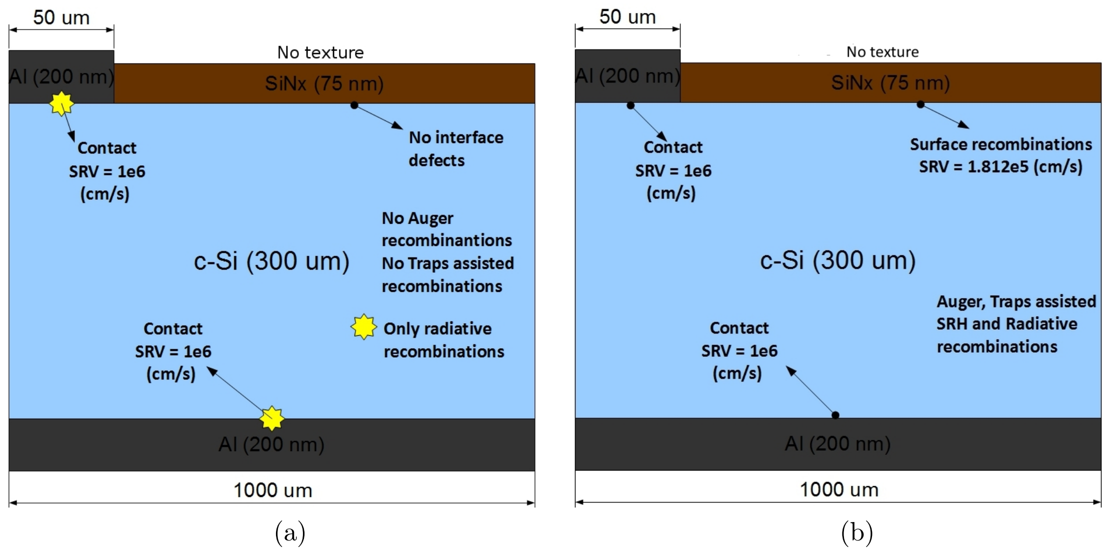

Figure 57: Real and ideal HE solar cell in which considered and neglected loss mechanisms are highlighted.

	J_{ph} (mA/cm^2)	J_{sc} (mA/cm^2)	V_{oc} (mV)	FF (%)	η (%)
Ideal HE	35.68	35.49	673	83.21	19.87
Real HE	35.68	34.08	628	82.13	17.57

Table 23: Performance of homogeneous emitter solar cells.

6.2.2 Heterojunction with intrinsic thin layer HIT solar cell

In a HIT solar cell, differently from the previously described HE cell, doping diffusions are replaced by depositions of thin doped amorphous silicon layer, as shown in Fig. 58. The front p-type layer is the emitter and the back n-type layer is the base. In order to compare the performance upper bound limits by assuming the similar conditions, defects are neglected in a-Si. Mobility for electrons and holes is considered much greater than one, in order to not limit the carriers transport. In Tab. 24 the ideal performance are reported. The maximum achievable efficiency of the HIT solar cells improves with respect to that of HE; such improvement is mainly due to passivating effects of a-Si layers. In order to simulate a practical electrical behaviour, the defects within a-Si have to be considered, as in section (4.2.1). The interfaces between c-Si and doped a-Si are highly defective, therefore in practical device a passivating layer of intrinsic a-Si is necessary. In order to reach relatively high efficiency an optimization of geometrical and physical parameters is necessary. Such optimization in this thesis is not performed, hence in Tab. 24 literature [33] results are reported.

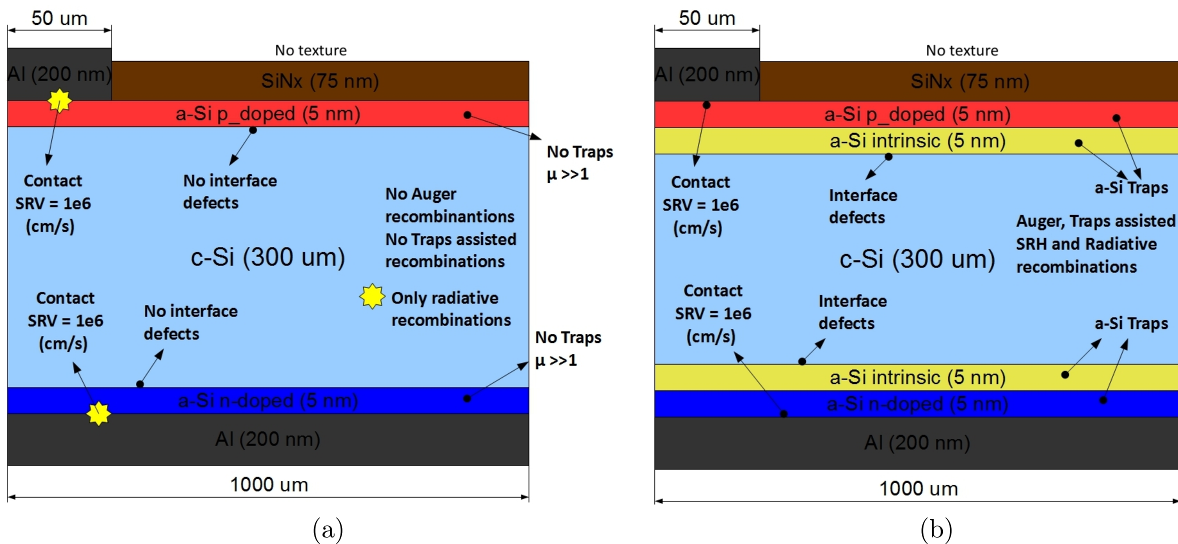

Figure 58: Real and ideal HIT solar cell in which considered and neglected loss mechanisms are highlighted.

	J_{ph} (mA/cm^2)	J_{sc} (mA/cm^2)	V_{oc} (mV)	FF $(\%)$	η $(\%)$
Ideal HIT	35.04	35.02	726	87.02	22.12
Real HIT		34.70	662	74.60	17.10

Table 24: Performance of HIT solar cell.

6.2.3 Interdigitated back contact hetero-junction IBC-HJ solar cell

The vertical cross section of all back contact architecture IBC-HJ is shown in Fig. 59. In order to estimate the maximum achievable performance the structure is simulated under the same assumption of the solar cells previously described, which allows a fair comparation of the different technologies. The resulting 23.37 %, Tab. 25, efficiency is higher than the others, which is due to higher photons absorption caused by the absence of shadowing effect. The efficiency of a practical solar cell has to be evaluated under realistic conditions (Fig. 59b). The study of the performance sensitivity to different geometrical and physical parameters is a goal of this thesis and it is discussed in the following subsection.

	J_{ph} (mA/cm^2)	J_{sc} (mA/cm^2)	V_{oc} (mV)	FF $(\%)$	η $(\%)$
Ideal IBC-HJ	37.60	37.12	726	86.69	23.37
Real IBC-HJ	36.80	34.58	704	81.72	19.34

Table 25: Performance of interdigitated back contact hetero-junction devices.

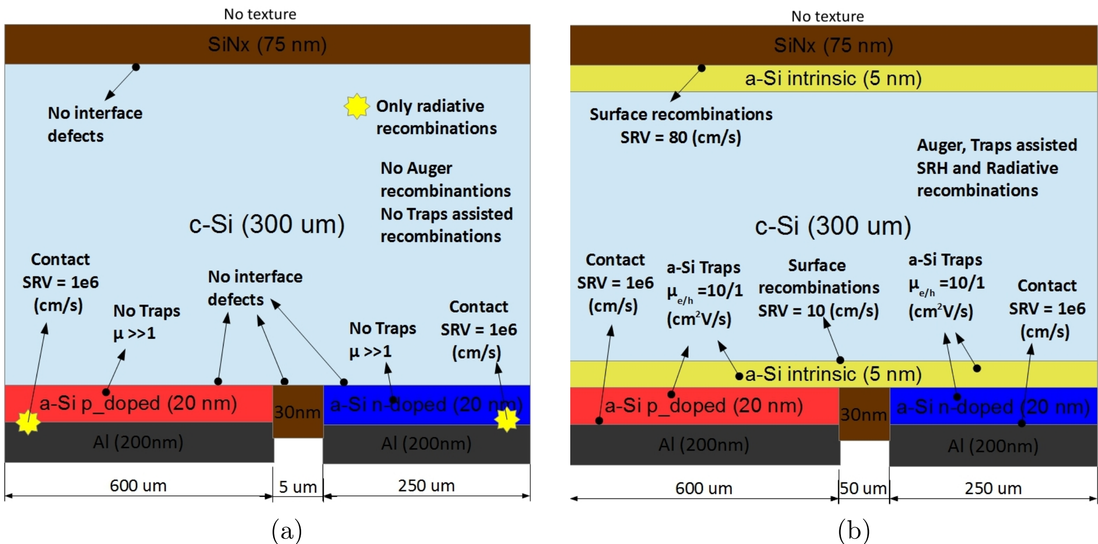

(a) (b)

Figure 59: Real and ideal IBC-HJ solar cell in which considered and neglected loss mechanisms are highlighted.

6.3 Impact of the back buffer layer on cell performance

As already discussed, intrinsic passivating a-Si layers are necessary in order to reduced the defectivity of interfaces between c-Si and doped a-Si. In IBC-HJ solar cells, the back buffer layer affects the carriers conduction, hence such effect cannot be neglected. As discussed in the section (3.4), the intrinsic a-Si layer leads to a potential barrier for holes. In order to evaluate such effects, a set of simulation is performed by changing the buffer layer thickness with carrier mobility and bandgap are considered as simulation parameters. As reference structure, the one without the intrinsic back buffer layer is considered, as in Fig. 60, in which the SRV value between c-Si and doped a-Si is set to 10000 cm/s. The other surface recombination velocities adopted in these simulations are listed in Tab. 26 and the c-Si effective lifetime is assumed to be $\tau = 0.6\ ms$.

SRV a-Si/SiNx	SRV c-Si/a-Si	SRV metal contacts
80 (cm/s)	10 (cm/s)	10^6 (cm/s)

Table 26: SRV setting of the simulation.

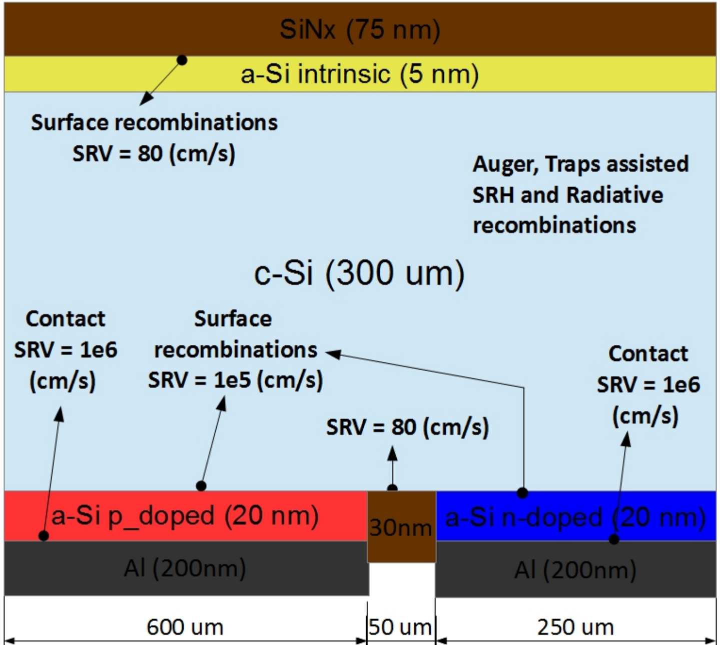

Figure 60: IBC-HJ without back buffer layer.

The performance of a IBC-HJ cell without back buffer layer are reported in Tab. 27. The buffer back layer leads to: i) an improved surface passivation and ii) a barrier for

J_{sc} (mA/cm^2)	V_{oc} (mV)	FF (%)	η (%)
32.89	668	80.85	17.77

Table 27: Performance of interdigitated back contact hetero-junction without a-Si back buffer layer.

holes at the emitter; such competitive effects have to be accounted for.

The first set of simulations is performed under the conditions of a typical a-Si bandgap width of 1.72 eV and a very low carrier mobility. Such mobility is independent on the doping concentration and its value is equal to 1 cm^2/Vs for electrons and 0.1 cm^2/Vs for holes. Cell performance are reported in Tab. 28, the presence of the buffer layer is detrimental, as results from Fig. 61.

As already discussed, the FF (shown in Fig. 61) decreases with increasing buffer thickness, therefore it is always lower than that of the case without buffer layer. In such figure, we observed that also η decreases as the thickness increases and it is smaller compared to the case with no buffer. The degradation of the FF value is illustrated in Fig. 62.

Buffer thickness (nm)	J_{sc} (mA/cm^2)	V_{oc} (mV)	FF (%)	η (%)
2	33.50	696	73.06	17.03
5	33.50	696	61.15	14.26
8	33.49	696	49.80	11.61
11	33.47	696	38.78	9.02
14	33.46	696	28.91	6.73

Table 28: Solar cell performance ($E_g = 1.72$ eV and $\mu_{e/h} = 1/0.1$ cm^2/Vs in the back buffer layer).

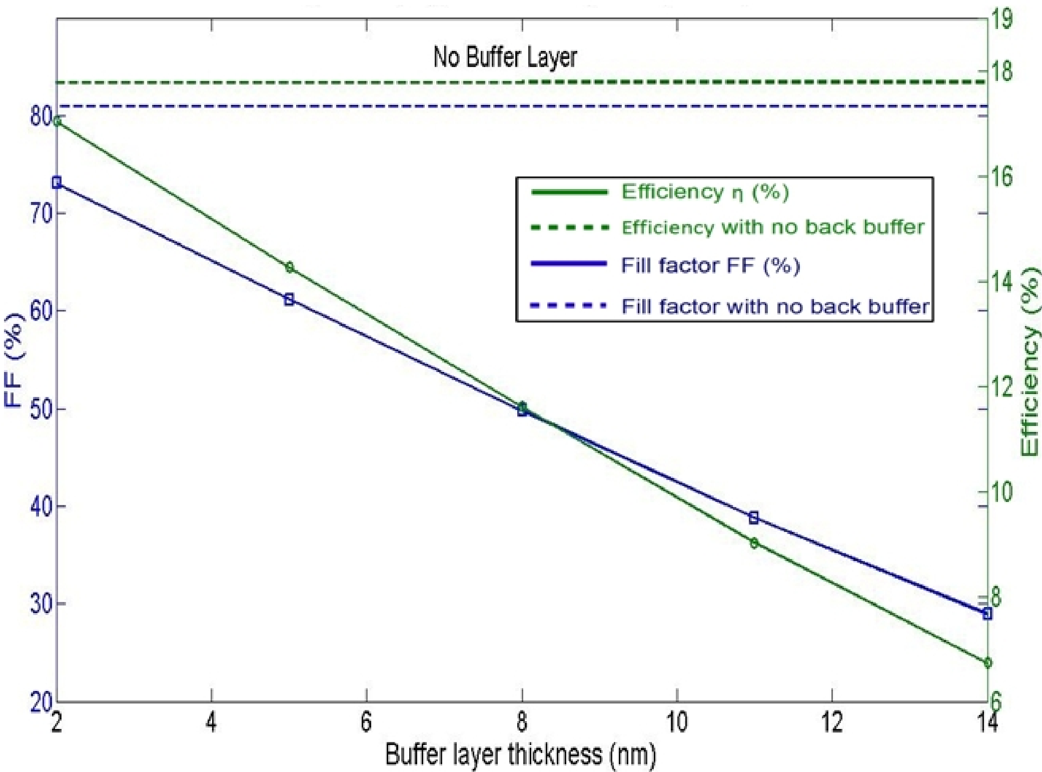

Figure 61: Efficiency and FF versus buffer layer thickness (buffer layer with $E_g = 1.72$ eV and $\mu_{e/h} = 1/0.1$ cm^2/Vs).

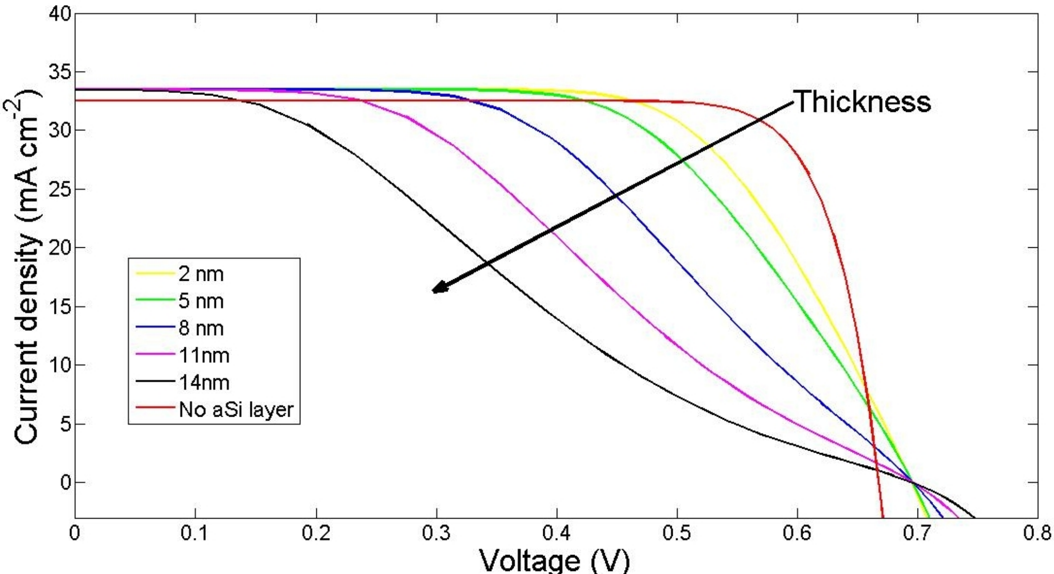

Figure 62: J-V characteristics calculated for different buffer layer thickness (buffer layer with $E_g = 1.72\ eV$ and $\mu_{e/h} = 1/0.1\ cm^2/Vs$).

A second set of simulation is performed under the realistic assumption that the carriers mobility within the intrinsic a-Si layers is higher with respect to that in doped a-Si layers. Such mobilities are set, as in [27] and [31], to 10 cm^2/Vs for electrons and to 1 cm^2/Vs for holes. Under these conditions, as we can observed from Tab. 29 and Fig. 63, a thin a-Si buffer layer can improve the solar cell efficiency if its maximum thickness is around 5 nm. In addiction, an higher mobility leads to a less degraded FF.

Buffer thickness (nm)	J_{sc} (mA/cm^2)	V_{oc} (mV)	FF (%)	η (%)
2	33.53	696	78.6	18.34
5	33.52	696	77.18	18.01
8	33.52	696	74.63	17.42
11	33.5	696	70.75	16.50
14	33.5	696	65.53	15.28

Table 29: Solar cell performance in case of back buffer layer featuring $E_g = 1.72\ eV$ and $\mu_{e/h} = 10/1\ cm^2/Vs$.

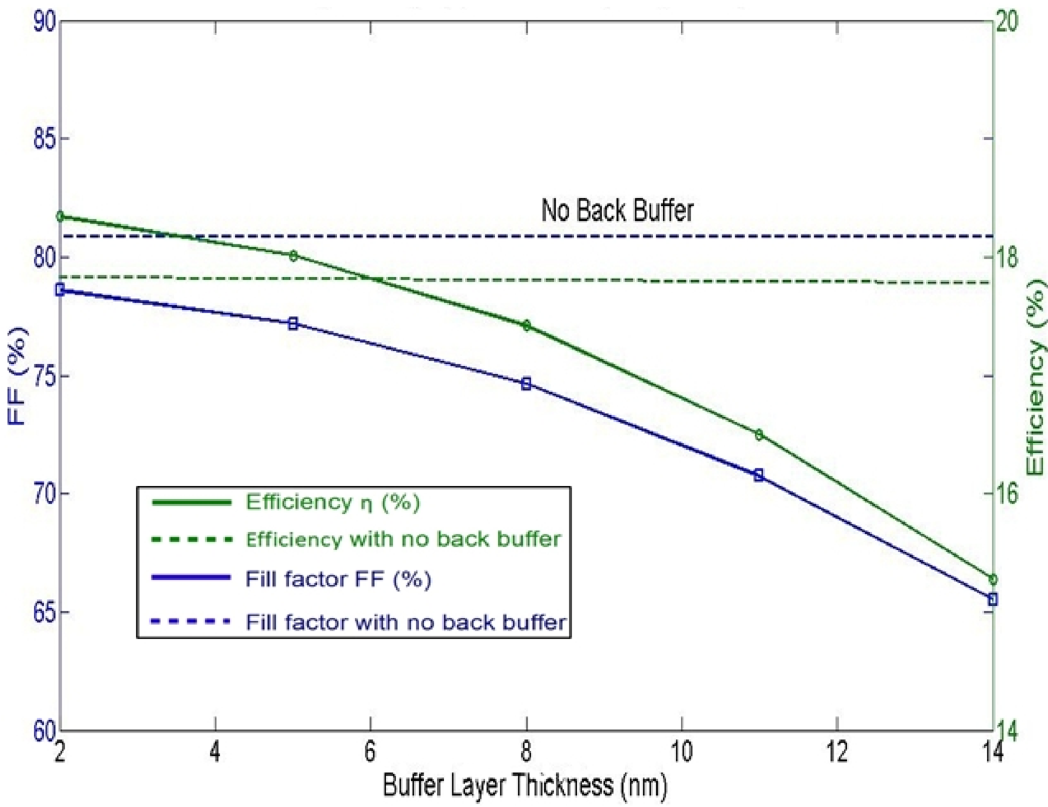

Figure 63: η and FF as function of the layer thickness (buffer layer with $E_g = 1.72\ eV$ and $\mu_{e/h} = 10/1\ cm^2/Vs$).

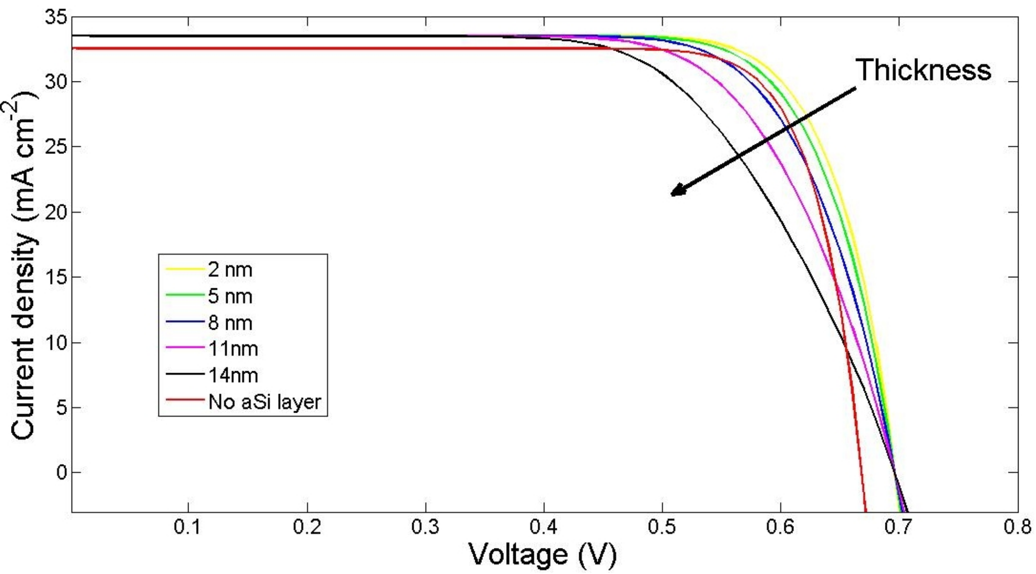

Figure 64: JV characteristic with buffer thickness as parameter (buffer layer with $E_g = 1.72\ eV$ and $\mu_{e/h} = 10/1\ Vcm^2/s$).

In order to decrease the potential barrier for holes, it is possible to reduce the bandgap width by means of modifications to the fabrication process as discussed in (3.5.3). As reported by [15] the minimum E_g value for a proper passivation effect is 1.65 eV, therefore a set of simulations is performed with such bandgap width. The carrier mobility in a-Si is defined as 1 cm^2/Vs for electrons and as 0.1 cm^2/Vs for holes. Under these conditions, the cell performance are further improved, as shown in Tab. 30, and the buffer layer leads to enhancement efficiency with respect to the case of the absence of buffer if its thickness is below 8 nm, as shown in Fig. 65. The corresponding JV characteristic in Fig. 66 exhibits a less marked s-shape.

Buffer thickness (nm)	J_{sc} (mA/cm^2)	V_{oc} (mV)	FF (%)	η (%)
2	33.50	696	78.90	18.39
5	33.50	696	78.00	18.18
8	33.50	696	76.44	17.82
11	33.48	696	74.05	17.25
14	33.48	696	70.54	16.44

Table 30: Solar cell performance in the case of $E_g = 1.65$ eV and $\mu_{e/h} = 1/0.1$ cm^2/Vs in the back buffer layer.

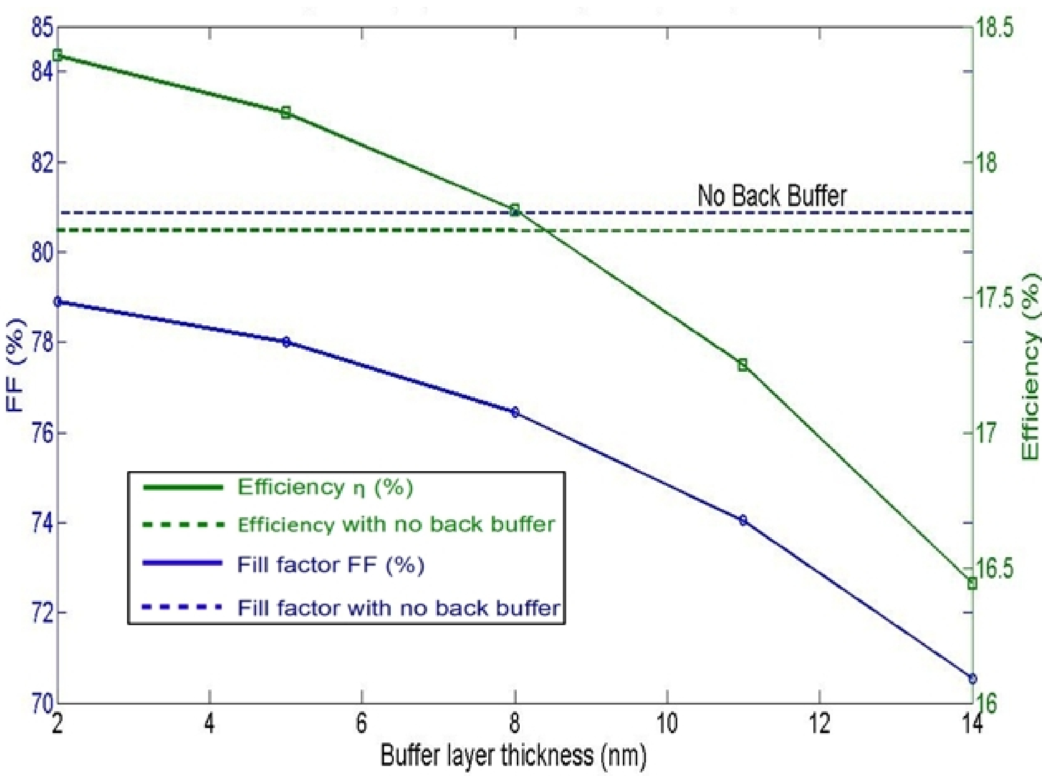

Figure 65: η and FF as function of the layer thickness (buffer layer with $E_g = 1.65$ eV and $\mu_{e/h} = 1/0.1$ cm^2/Vs).

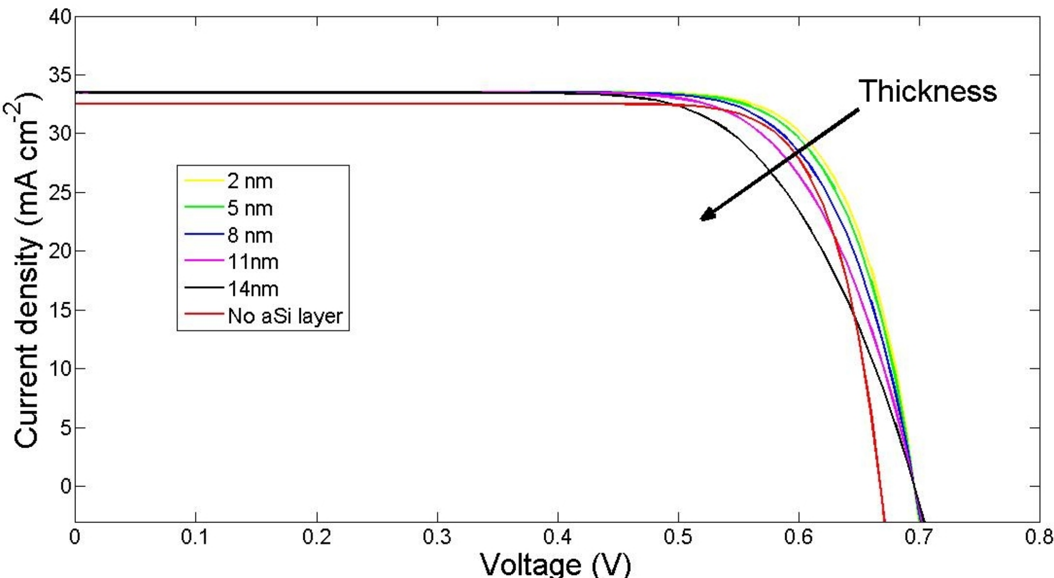

Figure 66: JV trend with increasing thickness (buffer layer with $E_g = 1.65\ eV$ and $\mu_{e/h} = 1/0.1\ cm^2/Vs$).

Lastly a set of simulations is performed with a bandgap width of 1.65 eV and with the carriers mobility defined as 10 cm^2/Vs for electrons and as 1 cm^2/Vs for holes. Under such conditions, the FF slightly decreases with increasing thickness, therefore the efficiency is higher compared to those of the previous simulations, as shown in Tab. 31. Furthermore, the performance improvement is no more dependent on the buffer thickness because, as shown in Fig. 67, even relatively thick substrate leads to an increase of η. A buffer layer, under those assumptions, is no longer a significant obstacle to the carriers transport, therefore the s-shape is not marked in the JV characteristic in Fig. 68.

Buffer thickness (nm)	J_{sc} (mA/cm^2)	V_{oc} (mV)	FF (%)	η (%)
2	33.53	696	79.25	18.49
5	33.52	696	79.18	18.47
8	33.52	696	79.02	18.44
11	33.50	696	78.78	18.37
14	33.50	696	78.43	18.28

Table 31: Solar cell performance in the case of the back buffer layer exhibits ($E_g = 1.65\ eV$ and $\mu_{e/h} = 10/1\ cm^2/Vs$).

The efficiency is higher in case of a particularly thin back buffer layer, below 2 nm. In this work, it is assumed that the minimal layer thickness possible for a practical process is 5 nm, therefore such value is adopted in the following.

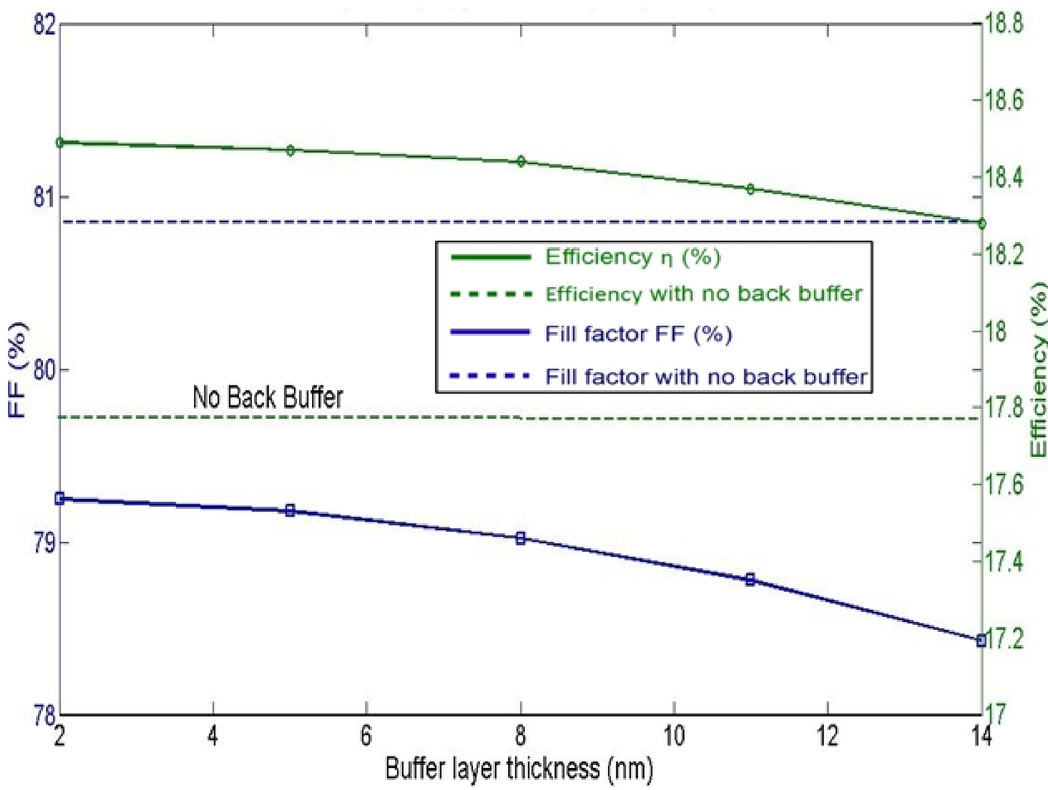

Figure 67: η and FF as function of the layer thickness (buffer layer with $E_g = 1.65\ eV$ and $\mu_{e/h} = 10/1\ cm^2/Vs$).

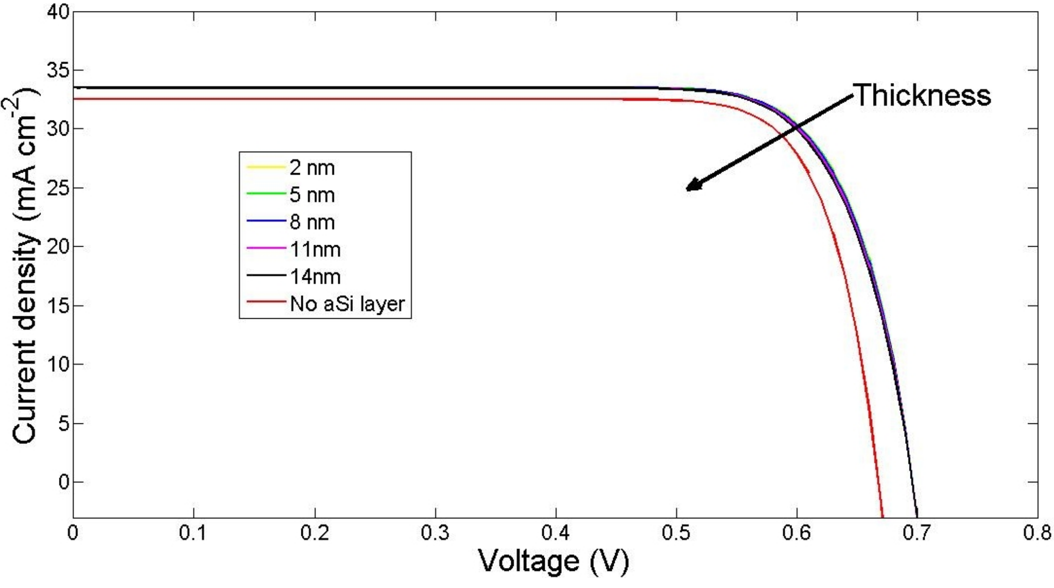

Figure 68: JV trend with increasing thickness (buffer layer with $E_g = 1.65\ eV$ and $\mu_{e/h} = 10/1\ cm^2/Vs$).

6.4 Sensitivity on substrate resistivity

As discussed in (3.7) a high quality c-Si substrate is necessary to reduce the recombination losses. However, the physical properties of the substrate are linked together, in fact resistivity and carriers lifetime are doping dependent. The relationship between substrate resistivity and carriers lifetime, in case of a high quality n-type FZ substrate, is considered as in [23].

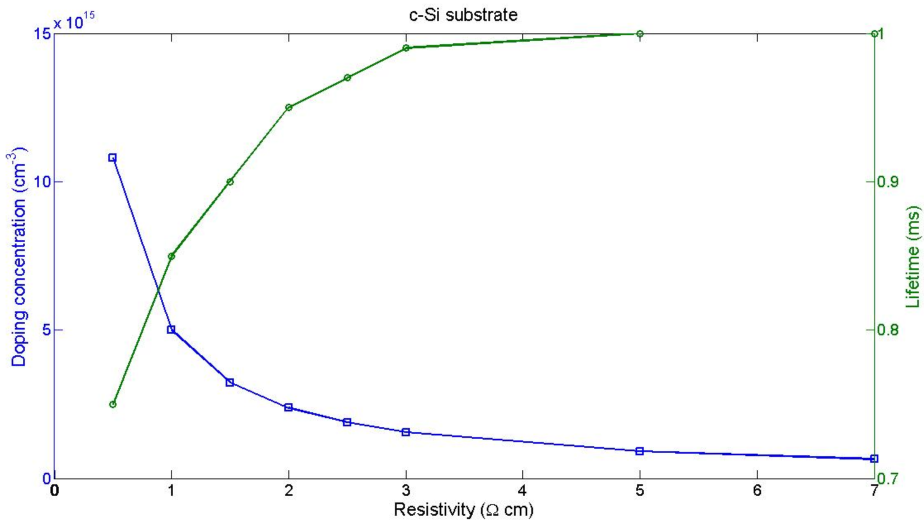

Figure 69: Relationship between c-Si substrate resistivity, doping concentration and carrier lifetime.

A set of simulation is performed in order to estimate the sensitivity of cell performance to different bulk resistivities ρ_{c-Si}, which is varied within the range $0.5 - 10\ \Omega \cdot cm$.

ρ_{c-Si} $(\Omega \cdot cm)$	J_{sc} (mA/cm^2)	V_{oc} (mV)	FF (%)	η (%)
0.5	32.51	702	83.34	19.01
0.75	33.22	703	82.38	19.22
1	33.60	704	81.72	19.34
1.5	34.01	705	80.67	19.35
2	34.28	707	79.97	19.37
2.5	34.44	707	79.50	19.37
3	34.58	708	79.14	19.38
5	34.88	709	78.23	19.35
7	35.06	709	77.74	19.34
10	35.23	709	77.31	19.32

Table 32: IBC-HJ performance with different substrate resistivities.

The results highlights two competitive effects occurring, as ρ_{c-Si} increases: i) J_{sc} increases (as shown in Fig. 70) and ii) FF decreases (as shown in Fig. 71). The fill factor is directly related to the bulk resistivity, whereas short circuit current increases as

the doping concentration decreases because the Auger recombinations is consequently reduced. However, the impact of ρ_{c-Si} on V_{oc} is negligible.

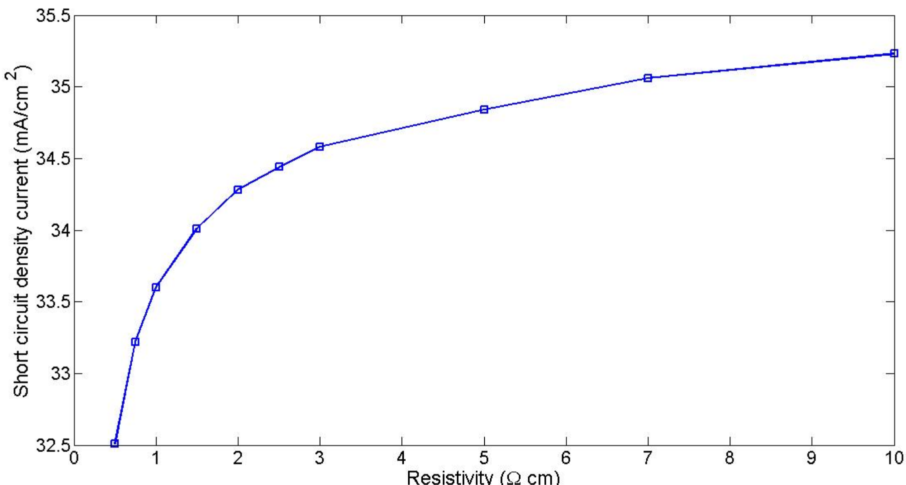

Figure 70: Sensitivity of J_{sc} to c-Si substrate resistivity.

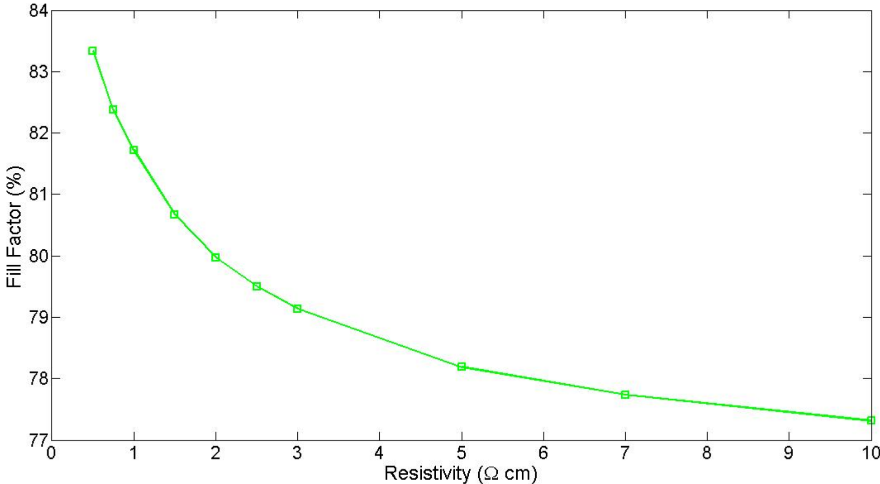

Figure 71: Sensitivity of FF to c-Si substrate resistivity.

Overall the efficiency of IBC-HJ exhibits a small sensitivity to the ρ_{c-Si}, as shown in Fig. 72, the peak value is reach at $\rho_{c-Si} = 3\ \Omega \cdot cm$.

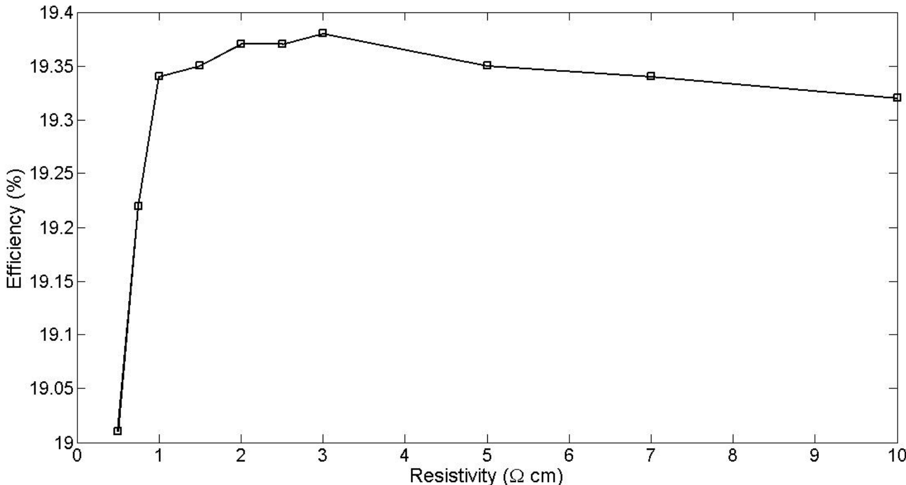

Figure 72: Sensitivity of the IBC-HJ efficiency to c-Si substrate resistivity.

6.5 Sensitivity to geometrical gap value

The last set of simulations is aimed at understanding the sensitivity of the gap width to the cell performance. The geometrical gap between the contacts affects the length of the path which carriers have to follow to be collected by the contacts. In order to perform such simulations, a c-Si substrate with a $3\ \Omega \cdot cm$ resistivity is considered and the gap length is varied within the range of $50 - 200\ \mu m$, in which the back contact pitch is kept constant. In case of a high quality FZ substrate the results are reported in Tab. 33, therefore as the gap increases the performance are slightly degraded.

Gap length (μm)	J_{sc} (mA/cm^2)	V_{oc} (mV)	FF (%)	η (%)
50	34.58	708	79.14	19.38
100	34.45	708	79.08	19.28
150	34.33	707	79.04	19.19
200	34.17	707	78.98	19.08

Table 33: Solar cell performance with different values of gap length.

The sensitivity of the short circuit current density to the geometrical gap width is shown in Fig. 73, in which simulations are performed with different ρ_{c-Si}: i) $\rho_{c-Si} = 3\ \Omega \cdot cm$, ii) $\rho_{c-Si} = 0.5\ \Omega \cdot cm$ and iii) $\rho_{c-Si} = 10\ \Omega \cdot cm$. The resulting trend is similar, however in case of smaller ρ_{c-Si} the J_{sc} is lower due to a minor minority carriers lifetime.

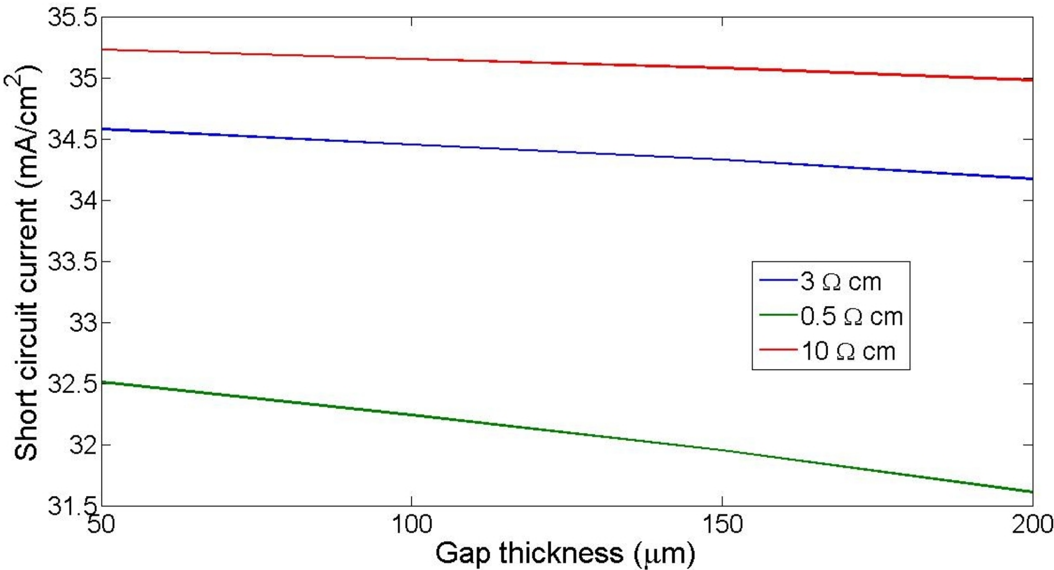

Figure 73: Sensitivity of J_{sc} on the gap length for different c-Si substrate.

Both FF and V_{oc} are not significantly affected by geometrical gap width. The efficiency (η) trends are shown in Fig. 74. As results from the previous subsection, the substrate with the $\rho_{c-Si} = 3\ \Omega \cdot cm$ exhibits the higher efficiency, feature which is valid also with wider gap. Substrate with $\rho_{c-Si} = 10\ \Omega \cdot cm$ shown a less marked degradation, which is due to a higher J_{sc}.

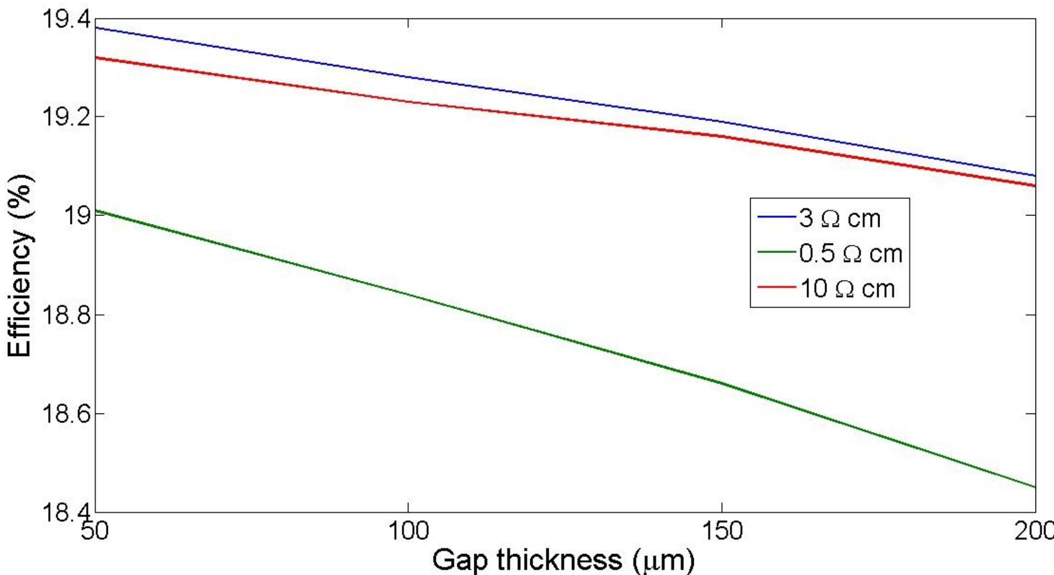

Figure 74: Sensitivity of η to the geometrical gap width for different c-Si substrate.

Conclusions

Photovoltaic research aimed at investigating novel solar cell high efficiency architectures, which can be manufactured by means of low-cost processes. Interdigitated back contact hetero-junction (IBC-HJ) solar cells are one of the most promising devices towards the reduction of the cost-per-watt, therefore many efforts have been made to optimize its performance and its fabrication process.

Such devices, featuring all-back contacts, exhibit an enhanced photogenerated current due to the absence of shadowing effects of front contacts. In addiction the hetero-junction leads to an improved surface passivation. In IBC-HJ non-crystalline materials, as amorphous silicon, are deposited on the surfaces, requiring a far less expensive process compared to the doping diffusions, in the case of conventional crystalline silicon solar cells.

On the other hand, several critical aspects and drawbacks are associated to IBC-HJ, one goal of this thesis is to highlight them by means of numerical simulations. In particular, the additional deposition of an intrinsic amorphous silicon layer between the crystalline and the doped amorphous silicon, which is necessary to attain at a good surface passivation, affects the solar cell performance. In fact, it leads to the formation of potential barriers at the contacts, which is particularly detrimental to the minority carriers transport at the emitter contact. Such effect causes an output J-V characteristic featuring a s-shape, leading a markedly low fill factor.

In order to simulate an illuminated solar cell the optical generation rate map has to be collected. The transfer matrix method has been adopted to successfully solve the optical part in different structures with a planar front surface, accounted for anti reflective coating layers. Solar cells with textured front surface have been, also, simulated by means of the raytracing method. Texturing leads to an enhanced photon absorption and, therefore, to a higher photogenerated current.

The physical models have been set-up and validated by means of comparison with literature results. The simulation flow has been adopted to calculate the achievable efficiency of IBC-HJ solar cells, in which only optical losses and surface recombination velocities at metal contacts are accounted for. IBC-HJ exhibits potentially higher efficiency compared to other considered architectures, including the conventional cell and a HIT solar cell. In order to understand the critical aspects of practical devices different sets of simulation have been performed. The impact of the intrinsic back amorphous silicon layer

on cell performance have been investigated. The presence of a buffer layer leads to two competitive effects: i) an improved surface passivation and ii) a degraded minority carriers conduction at the emitter. The simulation results show that the potential barrier can be decreased by reducing the energy bandgap width or by improving the mobility for holes in such layer.

Since high quality c-Si substrates are required in the case of IBC solar cells, practical devices are fabricated on FZ n-type wafers. The influence of bulk resistivity on performance has been analyzed; as the resistivity increases: i) the doping concentration decreases and ii) the carriers lifetime increases. Such variations lead to two competitive effects, that are a degradation of the fill factor and an increased short circuit density current, therefore an optimum configuration can be calculated. However, the sensitivity of efficiency to bulk resistivity is not marked.

Lastly the sensitivity of the main figures of merit to the geometrical gap between contacts has been analyzed. In order to perform such analysis the chosen substrate resistivity is that which maximize the efficiency. A wider geometrical gap do not lead to a strong performance degradation, therefore such fabrication parameter does not markedly affect the IBC-HJ efficiency.

Overall interdigitated back contact hetero-junction have been confirmed to be a promising architecture in order to achieve relatively high efficiency by means of low-cost fabrication processes. A wide range of physical parameters affect the performance of these solar cells and an optimization is necessary in order to maximize efficiency. Such parameters are mainly related to the minority carriers mobility and to the defectiveness of the intrinsic amorphous silicon back buffer layer.

List of Figures

1 Sun regions (from wikipedia). 15
2 Solar power balance through the atmosphere (from wikipedia). 16
3 Solar spectrum compared to black body spectrum (from wikipedia). . . . 17
4 Effect of the atmosphere on the solar spectrum [3]. 18
5 Calculation of the air mass coefficient [3]. 19
6 Periodic table of the elements [5]. 21
7 sp^3 type hybridation (from wikipedia). 21
8 Band structure of metals, insulators and semiconductors (from wikipedia). 23
9 Fermi statistic (from wikipedia). 24
10 Doped silicon structure [3]. 25
11 Comparison between density of states DOS (from wikipedia). 25
12 Real and complex part of the silicon refractive index [3]. 27
13 Incident and transmitted ray at an interface [3]. 27
14 Comparison between absorption coefficient of various materials [3]. 29
15 Dispersion relationship of silicon crystal lattice [1]. 30
16 Comparison between direct and indirect band gap structure [1]. 31
17 Elemental volume for deriving the continuity equation [1]. 36
18 Structure of a pn junction with depleted and quasi-neutrals region[8]. . . 37
19 Solar cell equilibrium conditions: (a) energy bands, (b) electric field and (c) charge density [8]. 40
20 Architecture of a typical solar cell [3]. 43
21 I-V characteristic under dark and illuminated conditions [1]. 44
22 Two diode solar cell model [8]. 45
23 Typical reflectance, external and internal quantum efficiency characteristic (from wikipedia). 47
24 Short circuit density current trend compared to the bandgap [3]. 48
25 Solar cell efficiency limit as function of the semiconductor bandgap [1]. . 49
26 Standard solar cell schematic [1]. 50
27 Two diode model including the parasitic resistances [8]. 51
28 Variations of the output characteristic with different value of (a) R_S (b) R_{SH} [1]. 52
29 Periodic (A) and random (B) pyramids three-dimensional scheme [4]. . . 54
30 Summary of the technological options for surface recombination reduction [3]. 55
31 Cross section of a homojunction IBC solar cell [10]. 56
32 Schematic of a heterojunction with intrinsic layer solar cell [13]. 57

33 Cross section of an interdigitated back contact hetero-junction solar cell [15]. 59
34 Bottom view of an IBC-HJ solar cell [17]. 60
35 Sensitivity of J_{sc} to the n-contact length, where both simulated (circle) and experimental (square) results are reported [16]. The total device length is kept constant. 63
36 Illuminated J-V curves for IBC-HJ solar cells with and without back surface buffer [16]. 64
37 Equilibrium band aligment for hetero junction p-contact [16]. 65
38 Bias and unbias band aligment for hetero-junction p-contact and n-contact [16]. 65
39 Experimental J-V curves with buffer layer, intrinsic and doped [16]. 66
40 Equilibrium band structure and experimental JV characteristic with a-Si buffer layer thickness as parameter [16]. 67
41 Simulated J-V curves with a 8 nm-thick buffer layer with variable E_g [15]. 68
42 FF trends versus intrinsic a-Si layer bandgap E_g. Three different thicknesses are simulated [15]. 68
43 Impact of c-Si resistivity on the main figures of merit [23]. 70
44 Simulation tools flow in Sentaurus [25]. 71
45 Design example of a MOS architecture, in which mesh and doping profile are defined [25]. 72
46 Element of symmetry if the simulated structure. 73
47 Traps distribution in p-type doped a-Si. 76
48 Incident ray splits into reflected and transmitted rays at an interface [25]. 79
49 Integrating horizontal slices to extract 1D optical generation profiles [28]. 80
50 Complex refraction indexes of ARC layers [17]. 81
51 Different cross sections assumed in the optical simulation. 83
52 Optical generation profile in the 2D IBC-HJ architecture. 84
53 Top part of the basic simulated element in case of textured cell. 87
54 Sentuarus workbench parameters for the optical simulation. Both planar and textured cell can be simulated with raytracing method. 88
55 Structure of the reference device for the electrical simulations. 89
56 Influence of buffer back layer thickness on FF. 90
57 Real and ideal HE solar cell in which considered and neglected loss mechanisms are highlighted. 92
58 Real and ideal HIT solar cell in which considered and neglected loss mechanisms are highlighted. 93
59 Real and ideal IBC-HJ solar cell in which considered and neglected loss mechanisms are highlighted. 94

60 IBC-HJ without back buffer layer. 95
61 Efficiency and FF versus buffer layer thickness (buffer layer with $E_g = 1.72\ eV$ and $\mu_{e/h} = 1/0.1\ cm^2/Vs$). 96
62 J-V characteristics calculated for different buffer layer thickness (buffer layer with $E_g = 1.72\ eV$ and $\mu_{e/h} = 1/0.1\ cm^2/Vs$). 97
63 η and FF as function of the layer thickness (buffer layer with $E_g = 1.72\ eV$ and $\mu_{e/h} = 10/1\ cm^2/Vs$). 98
64 JV characteristic with buffer thickness as parameter (buffer layer with $E_g = 1.72\ eV$ and $\mu_{e/h} = 10/1\ Vcm^2/s$). 98
65 η and FF as function of the layer thickness (buffer layer with $E_g = 1.65\ eV$ and $\mu_{e/h} = 1/0.1\ cm^2/Vs$). 99
66 JV trend with increasing thickness (buffer layer with $E_g = 1.65\ eV$ and $\mu_{e/h} = 1/0.1\ cm^2/Vs$). 100
67 η and FF as function of the layer thickness (buffer layer with $E_g = 1.65\ eV$ and $\mu_{e/h} = 10/1\ cm^2/Vs$). 101
68 JV trend with increasing thickness (buffer layer with $E_g = 1.65\ eV$ and $\mu_{e/h} = 10/1\ cm^2/Vs$). 101
69 Relationship between c-Si substrate resistivity, doping concentration and carrier lifetime. 102
70 Sensitivity of J_{sc} to c-Si substrate resistivity. 103
71 Sensitivity of FF to c-Si substrate resistivity. 103
72 Sensitivity of the IBC-HJ efficiency to c-Si substrate resistivity. 104
73 Sensitivity of J_{sc} on the gap length for different c-Si substrate. 105
74 Sensitivity of η to the geometrical gap width for different c-Si substrate. . 105

References

[1] M. A. GREEN. **Solar Cells: Operating Principles Technology (The Red Book)**. UNSW Photovoltaics., 1996.

[2] M. A. GREEN. **Silicon Solar Cells: Advanced Principles and Practice (The Green Book)**. UNSW Photovoltaics, 1995.

[3] PVEEDUCATION, *www.pveducation.org.*

[4] M. ZANUCCOLI. **PhD thesis**, ARCES, University of Bologna, 2012.

[5] ELEMENTSDATABASE, *http://www.elementsdatabase.com/*

[6] ASTM INTERNATIONAL, *http://www.astm.org/DATABASE.CART/HISTORICAL/G173-03.htm*

[7] REFRACTIVE INDEX, *http://refractiveindex.info/.*

[8] A. LUQUE AND S. HEGEDUS **Handbook of Photovoltaic Science and Engineering**. John Wiley EEE Sons, Inc., 2003.

[9] D. REDFIELD **Multiple-pass thin-film silicon solar cell**. Appl. Phys. Lett., 25:647649, 1974.

[10] J. RENSHAW AND A. ROHATGI **Device optimization for screen printed interdigitated back contact solar cells**. Photovoltaic Specialists Conference (PVSC), 2011 37th IEEE , vol., no., pp.002924-002927, 19-24 June 2011

[11] F.J. CASTANO, D. MORECROFT, M. CASCANT, H. YUSTE, M.W.P.E. LAMERS, A.A. MEWE, I.G. ROMIJIN, E.E. BENDE, Y. KOMATSU, A.W. WEEBER AND I. CESAR **Industrially feasible > 19% efficiency IBC cells for pilot line processing**. Photovoltaic Specialists Conference (PVSC), 2011 37th IEEE , vol., no., pp.001038-001042, 19-24 June 2011

[12] M. ALEMAN, J. DAS, T. JANSSENS, B. PAWLAK, N. POSTHUMA, J. ROBBELEIN, S. SINGH, K. BAERT, J. POORTMANS, J. FERNANDEZ, K. YOSHIKAWA AND P.J. VERLINDEN **Development and Integration of a High Efficiency Baseline Leading to 23% IBC Cells**. Energy Procedia, Volume 27, 2012

[13] D. FUJISHIMA, H. INOUE, Y. TSUNOMURA, T. ASAUMI, S. TAIRA, T. KINOSHITA, M. TAGUCHI, H. SAKATA AND E. MARUYAMA **High-performance HIT solar cells for thinner silicon wafers**. Photovoltaic Spe-

cialists Conference (PVSC), 2010 35th IEEE , vol., no., pp.003137-003140, 20-25 June 2010

[14] C. BALLIF, L. BARRAUD, A. DESCOEUDRES, Z.C. HOLMAN, S. MOREL AND S. DE WOLF **A-Si:H/c-Si heterojunctions: a future mainstream technology for high-efficiency crystalline silicon solar cells?**. Photovoltaic Specialists Conference (PVSC), 2012 38th IEEE , vol., no., pp.001705-001709, 3-8 June 2012

[15] J. ALLEN, B. SHU, L. ZHANG, U. DAS AND S. HEGEDUS **Interdigitated back contact silicon hetero-junction solar cells: The effect of doped layer defect levels and rear surface i-layer band gap on fill factor using two-dimensional simulations**. Photovoltaic Specialists Conference (PVSC), 2011 37th IEEE , vol., no., pp.002545-002549, 19-24 June 2011

[16] M. LU U. DAS, S. BOWDEN, S. HEGEDUS AND R. BIRKMIRE **Optimization of interdigitated back contact silicon heterojunction solar cells: tailoring hetero-interface band structures while maintaning surface passivation**. Prog. in Photovoltaics 19, 326, 2011

[17] B. SHU, U. DAS, J. APPEL, B. MCCANDLESS, S. HEGEDUS AND R. BIRKMIRE **Alternative approaches for low temperature front surface passivation of interdigitated back contact silicon heterojunction solar cell**. Photovoltaic Specialists Conference (PVSC), 2010 35th IEEE , vol., no., pp.003223-003228, 20-25 June 2010

[18] T. SHIMIZU **Staebler-Wronski Effect in Hydrogenated Amorphous Silicon and Related Alloy Films**, Jpn. J. Appl. Phys. 43, (2004) 3257

[19] K.W. JANSEN, S.B. KADAM AND J.F. GROELINGER **The Advantages of Amorphous Silicon Photovoltaic Modules in Grid-Tied Systems**. Photovoltaic Energy Conversion, Conference Record of the 2006 IEEE 4th World Conference on , vol.2, no., pp.2363-2366, May 2006

[20] A. FANTONI, M. VIEIRA AND R. MARTINS **Simulation of hydrogenated amorphous and microcrystalline silicon optoelectronic devices**. Mathematics and Computers in Simulation, Volume 49, Issues 4-5, September 1999.

[21] C. LEE, H. EFSTATHIADIS, J.E. RAYNOLDS, P. HALDAR **Two-dimensional computer modeling of single junction a-Si:H solar cells**. Photovoltaic Specialists Conference (PVSC), 2009 34th IEEE , vol., no., pp.001118-001122, 7-12 June 2009

[22] L. ZHANG, U. DAS, J. APPEL, S. HEGEDUS AND R. BIRKMIRE **Properties of amorphous silicon passivation layers for all back contact c-Si heterojunction solar cells**. MRS Symp Proc., 2011

[23] D. DIOUF, J.P. KLEIDER, T. DESRUES, P.J. RIBEYRON. **2D simulations of interdigitated back contact heterojunction solar cells based on n-type crystalline silicon**. Phys. Status Solid, 2010

[24] SYNOPSYS. **Sentaurus Structure Editor User Guide**. version F-2011.09, September 2011

[25] SYNOPSYS. **Sentaurus Device User Guide**. version F-2011.09, September 2011

[26] SYNOPSYS. **Inspect User Guide**. version F-2011.09, September 2011

[27] D. BJELOPAVLIC, D. PANTIC, B. DORDEVIC AND D. PANTIC **Simulation of hetero-junction silicon solar cells**. Contemporary Materials I-2, 2010

[28] SYNOPSYS APPLICATIONS NOTE. **Simulation of 2D Single-Junction GaAs Solar Cell**. 2012

[29] SYNOPSYS APPLICATIONS NOTE. **Sentaurus Technology Template: EQE and I–V Curve Calculation of Textured Solar Cells Using Raytracer**. 2011

[30] SYNOPSYS APPLICATIONS NOTE. **Three-dimensional Optical Simulation of Textured Surface Silicon Solar Cell**. 2012

[31] A. FROITZHEIM, K. BRENDEL, L. ELSTNER, W. FUHS, K. KLIEFOTH, M. SCHMIDT **Interface recombination in heterojunctions of amorphous and crystalline silicon**. Journal of Non-Crystalline Solids, Volumes 299-302, Part 1, April 2002

[32] S. HERASIMENKA, K. GHOSH, S. BOWDEN AND C. HONSBERG **2D modeling of Silicon Heterojunction Interdigitated Back Contact solar cells**. Photovoltaic Specialists Conference (PVSC), 2010 35th IEEE , vol., no., pp.001390-001394, 20-25 June 2010

[33] M.R. PAGE, E. IWANICZKO, Y. XU, Q. WANG, Y. YAN, L. ROYBAL, H.M. BRANZ AND T.H. WANG **Well Passivated a-Si:H Back Contacts for Double-Heterojunction Silicon Solar Cells**. Photovoltaic Energy Conversion, Conference Record of the 2006 IEEE 4th World Conference on , vol.2, no., pp.1485-1488, May 2006